UNIVERSITY OF CALIFORNIA, SAN DIEGO

Surface and Interface Engineering of Organometallic and Two Dimensional Semiconductor

A dissertation submitted in partial satisfaction of the requirements for the degree Doctor of Philosophy

in

Materials Science and Engineering

by

Jun Hong Park

Committee in Charge:

Professor Andrew C. Kummel, Chair
Professor Peter M. Asbeck
Professor Shadi A. Dayeh
Professor William C. Trogler
Professor Paul K. Yu

2017

Dissertation of Jun Hong Park is approved, and it is acceptable in quality and form for publication on microfilm and electronically:

Chair

University of California, San Diego

2017

TABLE OF CONTENTS

LIST OF SYMBOLS AND ABBREVIATIONS

Å	angstrom
AFM	atomic force microscopy
ALD	atomic layer deposition
BE	binding energy
CB	conduction band
C_{max}	maximum capacitance
CV	capacitance voltage
CVD	chemical vapor deposition
DFT	density functional theory
DMA	dimethylaluminum
DOS	density of states
e	electron
E_F	Fermi level
EOT	equivalent oxide thickness
h	Planck's constant
I	electric current
KE	kinetic energy
L	Langmuir
LDOS	local density of states
MBE	molecular beam epitaxy
MMA	monomethylaluminum
MOSCAP	metal oxide semiconductor capacitor
MOSFET	metal oxide semiconductor field effect transistor
nA	nanoamps

nm	nanometer
pA	picoamps
PBE	Perdew-Burke-Emzerhof
PBN	pyrolitic boron nitride
PDA	post deposition anneal
SPM	scanning probe microscopy
SRC	Semiconductor Research Corporation
STM	scanning tunneling microscopy
TMA	trimethylaluminum
UHV	ultra high vacuum
V	volts
VASP	Vienna ab-initio simulation package
VB	valence band
V_{th}	threshold voltage
XPS	x-ray photoelectron spectroscopy
υ	frequency
Φ_{spec}	spectrometer work function

LIST OF FIGURES AND TABLE

ACKNOWLEDGEMENTS

I would like to acknowledge my advisor, Professor Andy C. Kummel for allowing me join his group and have the graduate school experience. Being able to collaborate with large number of different group in U.S and have access to quality equipment in the lab made most of the experimentation fun.

I would also like to acknowledge all members of the Kummel group. It was extremely motivating to work with intelligent someone and I attribute a lot of my abilities to their teaching skills. They were great teammates and I enjoyed, as much as one can with vacuum equipment, working with them on our various projects.

It is nearly impossible to write this dissertation, if it had not been for the help of our many collaborators. Professor William C. Trogler deserves an enormous thanks for giving us significant discussion in chemistry of organic molecules. Dr. Suresh Vishwanath and Professor Huili Grace deserve thanks for growing us high quality MBE TMDs. Sara Fathipour, Professor Susan K. Fullerton-Shirey and Professor Alan Seabaugh helped and co-worked us to gain an understanding of novel device fabrication and electrical characterization. Also Hema C.P. Movva, Atresh Sanne, Amritesh Rai and Professsor Sanjay K. Banerjee deserve great thanks for all helping and co-working us in fabrications of devices with graphene and TMDs. Finally I would also like to thank to Professor Pabitra Choudhury for all DFT calculations

My committee deserves huge thanks for giving up their precious time to attend my Senate and Thesis Defense presentations. The committee includes Professor Paul Yu, Professor William Trogler, Professor Peter Asbeck, and Professor Shadi A. Dayeh.

I would like to thank my family for their support throughout these six years and my whole life. And my friends for always providing an entertaining atmosphere in and out of the campus.

This work was funded by the Semiconductor Research Corporation (SRC) and National Science Foundation (NSF).

Chapter 2, in part or in full, is Reproduced with permission from “Jun Hong Park, James E. Royer, Evgeniy Chagarov, Tobin Kaufman-Osborn, Mary E. Edmonds, Tyler Kent, Sangyeob Lee, William C. Trogler, Andrew C. Kummel. Atomic Imaging of the Irreversible Sensing Mechanism of NO_2 on Copper Phthalocyanine. Journal of the American Chemical Society, 2013, 135 (39), pp 14600–14609.” Copyright [2017] American Chemical Society.

Chapter 3, in part or in full, is Reproduced with permission from “Jun Hong Park, Suresh Vishwanath, Xinyu Liu, Huawei Zhou, Sarah M. Eichfeld, Susan K. Fullerton-Shirey, Joshua A. Robinson, Randall M. Feenstra, Jacek K. Furdyna, Debdeep Jena, Huili Grace Xing, and Andrew C. Kummel. Scanning Tunneling Microscopy and Spectroscopy of Air Exposure Effects on Molecular Beam Epitaxy Grown WSe_2 Monolayers and Bilayers. ACS Nano 2016, 10, pp 4258−4267.” Copyright [2017] American Chemical Society.

Chapter 4, in part or in full, is Reproduced with permission from “Jun Hong Park, Hema C.P. Movva, Evgeniy Chagarov, Kasra Sardashti, Harry Chou, Iljo Kwak, Kai-Ting Hu, Susan K. Fullerton-Shirey, Pabitra Choudhury, Sanjay K. Banerjee, Andrew C. Kummel. In Situ Observation of Initial Stage in Dielectric Growth and Deposition of Ultrahigh Nucleation Density Dielectric on Two-Dimensional Surfaces. Nano Letters, 2015, 15 (10), pp 6626–6633.” Copyright [2017] American Chemical Society.

Chapter 4, in part or in full, is Reproduced with permission from “Jun Hong Park, Sara Fathipour, Iljo Kwak, Christopher F. Ahles, Suresh Vishwanath, Huili Grace Xing, Susan K. Fullerton- Shirey, Alan Seabaugh, Andrew C. Kummel. Atomic Layer Deposition of Al_2O_3 on WSe_2 Functionalized by Titanyl Phthalocyanine. ACS Nano, 2016, 10 (7), pp 6888–6896.” Copyright [2017] American Chemical Society.

The dissertation author was the primary investigator and author of these papers.

VITA

EDUCATION

2007 Bachelor of Materials Science and Engineering, Hanyang University, Seoul, Korea

2009 Master of Materials Science and Engineering, Hanyang University, Seoul, Korea

2017 Doctor of Philosophy in Materials Science and Engineering, University of California, San Diego

PUBLICATIONS

[1] Atomic Imaging of the Irreversible Sensing Mechanism of NO2 on Copper Phthalocyanine
Journal of the American Chemical Society, 2013, 135 (39), pp 14600–14609
Jun Hong Park, James E. Royer, Evgeniy Chagarov, Tobin Kaufman-Osborn, Mary E. Edmonds, Tyler Kent, Sangyeob Lee, William C. Trogler, Andrew C. Kummel

[2] NO Adsorption on Copper Phthalocyanine Functionalized Graphite
The Journal of Physical Chemistry C, 2014, 118 (19), pp 10076–10082
Jun Hong Park, Pabitra Choudhury, Andrew C. Kummel

[3] Domain Fracture and Recovery Process of Metal Phthalocyanine Layer via NO_2 and H_2O Dosing
Journal of Vacuum Science & Technology B Vol. 33, 030604 (2015)
Jun Hong Park, Sangyeob Lee, Andrew C. Kummel

[4] Passivation of InGaAs(001)-(2x4) by Self-limiting CVD of a Silicon Hydride Control Layer
Journal of the American Chemical Society 2015, 137 (26), pp 8526–8533
Mary Edmonds, Tyler Kent, Evgueni Chagarov, Ravi Droopad, Mei Chang, Jessica Kachian, ***Jun Hong Park***, Andrew Kummel

[5] Solution-Cast Monolayers of Cobalt Crown Ether Phthalocyanine on Highly Ordered Pyrolytic Graphite

The Journal of Physical Chemistry C, 2015, 119 (38), pp 21992–22000

Hao Lu, Iljo Kwak, ***Jun Hong Park,*** Katie O'Neill, Taniyuki Furuyama, Nagao Kobayashi, Alan Seabaugh, Andrew Kummel, Susan K. Fullerton-Shirey

[6] In Situ Observation of Initial Stage in Dielectric Growth and Deposition of Ultrahigh Nucleation Density Dielectric on Two-Dimensional Surfaces

Nano Letters, 2015, 15 (10), pp 6626–6633

Jun Hong Park, Hema C.P. Movva, Evgeniy Chagarov, Kasra Sardashti, Harry Chou, Iljo Kwak, Kai-Ting Hu, Susan K. Fullerton-Shirey, Pabitra Choudhury, Sanjay K. Banerjee, Andrew C. Kummel

[7] Scanning Tunneling Microscopy and Spectroscopy of Air Exposure Effects on Molecular Beam Epitaxy Grown WSe_2 Monolayers and Bilayers

ACS Nano 2016, 10, pp 4258−4267

Jun Hong Park‡, Suresh Vishwanath‡, Xinyu Liu, Huawei Zhou, Sarah M. Eichfeld, Susan K. Fullerton-Shirey, Joshua A. Robinson, Randall M. Feenstra, Jacek K. Furdyna, Debdeep Jena, Huili Grace Xing*, and Andrew C. Kummel*

[8] Atomic Layer Deposition of Al_2O_3 on WSe_2 Functionalized by Titanyl Phthalocyanine

ACS Nano, 2016, 10 (7), pp 6888–6896

Jun Hong Park†, Sara Fathipour†, Iljo Kwak, Christopher F. Ahles, Suresh Vishwanath, Huili Grace Xing, Susan K. Fullerton- Shirey, Alan Seabaugh*, Andrew C. Kummel*,

† Both authors have contributed equally to this publication.

[9] Low Temperature Thermal ALD of an SiN_x interfacial diffusion barrier and interface passivation layer on Si_xGe_{1-x}(001) and Si_xGe_{1-x} (110)

J. Chem. Phys. 146, 052820 (2017)

Mary Edmonds, Kasra Sardashti, Steven Wolf, Evgueni Chagarov, Max Clemons, Tyler Kent, ***Jun Hong Park,*** Kechao Tang, Paul C. McIntyre, Naomi Yoshida, Lin Dong, Russell Holmes, Daniel Alvarez, Andrew C. Kummel

[10] Low efficiency upconversion nanoparticles for high-resolution coalignment of near-infrared and visible light paths on a light microscope
Accepted in ACS Applied Materials & Interfaces
Sriramkumar Sundaramoorthy, Adrian Garcia Badaracco, Sophia M. Hirsch, ***Jun Hong Park***, Tim Davies, Julien Dumont, Mimi Shirasu-Hiza, Andrew C. Kummel, Julie C. Canman

[11] Self-limiting CVD of a passivating SiO_x control layer on InGaAs(001)-(2x4) with the prevention of III-V oxidation
Accepted in Surface Science
Mary Edmonds, Steven Wolf, Evgueni Chagarov, Tyler Kent, ***Jun Hong Park,*** Russell Holmes, Daniel Alvarez, Ravi Droopad, Andrew C. Kummel

[12] Growth Mode Transition from Monolayer by Monolayer to Bilayer by Bilayer in Molecularly Flat Titanyl Phthalocyanine Film
Manuscripts submitted in The Journal of Physical Chemistry C
Jun Hong Park, Lalitasri Ravavar, Iljo Kwak, Randall M. Feenstra, Pabitra Choudhury, Andrew C. Kummel

FIELD OF STUDY

Major Field: Materials Science and Engineering

Studies in Surface Science and Physical Chemistry

Professor Andrew C. Kummel

ABSTRACT OF THE DISSERTATION

Surface and Interface Engineering of Organometallic and Two Dimensional Semiconductor

by

Jun Hong Park

Doctor of Philosophy in Materials Science and Engineering

University of California, San Diego, 2017

Professor Andrew C. Kummel, Chair

For over half a century, inorganic Si and III-V materials have led the modern semiconductor industry, expanding to logic transistor and optoelectronic applications. However,

these inorganic materials have faced two different fundamental limitations, flexibility for wearable applications and scaling limitation as logic transistors. As a result, the organic and two dimensional have been studied intentionally as potential candidates for the novel electronic and optoelectronic applications. In the present dissertation, three different studies will be presented with followed order; (1) the chemical response of organic semiconductor in NO_2 exposure. (2) The surface and stability of WSe_2 in ambient air. (3) Deposition of dielectric on two dimensional materials using organometallic seeding layer.

In first part, the organic molecules rely on the van der Waals interaction during growth of thin films, contrast to covalent bond inorganic semiconductors. Therefore, the morphology and electronic property at surface of organic semiconductor in micro scale is more sensitive to change in gaseous conditions. In addition, metal phthalocyanine, which is one of organic semiconductor materials, change their electronic property as reaction with gaseous analytes, suggesting as potential chemical sensing platforms. In the present part, the growth behavior of metal phthalocyanine and surface response to gaseous condition will be elucidated using scanning tunneling microscopy (STM).

In second part, the surface of layered transition metal dichalcogenides and their chemical response to exposure ambient air will be investigated, using STM. Layered transition metal dichalcogenides (TMDs) have attracted widespread attention in the scientific community for electronic device applications because improved electrostatic gate control and suppression of short channel leakage resulted from their atomic thin body. To fabricate the transistor based on TMDs, TMDs should be exposed to ambient conditions, while the effect of air exposure has not been understood fully. In this part, the effect of ambient air on TMDs and partial oxidation of TMDs will be investigated.

In the last part, uniform deposition of dielectric layers on 2D materials will be presented, employing organic seedling layer. Although 2D materials have been expected as next generation

semiconductor platform, direct deposition of dielectric is still challenging and induces leakage current commonly, because inertness of their surface resulted from absent of dangling bond. Here, metal phthalocyanine monolayer (ML) is employed as seedling layers and the growth of atomic layer deposition (ALD) dielectric is investigated in each step using STM.

Chapter 1

Introduction

1.1 Metal phthalocyanines molecules

Metal phthalocyanines (MPc) have been studied for organic thin film transistor (OTFT) gas sensors[1-6] or organic photovoltaics cell (OPV)[7-15]. The metal atoms are placed at the center of molecule, while four outer benzene rings surround the metal center, as shown in Fig. 1.1. The MPc films can be deposited on inorganic or polymer substrates by various techniques, such as vapor deposition, spin coating, and spray coating. Although other organic, such as pentacene, thin films may have higher mobilities or photo-sensitivity, MPcs are possess high thermal stability thereby it can be integrated in the high temperature process. For example, MPcs can maintain their molecule structure at temperatures exceeding 400 °C[16], and only a few strong acids and oxidizing agents are able to decompose MPcs. The electronic properties of MPcs can be tuned by changing the central metal atom or adding functional groups to the outer rings. In addition, the charge distribution in the MPc molecule is not uniform; the central nitrogen and metal atom have a relatively higher electron density, while the inner carbon atoms have a lower electron density than the outer aromatic carbon atoms[1], thereby the reactivity of center in MPc with gaseous molecules can be higher than outer benzene rings. Structural and electronic properties of single MPc molecules and monolayers on solid surfaces (mostly single crystalline metal) have been investigated by multiple research groups, using the various surface analysis techniques.[17-23]

1.2 Two dimensional semiconductors

A two dimensional (2D) semiconductors are consistent with a type of semiconductors, with atomically thin thickness (typically 3 – 7 Å). Graphene is a famous example of 2D semiconductor, as shown in Fig 1.2.a; it is a single atomic layer of carbon with honeycomb atomic structure, and

considered originally as near metal, but it was rediscovered by Geim and Novoselov as semiconductors[24] with the superior mobility than other semiconductors. However, graphene has a zero-band gap, limiting in direct integration into logic devices. Therefore, stacking bilayer, chemical doping or formation of graphene nano-ribbon have been studied to open the band gap in graphene.

As shown in Fig. 1.2.b, layered transition metal dichalcogenides (TMDs), which is consistent with a metal layer sandwiched by two chalcogenides layers, also have been studied intensively, because they have readily band gap, unlike graphene. Moreover, as the thickness of TMDs decreases to monolayer, indirect-to-direct band gap crossover can be observed with stable emission of exciton at room temperature, therefore their applications can be expanded to both of logic and optoelectronic transistors[25-32].

Furthermore, since these layer materials do not have dangling bonds at the surfaces (both graphene and TMDs), these 2D topology enables heterojuction stacking without inducing lattice mismatch and strain between the layers. This feature makes possible the fabrication of transistors and diodes scaled to atomic thicknesses with tunable band gaps and excitonic effects.[33-35]

Various 2D materials growth methods, characterization of physical properties, and device applications have been intensively pursued by multiple research groups. Initial investigations on 2D materials focused on exfoliated bulk crystals that were naturally formed or grown by chemical vapor transport (CVT) or chemical vapor deposition (CVD).[36-40] Molecular beam epitaxy (MBE) has been employed more recently to grow TMDs, such as $MoSe_2$, $HfSe_2$ and SnS.[41-45]

1.3 Ultra High Vacuum Chamber

All of scanning tunneling microscopy (STM), spectroscopy (STS) and the x-ray photoelectron spectroscopy (XPS) were performed in an ultrahigh vacuum chamber (Omicron variable temperature chamber). The entire system consists of five sets of chambers, shown in Fig.

1.3, the STM chamber, the preparation chamber, the load lock chamber, the atomic layer deposition (ALD) chamber, and the organic MBE chamber. Each chamber is pumped by ion or turbo pumps and separated by gate valves. The main (sample preparation) and STM chambers are pumped by ion pumps; the base pressure of each is below 1 x 10^{-10} and 5 x 10^{-11} torr, respectively. The organic MBE, ALD, and load-lock chambers are pumped by turbo molecular pumps (TMP); the base pressures of the organic MBE, load lock, and ALD chambers are 5 x 10^{-9}, 1 x 10^{-7} and 3 x 10^{-6} torr, respectively.

1.4 Scanning Tunneling Microscopy and Spectroscopy

In this dissertation, scanning tunneling microscopy (STM) in UHV is employed, as a main tool, to investigate the various semiconductor surfaces in atomic scale. First STM was demonstrated by Binning and Rohrer in 1981[46]. The operation of STM is relies on the tunneling process of single or a few electrons between metal tips and samples; the tungsten (W) or Pt/Ir tips, are approached to sample surfaces of interest within few angstroms (Å) with a piezo electric crystal, while a bias (V) is applied to the tip relative to the sample simultaneously, resulting in the quantum mechanical tunneling current. By measurements this tunneling current passing through the STM tip, the location of atoms or morphology can be reconstructed and imaged, using a feedback loop to maintain a constant tunneling current. The tunneling current is exponentially proportional to distance (z), as shown below equation,

$$I \propto V \rho_s e^{-1.025\sqrt{\emptyset}z}$$

where ρ_s is local density of states (LDOS) of sample, ϕ is work function of sample. Following this equation, the tunneling current increases 7.4 times, as decreasing of Z by about 1 Å, allowing STM for atomic resolution.

As the sample is biased positively or negatively to the STM tip, the LDOS of the sample can be probed. As shown in Fig. 1.4, a W STM tip is approached on TiOPc/HOPG surface, while the TiOPc/HOPG is applied negative or positive bias. If the sample is biased negatively relative to the tip, the electrons tunnel from occupied orbitals, highest occupied molecular orbital (HOMO), to metal tip with locating Fermi level (E_F) of tip below of HOMO in the sample, consistent with probing the filled states of TiOPc. Conversely, If the sample is biased positively relative to the tip, the electrons tunnel from metal tip to unoccupied orbitals, lowest unoccupied molecular orbital (LUMO), with locating Fermi level of tip above of LUMO in the sample, consistent with probing the empty states of TiOPc. By choosing these two different imaging modes in STM, the LDOS of samples can be visualized.

During STM imaging, if a tip is located on a particular place of sample surface with a constant distance, the current (I) can be recorded by applying bias (V). When the number of electrons between tip and sample is very few to be in tunneling range, the tunneling probability is directly proportional to the number of available states in the sample. Therefore, since the tunneling current is measured as a function of electron energy in the sample, the differential of tunneling currents (dI/dV) is directly corresponded to the electron density of states, LDOS. Using this technique, the electronic states within few eV (normally 4 eV) can be observed near Fermi level (0V).

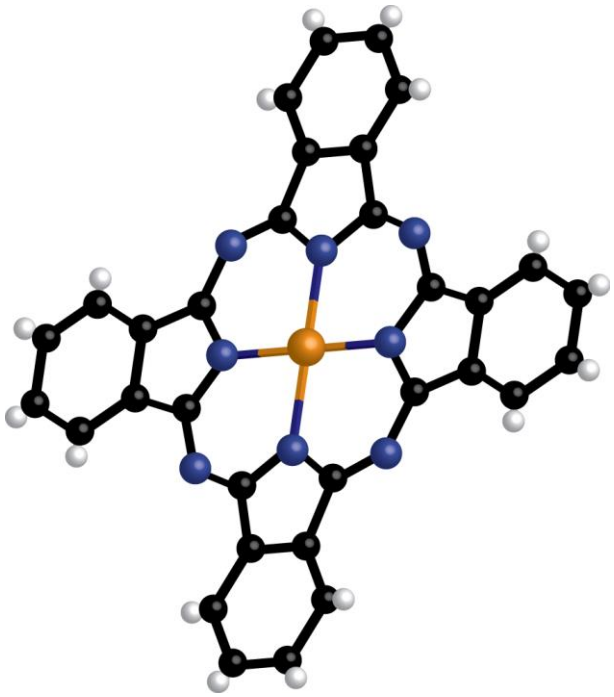

Figure 1.1. Schematic molecular structure of metal phthalocyanines; a central metal atom appears as the orange ball, while nitrogen atoms are shown as blue balls. Carbon and Hydrogen are displayed as black and white balls respectively.

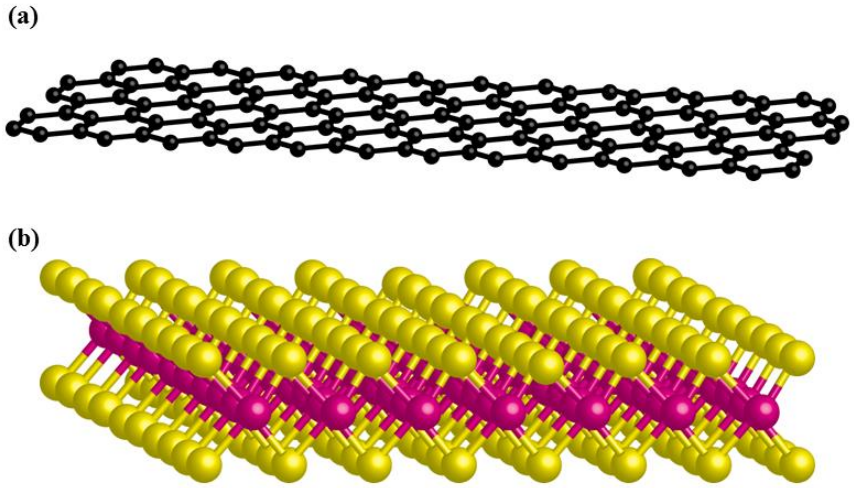

Figure 1.2. Schematics of graphene and TMDs. (a) graphene with a hexagonal carbon network. (b) TMDs consistent with a metal layer sandwiched by dichalcogenides.

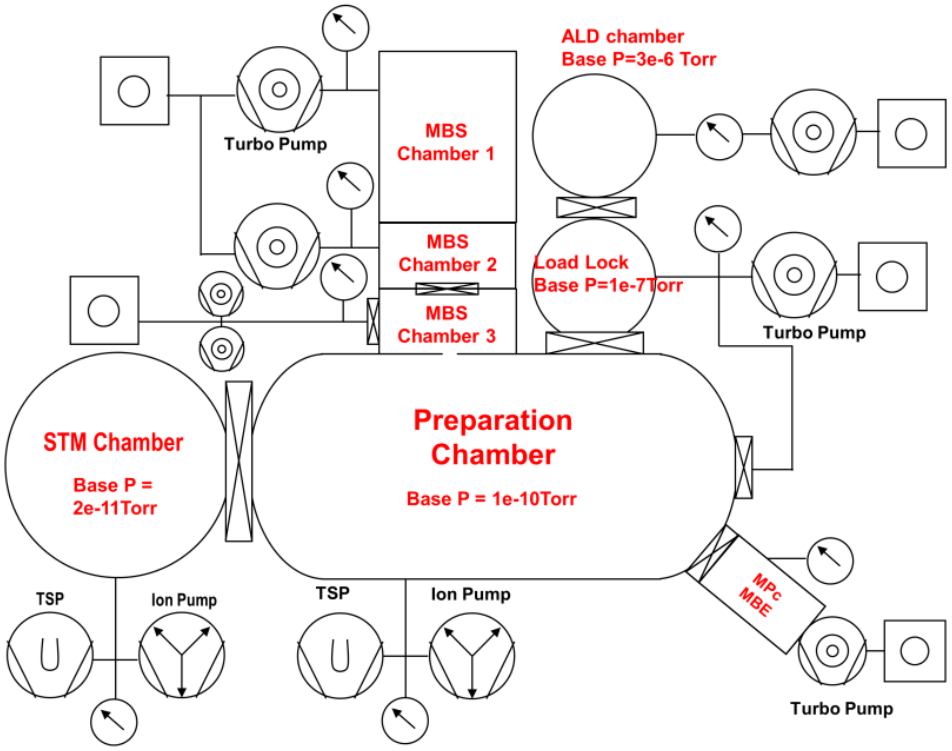

Figure 1.3. Schematic diagram of the Omicron variable temperature UHV system with custom built three chamber dosing, MBE and ALD system.

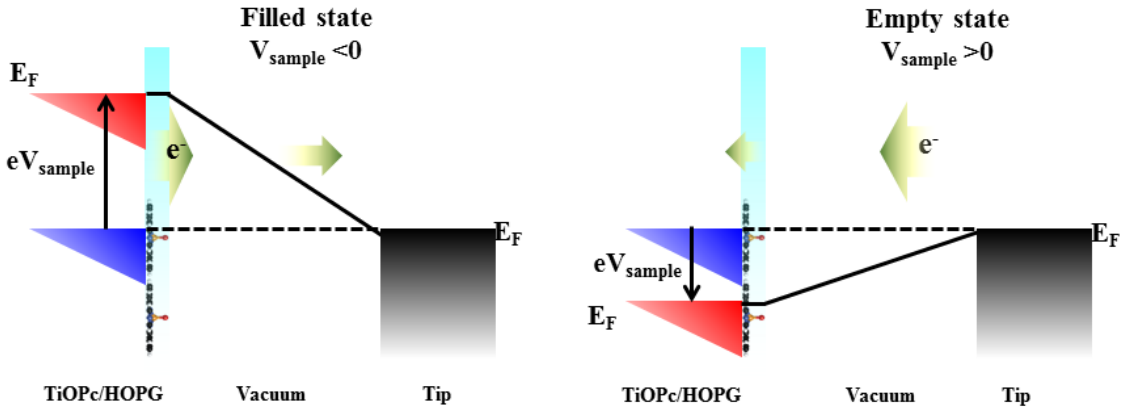

Figure 1.4. Schematic representation of filled and empty state STM imaging. Right: Filled state STM imaging. Left: Empty state imaging.

Chapter 2

Atomic Imaging of the Irreversible Sensing Mechanism of NO_2 Adsorption on Copper Phthalocyanine.

2.1 Abstract

Copper(II) phthalocyanine (CuPc) monolayers exposed to ambient NO_2 is observed using scanning tunneling microscopy (STM) in ultra-high vacuum (UHV) to elucidate the chemical response of CuPc at the molecular level. The bare CuPc ML is deposited on Au(111) surface using a molecular beam epitaxy. After exposure of low NO_2 dose at room temperatures, isolated chemisorption sites on the CuPc metal centers are observed in STM images. These chemisorbates almost completely disappears with annealing at 373 K for 30 min. Conversely, after exposure of high NO_2 doses, the exposure of NO_2 results in a fracture of the domains in CuPc ML. This domain fracture can be recovered by annealing above 423 K, indicating dissociative chemisorption into NO and atomic O accompanied by surface restructuring. This high stability indicates that the domain fracture is induced by tightly bound adsorbates. Existence of atomic O in the CuPc ML/Au (111) is confirmed by XPS analysis and ozone dosing control experiments. The observed CuPc domain fracturing with NO_2 dosing is consistent with a mechanism for the dosimetric sensing of NO_2 and other reactive gasses by organic thin film transistors (OTFTs).

2.2 Introduction

As referred in the section 1, MPc molecules have been considered as potential chemical sensing platforms, because MPc molecules act as electron donors because of their delocalized π-electrons, behave as p-type semiconductors, and provide a basis for chemiresistive sensing.[1, 47-48] The low ionization energy of MPcs imparts low activation energy for formation of charge transfer complexes with oxidizing gases. In addition, since the N and metal at the central area of MPc have higher electron density than the benzene rings, the charge transfer reactions of MPc with electron acceptor gasses are strongly favored to occur on the central metal atoms[1].

As a result, detection of electron-accepting analytes by MPcs OTFTs relies on reaction between the metal center and analytes, which in a simplified model act as "dopants":[49-50] Although pure MPcs films are insulating in vacuum, they become p-type semiconducting with exposure to dopant gases.[1, 49-51] This p-type conductivity of metal phthalocyanines films has been modeled as formation of charge transfer complexes on the metal centers with oxidative molecules. Weak oxidative analytes (such as O_2)[4, 50] chemisorb weakly on MPc films as electron acceptors and form superoxide adducts consisting of oxidized MPc^+ and O^{2-} species; holes are injected into the bulk solid from the positively charged MPc^+. The injection of these holes moves the HOMO edge towards the Fermi level forming a p-type MPc film[1]. The presence of this superoxide adducts on MPc has been studied using Electron paramagnetic resonance (EPR) and electron spin resonance (ESR) [52-54].

In chemical sensors based on MPc, higher chemical sensitivities are observed for strong binding analyte, such as NO_2, O_3, H_2O_2 and NO, than weak binding analytes.[3, 55-61] Weak binding analytes induce weak charge transfer reactions and have fast reversible recovery times. Similarly, tight binding dopants also show reversible recovery for low doses. However, for high doses, tight binding analytes, for example NO_2[2, 55, 62-64] or NO[60-61], have strong charge transfer reactions on MPc

films, resulting in very slow or irreversible recovery time. Since ambient air contains a high concentration of two such analytes, O_2 and H_2O, weak binding analytes are not ignored in practical sensing devices. Therefore, on MPc surfaces, the strong binder NO_2 must initially compete for reaction sites with gaseous or bound O_2 and H_2O, because O_2 and H_2O are present at much higher concentrations. When MPc is exposed to NO_2, it binds tightly to MPc molecules[1-2, 65]. However, after NO_2 dosing is ceased, the high background of O_2 and H_2O cause the NO_2 to desorb if it is reversibly bound. This competition model is consistent with strong binding analytes having reversible binding to MPc for very low analyte doses. However, for high analyte doses, the irreversible behavior observed for strong binding gaseous oxidants on MPc surfaces, and their ability to induce charge accumulation in the MPc film, is not fully understood on the molecular scale.[66]

Here, using scanning tunneling microscopy (STM), the irreversible sensing response of CuPc OTFTs exposed to NO_2 gas pulses is investigated at the molecular scale. Previously, it was shown that H_2O_2 vapor doses of high concentration induce an irreversible sensor response, involving an unrecoverable threshold voltage shift[59]. Since NO_2 is another strong binding gaseous oxidant, it is also expected to show an irreversible sensing threshold voltage shift on the CuPc surface. To investigate the sensing response to NO_2, CuPc OTFT sensing measurements are performed during exposures to a mixture of NO_2 and synthetic air. Afterwards, STM has been employed to image physical changes in the MPc surface that are induced by NO_2 binding.

2.3 Experimental Details

Bottom-gate, bottom-contact CuPc OTFTs were fabricated by photolithography. The source and drain electrodes were deposited by electron beam evaporation onto $SiO_2/n^{++}Si(100)$ substrates (Silicon Quest). The 100 nm thermally grown SiO_2 layer acts as a gate oxide with

C_{ox} = 34.5 nFcm^{-2}. The channel width (W = 10^5 μm) and length (L = 5 μm) are constant for all OTFTs. Deposition of 5 nm Ti was used as an adhesion layer for the 45 nm Au electrodes and electrical contact pads. A 4 monolayer CuPc film was deposited on the OTFT substrate under ultra-high vacuum using molecular beam deposition. The deposition rate was approximately 1 Å-s^{-1}. The devices were wire-bonded onto a ceramic dual in line package (DIP) and mounted on a printed circuit board for NO_2 sensing. Current-voltage (*I-V*) measurements were recorded *in-situ* during NO_2 vapor dosing. The *I-V* data for the OTFTs were analyzed every 60 s by a gate voltage (V_g) sweep from +10 V to –10 V at 4 Vs^{-1} with the drain voltage (V_{ds}) held at −10 V. A National Instruments PXI-6259 M-Series Multifunction DAQ controlled by a custom designed LabVIEW program was used for voltage sweeps and data acquisition. The threshold voltage (V_{th}) and mobility (μ) were calculated from a linear fit to the equation for OTFT drain current in the saturation regime (Equation 1).

$$\sqrt{I_d\left(sat\right)} = \sqrt{\frac{W\mu C_{ox}}{2L}}\left(V_g - V_{th}\right) \quad (1)$$

The V_{th} and μ calculation was performed in real time during sensing and used a constant range of fit for the gate voltage (V_g) of $-10\ V \leq V_g \leq -7\ V$. All OTFT sensing experiments were performed with zero grade air (Praxair, < 2 ppm H_2O, < 0.02 ppm NO_2) and a 10 ppm NO_2 mixture in dry air (Airgas).

For STM experiments, copper phthalocyanine (CuPc) was deposited on Au (111) in a Omicron ultra-high vacuum (UHV) system with a base pressure below 1 X 10^{-10} torr. The surface of single crystalline Au(111) at 25 °C was cleaned by sputtering with a 1 keV Ar^+ ion beam ion beam (RBD instruments) with an Ar background pressure of 6 X 10^{-5} torr. After sputtering, the Au(111) sample was annealed at 500 °C for 30 min for curing. Sputtering and annealing were repeated until STM imaging verified an atomically flat Au(111) surface.

The CuPc was purchased from Sigma Aldrich and purified by multiple sublimations. The sample was prepared by deposition of a thick overlayers on a cleaned Au (111) surface at 373 K by organic molecular beam epitaxy with use of a differentially pumped effusion cell (Eberl MBE-Komponenten), while the sample was in the UHV preparation chamber. Subsequently, this multilayer was heated to 623 K for 4 min, afterwards a flat-lying monolayer of CuPc was formed on the Au(111) surface, because the CuPc/CuPc interaction in multilayers is weaker than the CuPc/Au surface interaction.[67] The monolayer structure was confirmed by STM, which showed the characteristic Au(111) herringbone reconstruction through the single monolayer CuPc films. The monolayer samples were transferred from the preparation chamber via the load lock and introduced into the atmosphere for NO_2 dosing.

High concentration NO_2 dosing was performed with a 10 ppm NO_2 in dry synthetic air mixture onto CuPc monolayers at atmospheric pressure. These high concentration dosing studies were performed in an air-tight container with a constant flow of the 10ppm NO_2 mixture. Low concentration dosing (1 ppm NO_2 in dry synthetic air) was performed in a custom air-tight designed flow system with constant flow using mass-flow controllers. The 10ppm NO_2/air mixture was diluted 10-fold in synthetic air (Praxair, < 2 ppm H_2O,< 0.02 ppm NO_2) using a separate dilution line to create a 1 ppm NO_2 mixture in synthetic air.

Density functional theory (DFT) calculations were performed with the Vienna Ab-Initio Simulation Package (VASP)[68-69] using projector augmented-wave (PAW) pseudopotentials (PP)[70-71] and the PBE (Perdew-Burke-Ernzerhof) exchange-correlation functional[72-73]. The choice of PBE functional and PAW PP was validated by parameterization runs demonstrating good agreement with experimental properties of bulk Au and C, as well as N_2 and O_2 molecular properties. The atomic charges for calculated systems were obtained applying Bader charge decomposition[74-76].

2.4 Results

2.4.1 Chemical sensing response of CuPc OTFT to NO_2

The chemical sensing is presented prior to the STM experiments to show the electric evidence of irreversible NO_2 chemisorption *via* dosimetric sensing. In Fig. 2.1 shows typical sensing responses of CuPc OTFT to 100 ppb NO_2 gas pulses of variable duration (30 sec, 2 min, 5 min and 10 min) at 300 K. During these experiments, high purity dry air was employed as the purge and the carrier gas. Full current (I) – voltage (V) curves are measured at each point in time so that the influence of the NO_2 exposure on the mobility and threshold voltage(V_{th}) can be recorded independently. It is noted that the exposure of NO_2 in these sensor measurements are smaller than in the STM studies, because the I-V characteristics are closer to ideal for small doses thereby enabling independent measurement of the mobility and threshold voltage. Furthermore, fixed charge of less than 0.1% of a monolayer ($10^{12}/cm^2$) is readily detected by I-V measurement, which is much below the detection limitation of STM for almost any adsorbate. With increase if dosing time, the CuPc OTFT has a non-linear sensing response. Analyte induced changes in the mobility indicates the changes in the carrier trap energy or carrier density, while the changes in the threshold voltage is induced by changes in fixed charge in CuPc OTFT.

For short analyte pulses (30 sec and 2 min), mobility decreases and small V_{th} shifts are observed, but these changes are reversed by ceasing NO_2 dosing with the dry air flow. However, for longer doses (5 min and 10 min), large V_{th} shifts occur, and these shifts are irreversible and dosimetric as shown by red arrows. This is consistent with an analyte induced fixed charge in CuPc OTFT.

The DFT VASP plane-wave calculations show that the binding energies of NO and NO_2 to CuPc are low with 0.06 eV of NO_2/CuPc and 0.02 eV of NO/CuPc: 0.02 eV; for NO/CoPc, the DFT VASP plane-wave calculation estimates a binding energy of 1.57 eV, which agrees well with the

binding energy of 1.55 eV calculated by T. Nguyen *et al*[77] for the same NO/CoPc. As a result, the low adsorption energies of NO and NO_2 on CuPc are consistent with existence of another chemisorbate for irreversible changes in the fixed charge in the film. Thus, non-dissociative NO_2 adsorption, which has a weak interaction with the Cu metal center, can be ruled out to explain the irreversible V_{th} shifts, while a secondary effect from NO_2 dosing would be responsible for the irreversible component of sensing.

2.4.2 Morphology changes in CuPc monolayers induced by dosing NO_2

A CuPc monolayer dosed with NO_2 was imaged in UHV-STM in elucidate the moelculr change induced as a result of NO_2 dosing. As shown in Fig. 2.2.a, bare CuPc molecules form a crystalline on Au (111) with four-fold symmetry. The molecular structure of CuPc shown in Fig. 2.2.b, are well defined in individual CuPc molecules in the inset of Fig. 2.2.a. The holes are assigned to the Cu atom at the center of each CuPc molecule, while aromatic rings are displayed as an outer 4-leaf pattern[18].

After dosing NO_2 (1 ppm for 5min: low dose) and annealing at 50 ˚C to improve STM imaging, small NO_2 induced chemisorption sites are observed dispersing on the CuPc layer in Fig 2.3.(a). All DFT calculations estimate the binding configurations of single gaseous molecules to the metal centers of CuPcs, which is consistent with the low NO_2 dose STM images.[77-79] After annealing at 100 ˚C for 30 min, these chemisorbates desorb from the CuPc monolayer as shown in Fig 2.3.b. It is noted that although resolution difference is observed in between Fig 2.3.a and Fig 2.3.b, the both CuPc monolayers maintain four fold symmetry as well as observation of the Au(111) herringbone reconstruction (white arrow). In Fig 2.3.c, two different chemisorption sites are observed with a distinct bias dependence, as shown in Fig. 2.3.d and Fig. 2.3.e. It is noted that precipitates are observed on the domain boundaries of the CuPc monolayer, which were shown to

be mixtures of carbon complex and displaced CuPc molecules. The observed chemisorbates have variable bias dependence; for site A, the metal center is brighter than the aromatic ring in both the empty and filled state images. Conversely, for site B, the brightness of entire CuPc molecule is depressed in the filled state image, while they are brighter than neighboring molecules in the empty state. It can be hypothesized that after exposure of high NO_2, chemisorbate of NO_2/CuPc would influence the electronic structure of the CuPc molecules, thereby the diversity of observed isolated chemisorption sites is created.

Before exposure NO_2 on CuPc monolayer, the air exposure was performed on CuPc monolayer as a control. The bare CuPc molecules form nearly single crystalline domains on each Au (111) step as shown in Fig 2.4.a. When the CuPc monolayer is exposed to air for 30 min, any topographical changes are not observed in CuPc monolayer, such as reorganization of molecules or fractured domains, while some carbon-rich adsorbates from ambient air are observed, as shown Fig. 2.4.b.

After confirmation of inertness of CuPc monolayer in ambient air, higher concentrations of NO_2 were dosed on the CuPc monolayer surface to determine the mechanism of the irreversible sensing response. After dosing 10 ppm of NO_2 for 5 min on the CuPc monolayer, reconstruction of CuPc layer and fractured domains can be observed. As shown in Fig 2.5.a and 2.5.b, after 10 ppm of NO_2 is dosed at room temperature for 5 min (high dose) and annealed in UHV at 50 °C, new domain boundaries are induced with the decrease of domain sizes. The domains of air exposed CuPc monolayer are larger than 200 nm in length and limited by terrace size, while NO_2 exposed CuPc domains are 50-80 nm in length, as shown in Table 2.1. These NO_2 induced domain reconstruction is not recoverable at room temperature, as shown in Fig. 2.5.c. After additional annealing of sample from Fig. 2.5.b at 50 °C for over 1 hr, the reconstruction of domain in CuPc ML is unchanged, consistent with involving a tightly bound adsorbate. This domain fracture can be reversed by annealing above 150 °C , as shown in Fig. 2.5.d; after annealing of sample from Fig

2.5.c at 150 °C, larger area of domain are observed resulting from merging fractured domain. Consequently, this domain fracture in the CuPc monolayers can be reversible with annealing at high temperature, consistent with the V_{th} shifts observed in the OTFT sensor data at high dosing.

2.4.3 Domain fracture induced atomic O on bilayers and multilayers of CuPc

A similar domain fracture is also observed on bilayer and multilayer of CuPc, after exposure to equivalent NO_2 doses. On bare bilayer surfaces, CuPc molecules form a crystalline bilayer with an average domain size of 357±17 nm, as shown in Fig. 2.6. a and Table 2.1. After dosing NO_2, new domain boundaries are induced in both the first and second layer, as displayed in Fig. 2.6.b. However, the domains in second layer are more disordered than the domain in monolayer after equivalent NO_2 doses. On CuPc monolayers dosed by NO_2, although NO_2 dosing induces domain fracture, CuPc molecules still maintain close packed crystallinity, as shown in Fig. 2.6.c. Conversely, on bilayer dosed by NO_2, larger amounts of vacancies are observed and fractured domains in the first layer are clearly shown through vacancies in the second layer. The enlarged STM image of 2.6.b displays that the direction of CuPc molecules arranged in first layer exactly corresponds with the symmetry of the second layer, as shown by green and blue arrows. This matched orientation between first and second layer is consistent with the domains having vertical order since the domain fracture is induced at the CuPc/Au(111) interface. It is hypothesized that dissociative chemisorption of NO_2 product additional atoms, which result from the interaction of NO_2 on the CuPc/Au surface, penetrate the CuPc bilayer and chemisorb on the Au(111). These by-product atoms at the CuPc/Au(111) interface reconstruct the first CuPc layer, which also results in reconstruction of the second CuPc layer while maintaining the relative positions of CuPc in layers 1 and 2.

Subsurface reactions also induce reorientation of domain structure on multilayers. Before dosing NO_2, a smooth and large domain on clean multilayer surfaces are observed, as shown in Fig. 2.7.a, with the herringbone patterns of Au (111). However, after dosing NO_2 at 10 ppm for 5 min, small domains appear, as shown in Fig. 2.7.b. The NO_2 dosed multilayer CuPc domains possess a high defect density, forming polycrystalline domain structures similar to the ones observed on the NO_2 dosed CuPc bilayer surface. The average domain size (length) in the NO_2 dosed CuPc multilayer is about 51 ± 4 nm as shown in Table 2.1.

2.4.4. Chemical mechanism for irreversible behavior.

A tightly bound adsorbate induces the formation of fractured domains after high NO_2 dosing, changing the unit cell size of the MPc monolayer.[80] It can be hypothesized that this resutls from dissociative chemisorption of NO_2 into NO and atomic O. To confirm weakly bound adsorbates, flash desorption mass spectrometry was performed. Figure 2.8.a shows mass spectra of molecules which desorb from a CuPc surface dosed with 10 ppm of NO_2 for 5 min, as heating rapidly. The times in the Fig. 2.8.a indicates the duration of heating prior to recording the spectra at the temperatures. The 18, 28, and 44 m/z peaks correspond with background H_2O^+, CO^+ and CO_2^+, whose parent molecules are always present in the UHV chamber. A 30 m/z peak starts to be detected above 70 °C, and corresponded intensity increases as the surface temperature increases. In previously published mass spectra, NO_2 and NO both exhibit 30 m/z peaks, but only NO_2 has a 46 m/z mass component[81-82]. However, in Fig. 2.8.b, there is no detectable peak at 46 m/z. Other research groups also report that NO was detected on NO_2 dosed MPc by IR spectroscopy.[83] The observation of NO by flash desorption mass spectrometry is consistent with NO_2 dissociating to NO and atomic O on the CuPc monolayer, similar to multiple reports of NO_2 dissociation on various surfaces.[84-86]

A high concentration of O species on CuPc/Au dosed by NO_2 is observed by XPS analysis. To obtain the total concentration of O and N species, the XPS peaks for O and N were integrated and normalized to the Cu signal. Figure 2.8.c shows a huge increase of the relative ratio of O to Cu on the CuPc monolayer/Au, after dosing with 10 ppm of NO_2 for 5 min compared with an air exposed CuPc monolayer. On CuPc/Au surfaces dosed with 10 ppm of NO_2 for 5 min and annealed, the relative coverage of O is still four times larger than on an air exposed CuPc/Au monolayer, and the coverage of O decreases with annealing.

Conversely, the integrated nitrogen XPS peak is nearly independent of NO_2 dose. To elucidate the chemical binding status of N species, chemical fitting analysis was carried out in present XPS results. The N 1s spectra of the CuPc monolayer measured before and after dosing with 10 ppm of NO_2 for 5 min are displayed in Fig. 2.9.a and 2.9.b respectively. In Fig. 2.9.a, three components are detected on air exposed CuPc/Au; 398.1 eV is corresponded to the N-Cu bond and 398.6 eV is corresponded to the N-C bond[87]. It is noted the broad peak (400.0 eV) is induced by shake up transitions. There is difference in binding energy between present data and reference data, because the present binding energies are obtained from a monolayer of CuPc on Au, while reference data are obtained from thick CuPc layers on Si_3N_4 substrates. After dosing with NO_2, a new component is observed at 398.9 eV, consistent with the presence of NO_2. It is noted this NO_2 may be bound to precipitates or displaced CuPc molecules instead of the CuPc monolayer.

By XPS chemical fitting analysis, the presence of O atoms was elucidated, as shown in Fig 2.9.c and 2.9.d. These XPS spectra displays the O 1s spectra for the CuPc monolayer measured before and after dosing with 10 ppm of NO_2 for 5 min. CuPc/Au exposed only to air for 10 min shows a weak, broad peak from 531.5 to 533.5 eV, resulting from different oxygen states, for example O_2, and H_2O. However, after the NO_2 dosing, the main peak is at 532 eV, with new shoulder feature (green arrow). The presence of this shoulder indicates that the dosing with NO_2 induces formation of new O binding states in CuPc/Au (111). Using peak fitting procedures, three

components can be identified (532.0, 531.2 and 530.3 eV) in the O 1s spectra. The largest component at 532.0 eV can be assigned to the oxygen atoms which form as NO_2 on CuPc/Au,[88] and this is also shown in N1s spectra. Although NO_2 dosing results in low binding energy states of O in CuPc/Au associated with dissociation products, the majority of O still remains with a binding energy consistent with adsorbed molecular NO_2. The second peak at 531.2 eV is consistent with the presence of the O_2, which can be introduced from air during NO_2 dosing or produced during dissociative chemisorption of NO_2.[89] Lastly, the third peak is detected at 530.3 eV; this peak dominates the shoulder of O1s spectra. This binding energy is consistent with atomic O on Au;[90] there is a small difference in the binding energy between 530.3 eV and published data (530 and 530.1 eV) consistent with the atomic oxygen having interactions with both the Au surface and overlying CuPc molecules. As a result of XPS analysis, it is hypothesized that some of NO_2 dosed on CuPc/Au dissociates to atomic oxygen. It is noted that the difference in calculated binding energy between O/Au and CuPc/O/Au is only 0.15 eV. Furthermore, the difference in Bader charge is only 0.09 between O/Au and CuPc/O/Au(O/Au: 6.69 |e|, CuPc/O/Au 6.78 |e|). This small difference in Bader charge may be too small to induce a difference in binding energy in XPS spectra.

Domain fracture induced by atomic O was also confirmed by O_3 dosing control experiments, since O_3 dissociatively chemisorbs into O_2 and atomic O.[91] STM images were recorded after O_3 dosing on a CuPc monolayer for 10 min at 25 °C with a supersonic molecular beam source (MBS) as shown in 2.10.a. As a control, NO diluted in He was dosed on a CuPc monolayer by supersonic MBS for 10 min at 25 °C (Fig. 2.10.b), since it does not dissociatively chemisorb. In contrast to the results from ambient dosing with NO_2, dosing O_3 and NO with MBS results in a very low density of carbon-rich adsorbates so more detail of molecular structure can be observed. As shown in Fig. 2.10.a, dosing of O_3 on a CuPc monolayer generates new domains which are only 15-20 nm, which is consistent with subsurface O sites similar to the ones generated

by NO_2 dissociative chemisorption. Moreover, O_3 on CuPc induces the formation of crack sites as indicated by the red arrows, implying a new subsurface chemisorption site. Conversely, the CuPc monolayer dosed with NO does not show either domain fracture or crack sites.

DFT calculations were performed to determine the energetics of O transfer from CuPc to Au(111), as shown in Fig. 2.11.a to c. The reference state was gaseous atomic O. Note the plane wave VASP technique was employed to determine the bonding of NO_2 to CuPc; it was found that NO_2 bonding through O is more slightly favorable than through N by 0.02 eV, but the binding is so weak that accurate calculations on the transition state would require use of a hybrid function which is challenging for modeling large systems. However, it is known that NO is able to dissociate on Cu(111) and (100),[92-93] and NO_2 can dissociate on both Cu surfaces and CuPc layers,[1, 87, 94-95] consistent with NO_2 bond activation having only a modest activation energy barrier. When O atoms bond with the Au surface, there is a high binding energy (4.60 eV); This binding energy was calculated by subtracting atomic O and relaxed Au slab total energies from the energy of the relaxed O/Au system. When O bonds to the CuPc on Au(111), the binding energy is modest (1.66 eV). When the O atom is bonded between the CuPc and Au(111), the binding energy is calculated to be highest (4.76 eV) which is slightly greater than the binding energy of O on clean Au(111). It is noted that the reference states employed in Fig. 8 use atomic O in the gas phase O(g), Au(111)(s), and CuPc/Au(111)(s) to calculate the binding energies. The binding energy of O in O/CuPc/Au and CuPc/O/Au systems was calculated by subtracting total energies of atomic O and relaxed CuPc/Au system from the total energy of the relaxed O/CuPc/Au or CuPc/O/Au systems respectively. The total energies are ⁻819.754 eV, (adsorbed O, i.e O/CuPc/Au) and ⁻822.855 eV. (subsurface O, CuPc/O/Au); therefore, the 3.1 eV difference represents the increased binding of oxygen migrating from the surface site on CuPc to the site between CuPc and Au. Therefore, any O atoms would be expected to migrate readily to sub-CuPc layer sites bound to Au or just to the Au(111) surface sites.

An analysis of the Bader charges in the DFT calculations is consistent with the higher binding energy of the O electrons in dissociation products observed in XPS. The O/CuPc/Au(111) Bader charge is 6.53 |e| and on transfer to the gold surface the O atoms gains about a quarter of an electron; the O/Au(111) Bader charge is 6.69 |e| and the CuPc/O/Au charge is 6.78 |e|. This gain in electrons would induce a lower electron binding energy. The DFT calculations are consistent with a large thermodynamic driving force for O atoms dissociating from NO_2 on CuPc/Au(111) to diffuse to the Au(111) surface. These subsurface O binding sites should have very high thermal stability after their formation.

The high binding energy of O/Au(111) is consistent with the thermal stability of the fractured islands and O chemisorbates[91]. This desorption temperature of 200 °C is similar to the annealing temperature where recovery of domain fracture occurs. The CuPc/O/Au sites are not directly observed by STM, because it is likely that subsurface O atoms do not significantly change in the CuPc topography. This hypothesis is supported by DFT models of CuPc/O/Au which show that the height of both the metal center and the rings changes by less than 0.2 Å when the O atom is bound subsurface. However, even if O were chemisorbed between the CuPc molecules, this would be nearly impossible to detect since adsorbates on Au(111) cause only small corrugation in STM images while the CuPc has a height of 1.7 Å on Au(111).[18]

2.5 Discussion

A simplified model is proposed (Fig. 2.11.d) based on the sensing data, the STM data, and the DFT calculations. First, NO_2 molecules reversibly and molecularly chemisorb to the CuPc metal center and dissociate by an activated process into O and NO. It is noted that a surface bimolecular reaction is also possible ($2\ NO_2 \rightarrow NO + NO_3 \rightarrow NO + NO_2 + O$) since the experiments were performed at high concentration and not just high dose[96]; however, the final result of both the

unimolecular and bimolecular reactions is chemisorption of O atoms. Subsequently, the atomic O diffuses to the Au (111) surface, which allows binding of more NO_2. The substrate bound O atoms act as coadsorbates inducing a change in CuPc domain structure, such as domain fracture and rearrangement of molecules. The molecular rearrangement and domain fracture likely occur because of the increased distance between adjacent CuPc molecules after O coadsorption. The eventual high density of O atoms per CuPc molecule could lower the barrier for lifting the CuPc from the Au surface, and induce domain fracture or rearrangement.

The DFT calculations and XPS data are consistent with dissociating NO_2 to generate O atoms which adsorb on bare Au or insert into subsurface sites between CuPc molecules and Au(111). Also, the adsorption of atomic O between CuPc and the surface would induce a change in the CuPc spacing, which is typical of coadsorbates.[97-98] Due to this adsorption, the spacing between CuPc molecules increases or the MPc molecules rotate. These spacing changes between molecules induced by subsurface O adsorbates generate reorganization of CuPc molecules and the lattice mismatch shown in Fig. 2.12. The lines are drawn along the rows of CuPc (green arrow). On clean surfaces, the molecules form perfect linear arrays (Fig 2.11.a). However, on the NO_2 dosed CuPc monolayer, the molecules are aligned along only one direction (green arrow), while the CuPc shift ½ unit cell almost every 2 molecules along the perpendicular direction (red line) in Fig. 2.11.b.

The NO_2 induced domain fracturing of CuPc layers (mono, bi, and multilayer) is consistent with the irreversible sensing response with CuPc chemFETs.[62-63] Charge carriers have their highest mobility inside the domains since they are near perfect single crystals, while the domain boundaries act as barriers to charge transport.[99-106] The NO_2 dosing increases the density of domain boundaries by domain fracture to further isolate domains. Charge carriers require high energy to cross domain boundaries.[100, 102] Since NO_2 induced domain fracture originates at the CuPc/Au interface, it is proposed the NO_2 induced domain fraction also degrades the CuPc/Au electrical contacts. It is well known that the performance of OTFTs depends strongly on the interface between the organic layer

and metal contacts.[107-110] In CuPc OTFTs exposed to high NO_2 doses, the increased density of domain boundaries would act to trap carriers near the contacts and induce positive uncompensated charge, which is consistent with the increased threshold voltage observed on NO_2 dosing.

2.6 Summary

STM was employed to study ambient adsorption of NO_2 on CuPc monolayers and elucidate a molecular scale mechanism of NO_2 sensing for CuPc OTFT sensors. For low NO_2 exposures, isolated chemisorbates are observed on the CuPc metal centers. These chemisorbates are removed by annealing at 100 °C. However, after exposures of high NO_2, domain fractures is observed in the CuPc film, because the NO_2 induced reorganization and domain fractures in CuPc. The generated domain fractures are stable at 25 ˚C and can only be reversed by annealing above 150 ˚C. Such high stability indicates that the driving force for domain fracture originates from strongly bound adsorbates. The existence of atomic O on Au(111) after exposure to NO_2 is confirmed by XPS analysis. Therefore, the STM and XPS data are consistent with a dissociation of NO_2 and generation of an O/CuPc complex. As shown by DFT calculations, O binds stronger with subsurface sites on the Au(111) surface than with top of CuPc molecules. It is proposed that the migrated O atoms bound in between CuPc and Au induce domain fracture. The dissociation of NO_2 generates atomic O which adsorbs at the CuPc/Au interface. This mechanism is supported by studies of O_3 dissociative chemisorption on CuPc monolayers, as well as NO_2 dosing of bilayer and multilayer CuPc/Au(111), both of which show similar NO_2 induced domain fracture. These NO_2 induced reconstructions of domains on bilayers and multilayers are consistent with domain fracture being one of important source for the irreversible V_{th} shifts observed in CuPc OTFTs. The types of mechanisms that lead to dosimetric sensing in the present instance (i.e., secondary surface reactions of analytes and sensor surface reconstruction) may serve as a model for the dosimetric sensing behavior in other OTFT chemical sensors, especially those which use metal phthalocyanines.

2.7 Acknowledgements

This work was supported by NSF Grant CHE-0848502 and STARnet, a Semiconductor Research Corporation program, sponsored by MARCO and DARPA.

Chapter 2, in part or in full, is Reproduced with permission from “Jun Hong Park, James E. Royer, Evgeniy Chagarov, Tobin Kaufman-Osborn, Mary E. Edmonds, Tyler Kent, Sangyeob Lee, William C. Trogler, Andrew C. Kummel. Atomic Imaging of the Irreversible Sensing Mechanism of NO2 on Copper Phthalocyanine. Journal of the American Chemical Society, 2013, 135 (39), pp 14600–14609.” Copyright [2017] American Chemical Society. The dissertation author was the primary investigator and author of this paper.

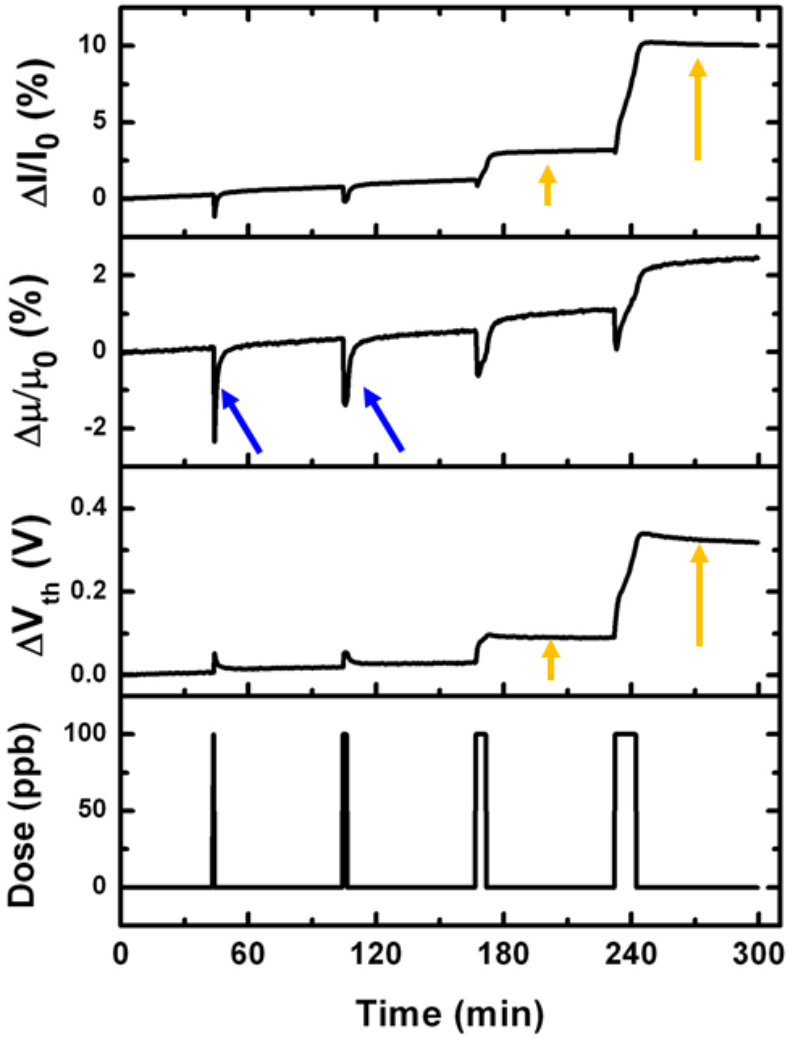

Figure 2.1. Chemical sensing response of CuPc OTFTs to 100 ppb of NO_2 gas pulses as a function of duration. The pulses were 30 s, 2 min, 5min, and 10 min, resulting in integrated doses of 0.05 − 1 ppm min^{-1}. I−V characterization was performed at every data point to extract the mobility and the threshold voltage.

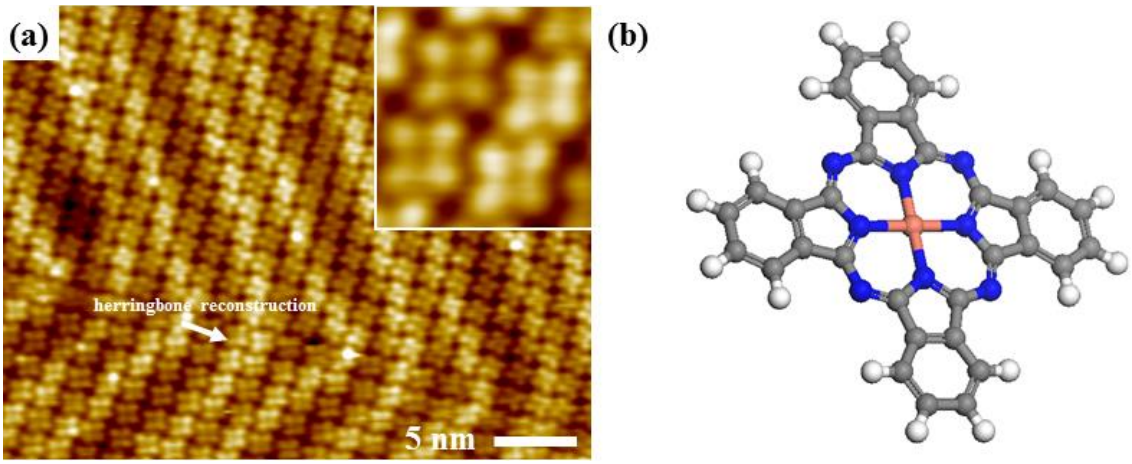

Figure 2.2. (a) Empty state STM image of a bare CuPc monolayer. (Vs = 2.0 V, It = 40 pA) Inset image shows individual CuPc molecules at the molecular level. (b) Molecular structure of CuPc (pink ball = Cu, blue ball = N, gray ball = C, white ball = H).

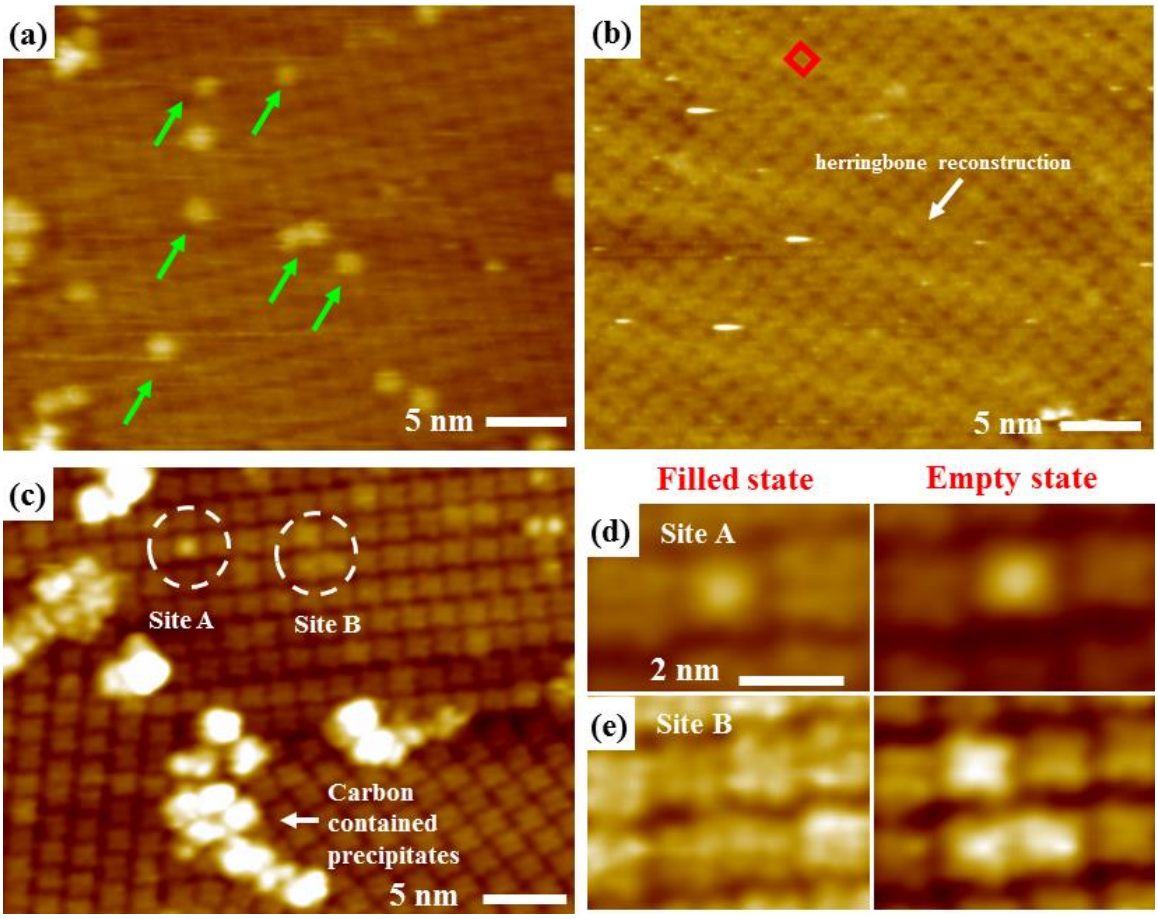

Figure 2.3. Empty-state STM images of a CuPc monolayer, after exposed NO_2 at 25 °C. (Vs = 2.0 V, It = 40 pA) (a) Exposing 1 ppm NO_2 for 5 min, then annealed at 50 °C for 20 min. the Chemisorbates are marked by green arrows. (b) After annealing sample in Fig. 2.3.(b) at 100 °C for 30 min. (c) Exposing 10 ppm NO_2 for 5 min, then annealing at 50 °C for 20 min. (d) and (e) Bias dependence of chemisorbates of site A and B. (Vs = ± 1.0 V, It = 40 pA.)

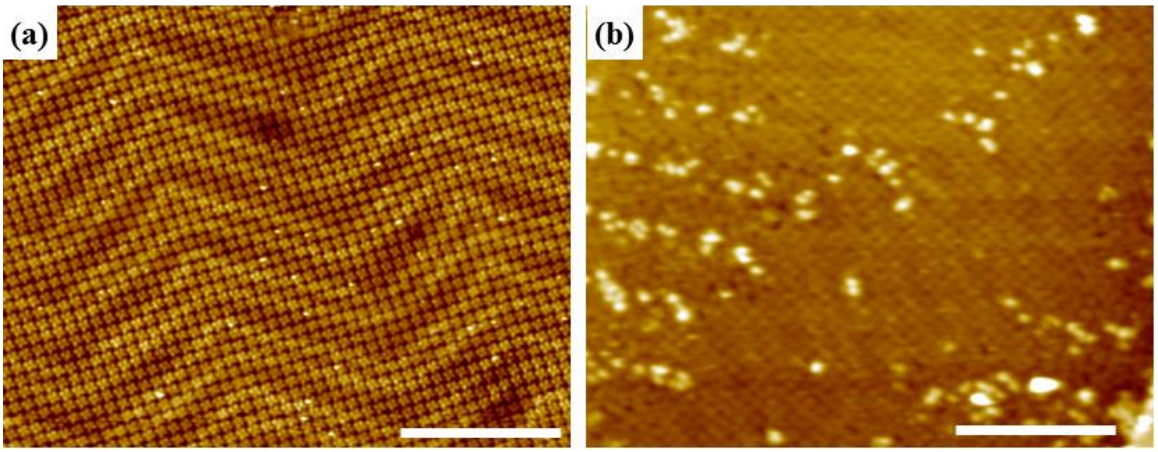

Figure 2.4. Empty state STM images of a CuPc monolayer surface. All scale bars are 20 nm. (a) bare CuPc monolayer surface. (Vs = 2.0 V, It = 10 pA) (b) After exposure to ambient air for 30 min and annealed at 50 °C for 10 min. (Vs = 2.0 V, It = 20 pA)

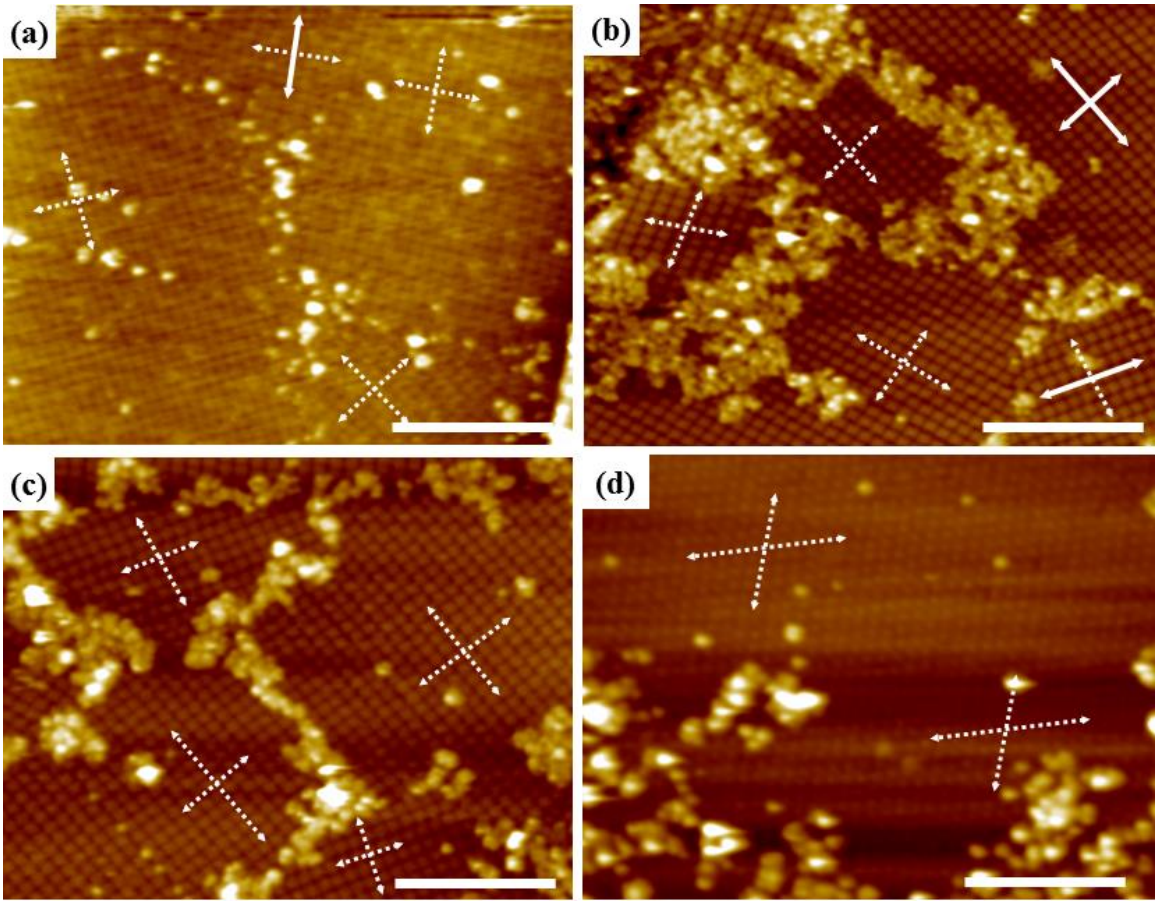

Figure 2.5. Empty state STM images of a CuPc monolayer surface after exposure high dose of NO_2. All scale bars are 20 nm. (Vs = 2.0 V, It = 40pA) (a) After exposure 10 ppm NO_2 for 5 min and annealed at 50 °C for 10 min. (b) CuPc monolayer from (a) annealed at 50 °C for an additional 10 min. (c) CuPc monolayer from (b) annealed at 50 °C for an additional 50 min. (d) CuPc monolayer from (c) annealed at 150 °C for further 6 h.

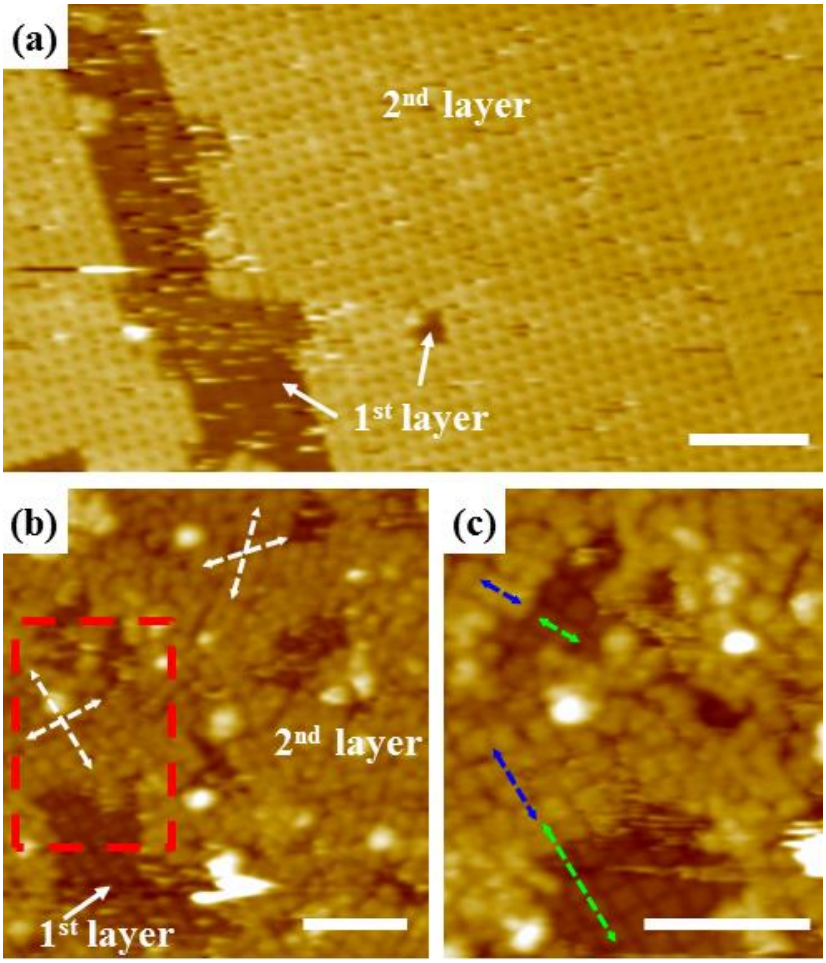

Figure 2.6. Empty state STM images of bilayer of CuPc. All scale bars are 10 nm. (a) Bare CuPc bilayer (Vs = 2.0 V, It = 10 pA). (b) Bilayer of CuPc, after exposure 10 ppm NO_2 for 5 min, then annealed at 50 °C for 1 h. (c) Expanded STM image from red rectangle in (b).

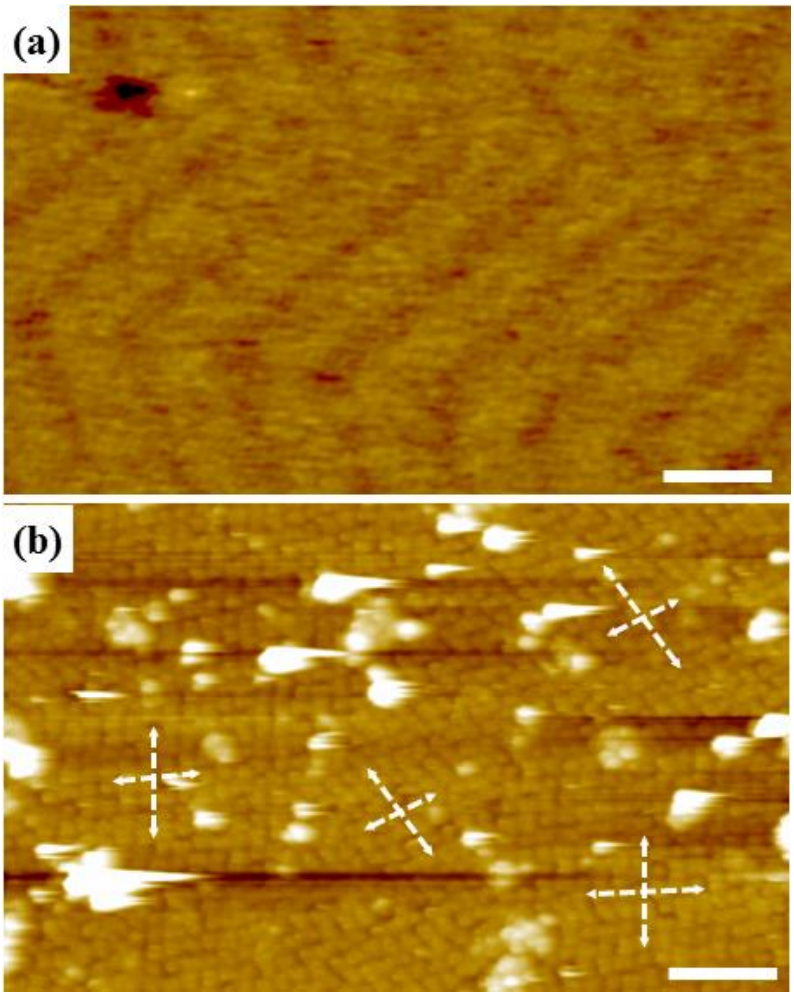

Figure 2.7. Empty state STM images of multilayer of CuPc. All scale bars are 10 nm. (a) Bare CuPc multilayer (Vs = 2.0 V, It = 10 pA). (b) CuPc multilayer, after exposure 10 ppm NO_2 for 5 min, then annealed at 50 °C for 1 h (Vs = 2.0 V, It = 40 pA).

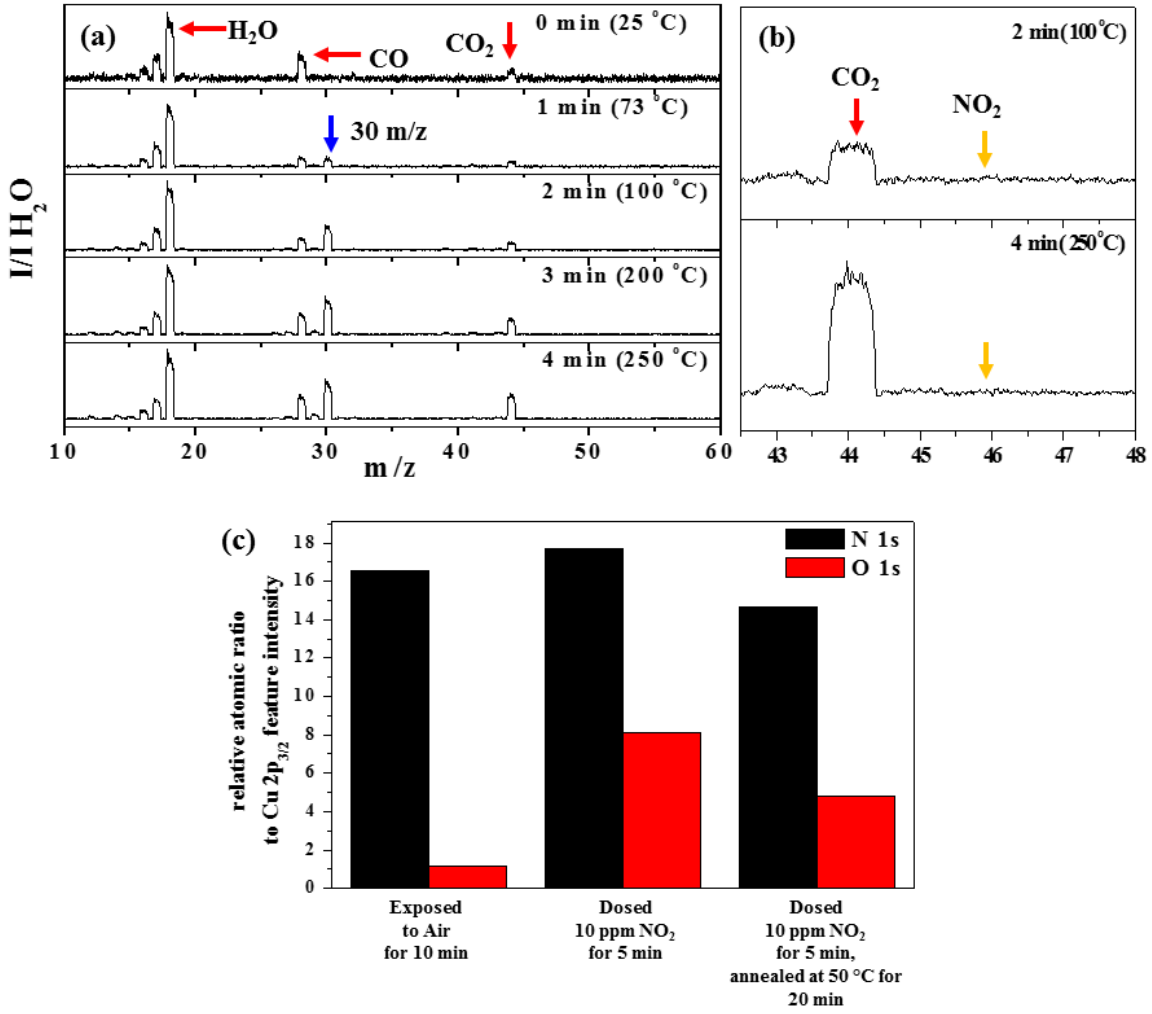

Figure 2.8. Mass spectrometry and XPS analysis of the NO_2/CuPc/Au (111) surface with flash desorption. (a) Detection of gaseous molecules in mass spectrum. The times indicate the duration of heating prior to recording the spectra at the temperatures. (b)Expanded spectrum from 42.5 to 48 m/z of (a). (c) Elementary coverage of N and O obtained from the relative XPS intensities.

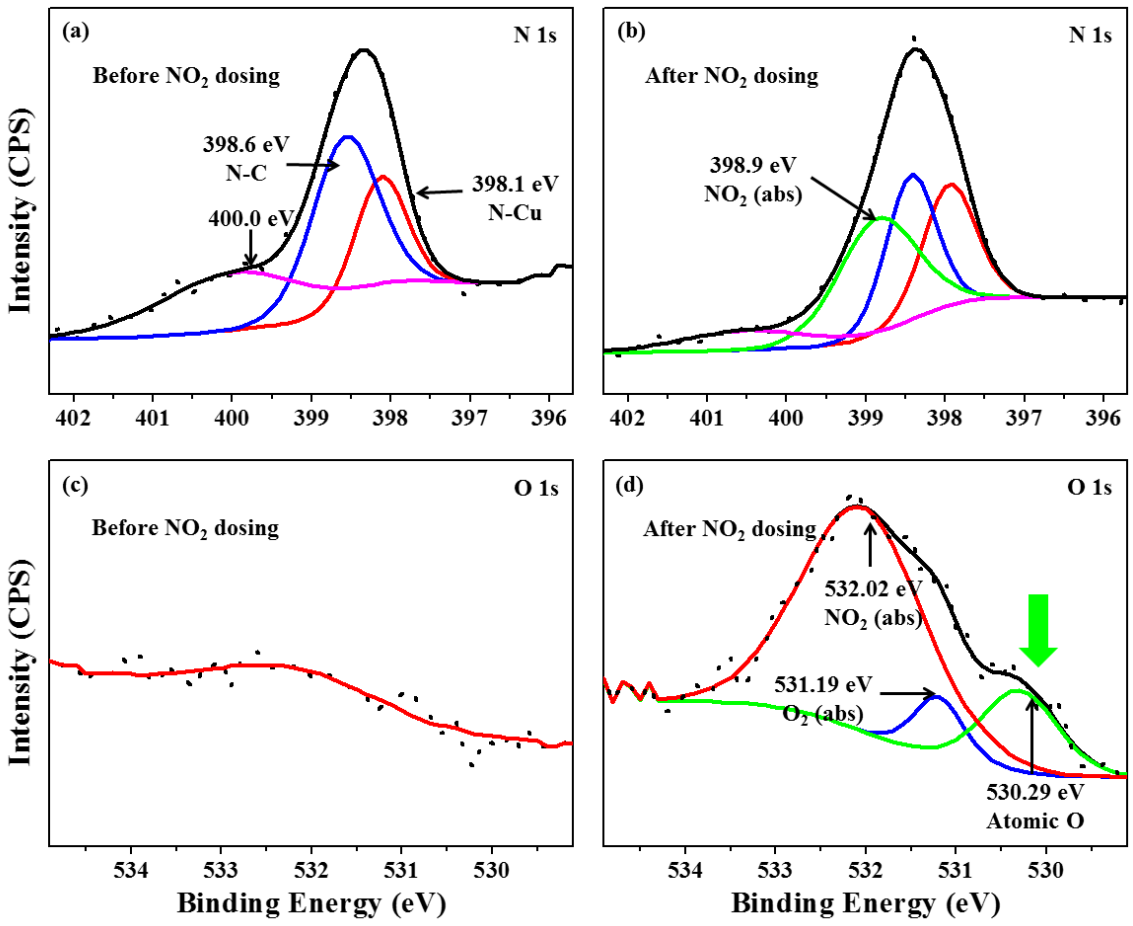

Figure 2.9. The spectra of XPS shown chemical states of of NO_2/CuPc/Au (111). (a) N 1s spectra taken from CuPc/Au(111) exposed to air for 10 min, (b) N 1s spectra taken from the NO2/CuPc/Au(111) is dosed with 10 ppm of NO_2 for 5 min and subsequently annealed at 50 °C for 20 min. (c) O 1s spectra taken from CuPc/Au(111) exposed to air for 10 min, (d) O 1s spectra taken from the NO_2/CuPc/Au(111) dosed with 10 ppm of NO_2 for 5 min and subsequently annealed at 50 °C for 20 min.

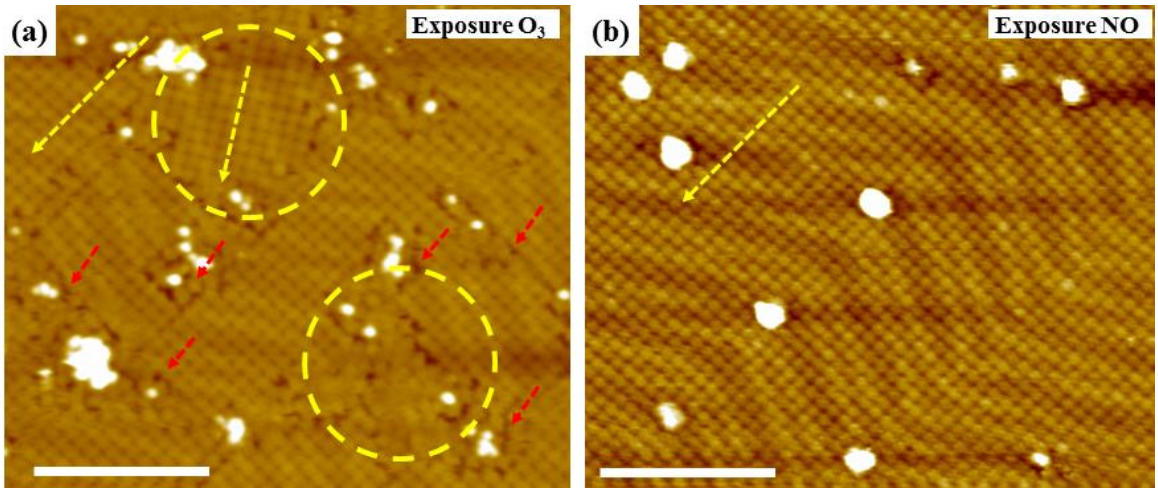

Figure 2.10. Empty state STM images of a CuPc monolayer dosed with a supersonic molecular beam source (MBS). All scale bars are 20 nm. (a) CuPc monolayer dosed with O_3 for 10 min at 25 °C (Vs = 2.0 V, It = 20 pA, f_{MBS} = 30 Hz). subsurface crack sites are marked by red arrows. (b) CuPc monolayer dosed with NO for 10 min at 25 °C (Vs = 2.0 V, It = 20 pA, f_{MBS} = 30 Hz).

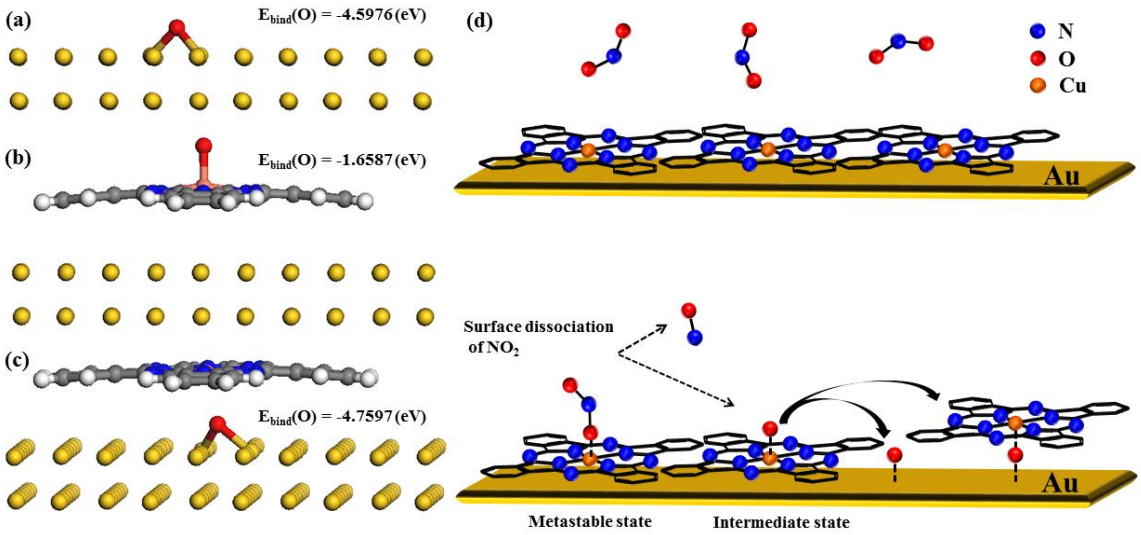

Figure 2.11. DFT calculations of CuPc/Au (111) with adsorption of atomic O on Au and CuPc. (a) Atomic O adsorbed on bare Au (111). (b) formation of O−CuPc/Au(111), while O is placed on top of the CuPc. (c) Formation of CuPc/O−Au(111) with placing O between CuPc and Au(111), i.e. subsurface adsorbate. (d) Schematic diagram for suggested mechanism of domain fracture induced by dissociative chemisorption of NO_2.

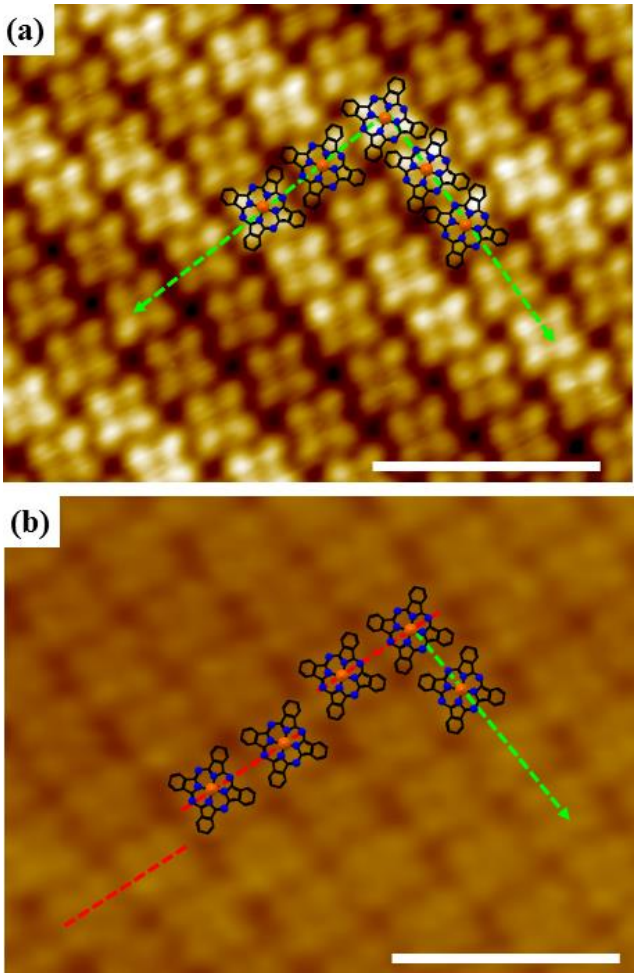

Figure 2.12. Empty state STM images of a CuPc monolayer surface. All scalecbars are 5 nm. (a) Bare CuPc monolayer (Vs = 2.0 V, It = 80 pA). (b) CuPc monolayer exposed with 10 ppm of NO_2 for 5 min at 25 °C and annealed at 50 °C for 20 min (Vs = 2.0 V, It = 40 pA). In both images, lines are drawn along the rows of CuPc (green arrow).

Table 2.1. Quantitative analysis of grain size of Mono-, Bi-, and Multilayers, after exposure 10 ppm of NO_2 for 5 min. The average grain size was estimated using the linear intercept method.

	Sample	Average domain size (nm)	Standard error	Standard deviation
Mono-layer	Clean surface	332	16	43
	Dosed and annealed at 50 °C, for 10 min	46.8	6	16
	Dosed and annealed at 50 °C, for 20 min	75.6	11	30
	Dosed and annealed at 50 °C, for 1hr 10 min	54.7	4	13
Bi-layer	Clean surface	357	17	45
	Dosed and annealed at 50 °C, for 1hr	38	4	10
Multi-layer	Clean surface	279	29	77
	Dosed and annealed at 50 °C, for 1hr	51	4	12

Chapter 3

Air Exposure Effects on Molecular Beam Epitaxy Grown WSe_2 Monolayers and Bilayers

3.1 Abstract

The effect of air exposure on 2H-WSe_2/HOPG is observed *via* scanning tunneling microscopy. WSe_2 was grown by molecular beam epitaxy on highly oriented pyrolytic graphite (HOPG), and STM images show that WSe_2 layers nucleate at both step edges and terraces of the HOPG. Exposure to air for 1 week and 9 weeks caused air-induced adsorbates to be deposited across entire WSe_2. however, the band gap of the terraces remained unaffected and nearly identical to those on de-capped WSe_2. The air-induced adsorbates can be removed by annealing at 523 K. In contrast to WSe_2 terraces, air exposure induced the edges of the WSe_2 to oxidize and form protrusions, inducing a larger band gap in the scanning tunneling spectra. The preferential oxidation at the WSe_2 edges compared to the terraces is likely the result of localized dangling bonds at the edge. In the absence of air exposure, the dangling bonds at edge have a smaller band gap compared to the terraces and a shift of Fermi level about 0.73 eV towards the valence band. However, after air exposure, the band gap of the oxidized WSe_2 edges became larger about 1.08 eV that of the WSe_2 terraces.

3.2 Introduction

To realize the potential applications of layered TMDs, such as optoelectronic or logic devices, layered TMD materials are typically exposed to ambient air during device fabrication; therefore, it is critical to elucidate the effect of air exposure on the structural and electronic properties of layered TMDs. However, although the impact of air stability of TMD materials to the transistors has been studied[111], the effect of air on the surfaces properties, such as the morphology or band structure, has not been fully understood at the atomic scale.

Here, the material properties of MBE-grown WSe_2, are characterized on the atomic scale by STM and spectroscopy (STS) at 100 K before and after air exposure, thereby elucidating the effects of air exposure on the morphology and electronic band gap of WSe_2. WSe_2 is have been intentionally studied, because of its electronic properties such as a large spin-orbit coupling of > 400 meV,[112] valley coherence,[113] and small direct-indirect gap crossover energy observed by photoluminescence[114]. In transistors of WSe_2, it is controlled by ambipolar behavior[27] with moderate ML mobility of ~250 cm^2/V-s, and bulk mobility as high as 500 cm^2/V-s.[25, 27, 115]

Based on the STM imaging, a very low defect density in the MBE WSe_2 is observed; this low density can be attributed to growth in high vacuum using high purity elemental sources. The electronic band gap (E_g) was determined for ML and bilayer (BL) WSe_2 using STS[42, 116]. Exposure of the MBE WSe_2/HOPG to the ambient air induced oxidation of the edges of WSe_2, as measured by STM and STS, while the terraces of WSe_2 remained nearly unchanged.

3.3 Experimental Details

HOPG substrates were gradually heated to 1073 K over 15 mins, held for 20 mins at 1073 K, and cooled to the growth temperature of 670 K. Once the growth temperature was stabilized, elemental tungsten (W) from an e-beam source and elemental selenium (Se) from a Knudsen cell

were dosed simultaneously to grow WSe_2. The growth conditions were designed based on prior MBE growth studies of $MoSe_2$[44]. A low W flux was employed, confirmed by the RHEED pattern appearance of the first layer WSe_2 after ~40 mins of growth. The Se flux was maintained at a beam equivalent pressure of $1.1x10^{-7}$ Torr. After growth, the sample was annealed under a Se flux first at 773 K for 3 mins and subsequently at 873 K for 7 mins. After annealing, the sample was cooled to 263 K under a Se flux to cap WSe_2 with approximately ~60 nm of Se to protect against ambient in transport to a separate UHV system for STM measurements.

The Se-capped WSe_2/HOPG samples, transported in a home-built vacuum case, were introduced into a UHV chamber through a load lock (base pressure: 5×10^{-8} torr) for performing STM/STS measurements. It is noted that the main and STM chamber were held $\leq 1 \times 10^{-10}$ torr and $\leq 5 \times 10^{-11}$ by ion pumping. Prior to STM and STS measurements, the Se capping layers were sublimated by annealing at 773 K for 3 hours; samples were heated to 773K with 15 K/min rate. After annealing the samples at 773 K, samples were cooled spontaneously.

STM imaging and STS measurements were performed by variable temperature (VT) STM in the UHV chamber (Omicron. Inc) at 100 K, using electrochemically etched W tips. After removing the Se capping layers from the WSe_2/HOPG samples, the samples were transferred to the STM stages. Afterwards, WSe_2/HOPG samples mounted into the STM stage were cooled to 100 K by liquid nitrogen. The differential tunneling conductance (dI/dV) of WSe_2 was probed by scanning tunneling spectroscopy at 100 K using standard lock-in modulation techniques. (lock-in modulation voltage: ΔV_{rms} = 20 mV, f = 500 Hz). In the STM system, the generation of tunneling current between the metal tip and the sample is induced by applying a bias to sample. Prior to the measurement of all STS spectra, a 2 V sample-tip bias was used in constant current imaging with 20~30 pA constant current, then the imaging and feedback loop were turned off and an I-V measurement was recorded while varying the tip to sample distance.

After verifying the as-decapped WSe_2 surfaces, WSe_2/HOPG samples were transferred from a UHV chamber into ambient air. After 9 weeks, the air-exposed WSe_2/HOPG samples were transferred into a UHV chamber, then annealed at 773 K to remove hydrocarbon and adsorbed H_2O or O_2 for stable STM and STS measurements. STM and STS on the air exposed WSe_2/HOPG samples was performed by the same methods as for the as-decapped samples.

3.4 Results and Discussion

3.4.1 Growth and atomic observation of WSe_2 deposited on HOPG *via* MBE

The STM images in Fig. 3.1 show that both HOPG step edges and terraces provide nucleation sites for WSe_2 growth. In Fig. 3.1.a, nucleation and growth at a multi-atomic step edge of HOPG is shown. Although some islands of WSe_2 grow on the terrace of HOPG, there is a complete coverage of WSe_2 along the HOPG step edges forming "sawtooth-shaped domains", indicated by the white arrows. Once WSe_2 is initially nucleated at both the upper and lower HOPG step edges, each WSe_2 layer grows laterally, propagating from the HOPG step edges to the internal HOPG basal planes. The position of this HOPG step edge is marked with a dashed orange line in Fig. 3.1.b. The height of the deposited WSe_2 is 0.79 ± 0.02 nm, consistent with the three-atomic-layer (Se-W-Se) thickness of single ML[27]. Comparing the height of ML WSe_2 on the upper HOPG terrace (purple arrow) to the height of ML WSe_2 on the lower HOPG terrace (yellow arrow), a 1.58 ± 0.03 nm height difference is calculated, indicating that a five-carbon-atomic-layer HOPG step edge nucleated the WSe_2 growth.

The step flow growth of WSe_2 at the HOPG step edges is not the only growth mode that occurs during MBE growth of WSe_2. Nucleation of WSe_2 can also occur on terraces of HOPG, as shown in Fig. 3.1.a, large islands of WSe_2 ML with variable lateral size (40 to 100 nm diameter) are observed on the HOPG terrace, likely facilitated by defects present on the HOPG terrace; and

BL growth is initiated at nearly the center of the WSe_2 ML islands. In summary, both HOPG step edges and terraces can provide nucleation sites to WSe_2.

The MBE-deposited WSe_2 layer has a hexagonal structure and low defect density, evident in the STM images in Fig. 3.2. In Fig. 3.2.a, STM image shows the Moiré pattern of ML WSe_2. The Moiré pattern is observed because the electron orbitals of WSe_2 and HOPG overlap, resulting in periodic potential wells that give rise to a hexagonal array of protrusions in the STM images and corresponding dots in the Fourier transform (FT).[117-118] Based on the Moiré pattern, the rotation angle is calculated to be ~2°. The atomic-resolution STM image and the associated FT image in Fig. 3.2.b reveal hexagonal arrays of the top Se layer of the three atomic planes in WSe_2. Although each atom has a different local density of states (LDOS), as shown by different brightness in the STM image, noticeable point defects or dislocations are not observed. The variation of LDOS can result from different interactions between WSe_2 and carbon atoms or defects states of the HOPG substrate. The lattice parameter of WSe_2 is measured about 0.32 ± 0.01 nm, in good agreement with previous crystal structure data.[119]

The quasi-particle band gap of ML and BL WSe_2 was measured using STS[45, 120-121]. Figure 3.2.c shows the averaged (dI/dV)/(I/V) *versus* V on a basal plane of WSe_2, far away from step edges of the second WSe_2 layer. The differential conductance dI/dV is normalized by dividing by I/V. [122] Each (dI/dV)/(I/V) is averaged from 10 individual dI/dV spectra. After converting into (dI/dV)/(I/V), a fitting method described in previous STM/STS studies was employed to extract the band gap.[122-123] As shown in below, the error is reported as the standard error obtained by the fitting process. It is noted that the uncertainties provided by the present fitting in STS are statistical uncertainties, using the least squares fitting.[124] Therefore, the given uncertainties can be much less than the thermal broadening in STS. Simulated fits to the STS data are included in Fig. 3.2.c as the dashed lines. From the dI/dV spectra on ML WSe_2, the conduction band minimum (CBM) is

estimated as +1.08 ± 0.02 V, while the valence band maximum (VBM) is estimated as -1.10 ± 0.01 V. Hence, the quasi-particle band gap for ML WSe_2 is determined to be 2.18 ± 0.03 eV, which is close to the reported theoretical value.[120] Employing the same method, the band gap of BL WSe_2 was also obtained; the CBM is positioned at +0.73 ± 0.01 V, while the VBM is located at -0.83 ± 0.01 V. Therefore, the band gap of bilayer WSe_2 is determined to be 1.56 ± 0.02 eV.[114, 121, 125] It is noted that in all of our measurements of ML and BL, the spectra reveal conductance extending from the band edges into the band gap, suggesting some sort of "band tail" states. The origin of this in-gap conductance is unknown at present; it greatly exceeds any effect of Fermi tails at 100 K in the STS measurements, which are fully included in the theoretical fit function.

3.4.2 Exposure of MBE grown WSe_2 in ambient air

To investigate the effect of air exposure on WSe_2/HOPG, the sample was removed from the UHV chamber and exposed to ambient air for 1 week. As shown in Fig. 3.3.a, air exposure-induced adsorbates, detected as bright features in STM, are present on both the terraces and step edges. As shown in the expanded STM image, Fig. 3.3.b, the diameter of the air induced adsorbates varies from ~1 to ~10 nm. It is reasonable to assume that hydrocarbons, H_2O and O_2 are adsorbed on the WSe_2 surface during air exposure. By comparing the band gaps measured in Figs. 3.3.c, it is clear that the air-induced adsorbates do not perturb the band structure of the ML and BL WSe_2; the band gaps of air exposed ML (2.15 ± 0.03 eV) and BL (1.62 ± 0.03 eV) are nearly identical to the band gap of pristine decapped WSe_2. Note that both ML and BL WSe_2 STS spectra were taken at locations within 1 nm of adsorbates. The air-induced adsorbates themselves (blue spectra in Fig. 3.3.c) have a smaller band gap than both ML and BL WSe_2; therefore, the adsorbates are more likely to be adsorbed hydrocarbon, H_2O or O_2 and not oxidation of WSe_2.

The air-induced adsorbates can be removed from WSe_2 surface by annealing, consistent with reversible adsorption of molecular chemisorbates. As shown in Fig. 3.4.a, annealing at 523 K for 30 mins induces desorption of most of the adsorbates from the WSe_2 terrace, indicating weak adsorbate binding. Only a few adsorbates remain along the step edge of WSe_2. As shown in Fig. 3.4.b, after desorption of adsorbates from the WSe_2 surface, the band gap of ML WSe_2 (2.10 ± 0.02 eV) does not change, compared the band gap of pristine WSe_2 ML (2.18 ± 0.03 eV) as shown in Fig. 3.2.c.

To mimic the asymptotic state of 2D materials during device process and testing, WSe_2/HOPG was also exposed to ambient air for 9 weeks. After air exposure, the sample was transferred into an UHV chamber and annealed at 773 K for 20 mins to remove ambient hydrocarbons, H_2O or O_2, thereby enabling stable STM and STS measurements. The large-area STM image in Fig. 3.5.a shows the air-exposed WSe_2 ML and BL on HOPG. In the atomic-resolution image of Fig. 3.5.b, the hexagonal crystal structure of the top Se layer is confirmed and there are no apparent defects, such as vacancies, dislocations or interstitial impurities. The FT image of Fig. 3.5.b displays prominent hexagonal peaks assigned to the topmost Se layer, consistent with the STM image. The band structure of the air-exposed WSe_2 ML is also confirmed by STS in Fig. 3.5.c; the VBM is -1.06 ± 0.03 V and the CBM is $+1.01 \pm 0.02$ V, giving a band gap of 2.07 ± 0.05 eV. Comparing the STS of the as-decapped WSe_2 ML terrace (2.18 eV), the band gap of the air exposed WSe_2 ML terraces decreased by only 0.11 ± 0.08 eV; therefore, the band gap of WSe_2 ML terrace remains nearly constant, even after air exposure for 9 weeks.

Spatial variations in the WSe_2 band structure are detected by measuring the dI/dV spectra from the bilayer WSe_2 to the edge of ML WSe_2 both before and after air exposure. First, the data before air exposure (*i.e.*, as-decapped, Fig. 3.6.a) are discussed. The black, dashed line on the STM image indicates the location along which the tunneling spectra were recorded. The black spectrum at the bottom of Fig. 3.6.a corresponds to the band structure of BL WSe_2, while the orange spectrum

at the top corresponds to the band structure of bare HOPG; the position of Fermi level (0 V) is marked as the purple dashed line. As the STM tip is moved from BL WSe_2 to ML WSe_2 to HOPG, STS spectra were acquired sequentially. Starting with BL WSe_2, two dI/dV spectra were recorded (black and red) with a band gap in the range of 1.54 ± 0.02 to 1.70 ± 0.03 eV. It is noted the STS curve closest to edge of WSe_2 BL (red curve) has a Fermi level slightly shifted towards the valence band. This shift could possibly arise from defect states near the edge of the WSe_2 BL. As the STM tip is moved towards the ML WSe_2 area adjacent to the edge of the BL WSe_2, the Fermi level shifts significantly away from the VBM. The measured band gap of the ML WSe_2 is in the range of 2.16 ± 0.02 to 2.23 ± 0.02 eV, as shown by the blue and green STS curves. At the step edge of the WSe_2 ML, the band gap decreases to 1.06 ± 0.04 eV and a large DOS is observed near the Fermi level. This edge state of WSe_2 will be discussed in further detail below. Beyond the step edge of ML WSe_2, a zero band gap is observed in the (dI/dV)/(I/V) spectrum (orange), consistent with the bare surface of HOPG. The symmetric linear dispersion of the measured LDOS on HOPG is consistent with prior STM/STS results.[38, 126-127]

A similar band structure transition from bilayer to monolayer also can be observed on the air-exposed WSe_2/HOPG, Fig. 3.6.b. In this case, spectra are also collected along the black dashed line shown in the STM image of Fig. 3.6.b. Here, an air-exposed WSe_2 island spans across a monoatomic HOPG step edge. Starting from the bottom spectra, two STS curves were obtained on air-exposed BL WSe_2, and both band gaps are similar to the band gap of the as-decapped WSe_2 BL in Fig 3.6.a. As the STM tip moves to the WSe_2 ML near the edge of the bilayer WSe_2, the band gap increases, consistent with that of the WSe_2 ML. However, when the STM tip is positioned on the WSe_2 ML located directly on monoatomic HOPG step edge, the band gap decreases to nearly 0 eV and a linear dispersion of the band structure is observed (pink curve). It is likely that the electronic structure of the WSe_2 ML is perturbed by the dangling bonds of underlying HOPG step edge. When the STM tip is moved far from the WSe_2 ML/HOPG step edge, the STS curves are

consistent with those representing the original band structure of the WSe_2 ML. Therefore, the spatially-resolved band structure measurements before and after air exposure show that the terraces of the MBE WSe_2 ML and BL appear to be nearly inert to the air exposure.

3.4.3 Partial oxidation of the edge in WSe_2

Although the terraces of WSe_2 are left nearly unaffected upon air exposure and UHV annealing, oxidation of the WSe_2 edges is observed. As seen in Fig. 3.7.a, the WSe_2 ML before exposure to ambient air (*i.e.* as-decapped) has clean and smooth step edges. However, after exposure to the ambient air and subsequent UHV annealing, the edges of the WSe_2 ML are decorated by air-induced protrusions, as seen in Fig. 3.7.b, with a height of 0.83 ± 0.03 nm, as shown in a line trace in Fig. 3.7.c.

The STS spectra in Fig. 3.8.a and 3.8.b shows that the air-exposed edge states have a larger band gap compared to the air-exposed terraces, consistent with the formation of a metal oxide with a relatively large band gap. In Fig. 3.8.a, both air exposed ML WSe_2 edge for 1 week (3.12 ± 0.02 eV) and for 9 weeks (3.15 ± 0.03 eV) have nearly identical band gap. As shown in Fig. 3.8.b, the (dI/dV)/(I/V) is displayed for both the air exposed WSe_2 ML edge and the air exposed WSe_2 ML terrace for 9 weeks so that the band gaps can be compared. As the position of STM tip is moved from terrace to edge, the VBM to Fermi level energy increases by 0.61 ± 0.04 V, while the CBM to Fermi level energy increases by 0.47 ± 0.04 V from 0 V; therefore, the band gap of the air-exposed edge is larger by 1.08 ± 0.08 eV than band gap of air exposed terrace. This 3.15 ± 0.03 eV band gap at the air exposed edge is very close to the theoretically calculated band gap of monoclinic WO_3 or the band gap of sub 2 nm WO_3 quantum dots.[128-130] Combining STM and STS results, it can be concluded the air exposure of WSe_2/HOPG induces selective oxidation of WSe_2 edges.

To better understand the oxidation process in air, the bare WSe_2 edges were characterized with STM and STS before air exposure (*i.e.*, the as-decapped WSe_2). In Fig. 3.9.a, typical WSe_2 ML and BL edges are displayed in empty-state STM imaging; both ML and BL possess smooth, clean edges. However, a higher resolution filled-state image of the edge of WSe_2 BL in the purple square in Fig. 3.9.a, reveals a bright rim along the edge, shown as a white dashed line in Fig. 3.9.b. From a filled-state STM image, the line trace indicates the height of the edge contour as 0.28 ± 0.02 nm, which is similar in height to dangling bonds on the Si (001) surface.[131-132]

As shown in Fig. 3.9.c, two major differences are observed in the STS spectra taken at the edge of WSe_2 compared to bare WSe_2 terraces. First, the DOS at the VB (approximately -1 V sample bias) is increased at the edge of the WSe_2 ML (blue arrow). This increase is consistent with the increased brightness of the terrace edges in the filled-states STM images in Fig. 3.9.b. The STS spectrum acquired at the edge indicates a band gap of 1.1 ± 0.04 eV, with the Fermi level located relatively close to the valence band. Comparing as-decapped WSe_2 edge with the air-exposed WSe_2 ML edge, the band gap of the air-exposed edge is increased three times from the band gap of as-decapped edge. These differences in the band structure at the step edges indicate the existence of new electron states.

Based on the STM and STS data, two schematic models for these new states along the WSe_2 edge are proposed in Fig. 3.9.d. In case I, the dangling bonds from the atoms at the WSe_2 edge might form enhanced VB states which are observed as a bright corrugation in the filled state STM image, similar to dangling bonds on Si (001) surface.[131-132] In case II, dangling bonds cause the condensation of Se adatoms which form the thin layer at the step edge. Both models share the common feature of electronic edge states along the outmost atoms at the WSe_2 edge. However, the observation of electronic edge state (case 1) is consistent with previous STM measurements and DFT calculations on MoS_2 nanocrystals showing that the edge of MoS_2 has a metallic band structure, resulting in high reactivity with other molecules or catalytic activities.[133-137] Moreover,

previous DFT calculations on MoS_2 nanoclusters show that the DOS at edges is larger near the Fermi level than the DOS of terraces in projected p-orbital DOS[136]. Therefore, it seems most likely that the WSe_2 edge states are due to electronic defects of the edge atoms (case I), rather than excess Se adatoms (case II).

Based on the STM/STS results on WSe_2 edges, together with previous DFT and experimental data, it is hypothesized that the WSe_2 electronic edge states resulting from dangling bonds that facilitate air-induced reactions. In ambient air, the dangling bonds of outmost atoms are passivated by adsorption of H_2O, O_2 or hydrocarbon molecules. Although both Se and W are expected to oxidize to SeO_x and WO_x respectively, SeO_x (selenium oxide) has desorption temperature much less than 773 K,[138-139] and therefore the SeO_x products will desorb during UHV annealing at 773 K, leaving WO_x at the edge. Because the oxidized and annealed edge states have high thermal stability, they persist after the UHV anneal and can be detected by STM as protrusions decorating the edges of the WSe_2. The basic model of air exposure and subsequent annealing forming WO_x at step edges is consistent with all the STM and STS data.

3.5 Summary

Molecular beam epitaxy was used to grow WSe_2 on HOPG, and layers were subsequently characterized by STM and STS. The samples were capped by excess 20 nm Se adlayer after growth and decapped for STM imaging. High-resolution STM images show almost no observable vacancy defects and dislocations on decapped WSe_2, except near step edges. High-resolution filled-state STM images revealed a distinct corrugation along the as-decapped WSe_2 edges, while STS displayed narrower band gap and shifted Fermi level toward the valence band compared with locations in the center of the terraces. To investigate effects of air exposure on WSe_2 layers, the WSe_2/HOPG was exposed to ambient air for 1 week and 9 weeks. STM images reveal that the

terraces of WSe_2 are nearly unaffected; although air induced adsorbates are deposited across the WSe_2 surface, the band gap of air-exposed WSe_2 ML is measured as 2.07 ± 0.05 eV, nearly identical to 2.18 ± 0.03eV prior to air exposure, and atomic resolution STM images display a hexagonal array of topmost Se layer without noticeable defects after the air exposure and UHV annealing. In contrast, the WSe_2 edge is oxidized by exposure to ambient air, involving a topographic transition along the edge and a large band gap (3.15 ± 0.03 eV) of the edge, as measured by STS. The selective reaction at the step edges results from the existence of dangling bonds at the WSe_2 edge, which was confirmed by STM and STS. Present results suggest air exposure of WSe_2 results in oxidation of the WSe_2 edge, while the terrace of WSe_2 is nearly inert to ambient air; therefore, air oxidation of WSe_2 can potentially passivate the electronic edge states thus minimizing leakage current or electron-hole recombination *via* the conductive edge states in pristine WSe_2, which is desired in devices.

3.6 Acknowledgements

This work is supported by NSF Grant DMR 1207213, NSF Grant ECCS 1433490, NSF Grant DMR14-00432, AFOSR, and LEAST-STARnet, a Semiconductor Research Corporation program, sponsored by MARCO and DARPA and by SRC NRI SWAN.

Chapter 3, in part or in full, is Reproduced with permission from “Jun Hong Park, Suresh Vishwanath, Xinyu Liu, Huawei Zhou, Sarah M. Eichfeld, Susan K. Fullerton-Shirey, Joshua A. Robinson, Randall M. Feenstra, Jacek K. Furdyna, Debdeep Jena, Huili Grace Xing, and Andrew C. Kummel. Scanning Tunneling Microscopy and Spectroscopy of Air Exposure Effects on Molecular Beam Epitaxy Grown WSe2 Monolayers and Bilayers. ACS Nano 2016, 10, pp 4258−4267.” Copyright [2017] American Chemical Society. The dissertation author was the primary investigator and author of this paper.

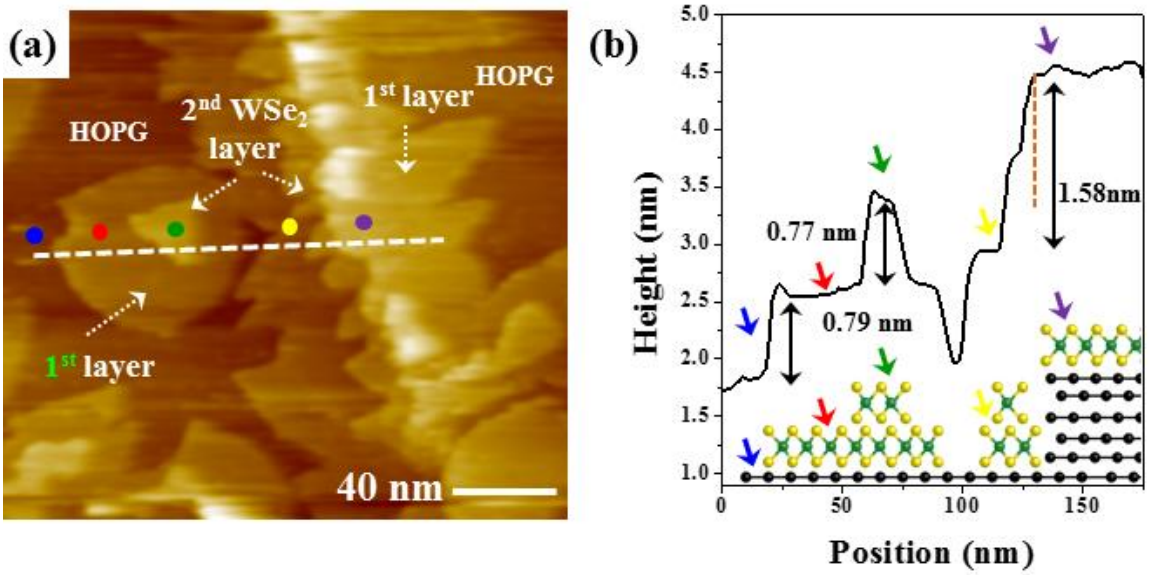

Figure 3.1. (a) Large area STM images of WSe_2 growth on HOPG. (b) Corresponding line trace along the dashed line in (a).

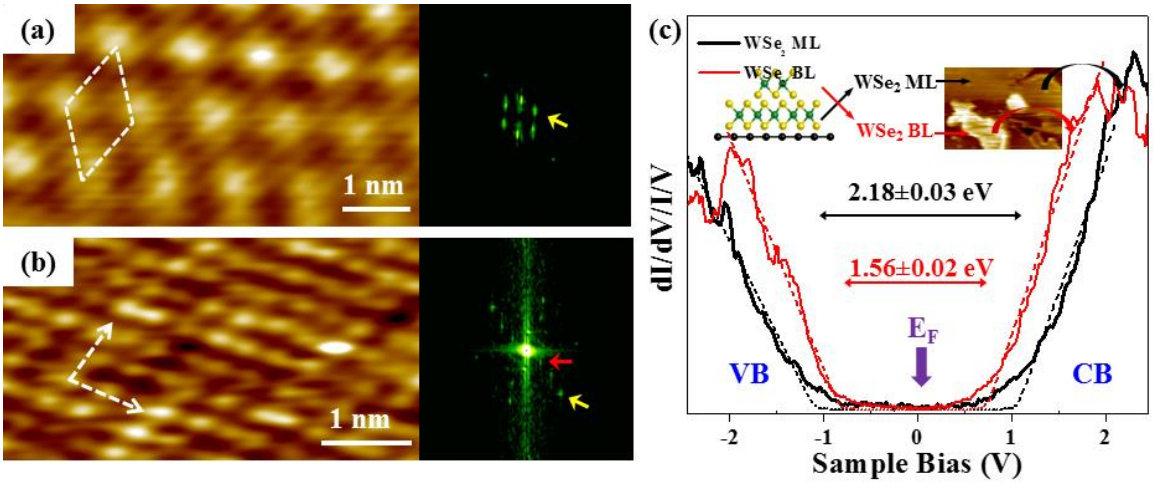

Figure 3.2. Atomic resolution STM image and STS of decapped MBE WSe_2 on HOPG. (a) Hexagonal moiré pattern and corresponding Fourier transform (V_{sample}: 2 V, I_T: 60 pA). (b) Atomically resolved STM showing arrays of Se atoms in WSe_2 and corresponding Fourier transform (Vsample: 1.5 V, IT: 80 pA). (c) STS ((dI/dV)/(I/V)) of ML (black) and bilayer (red) WSe_2.

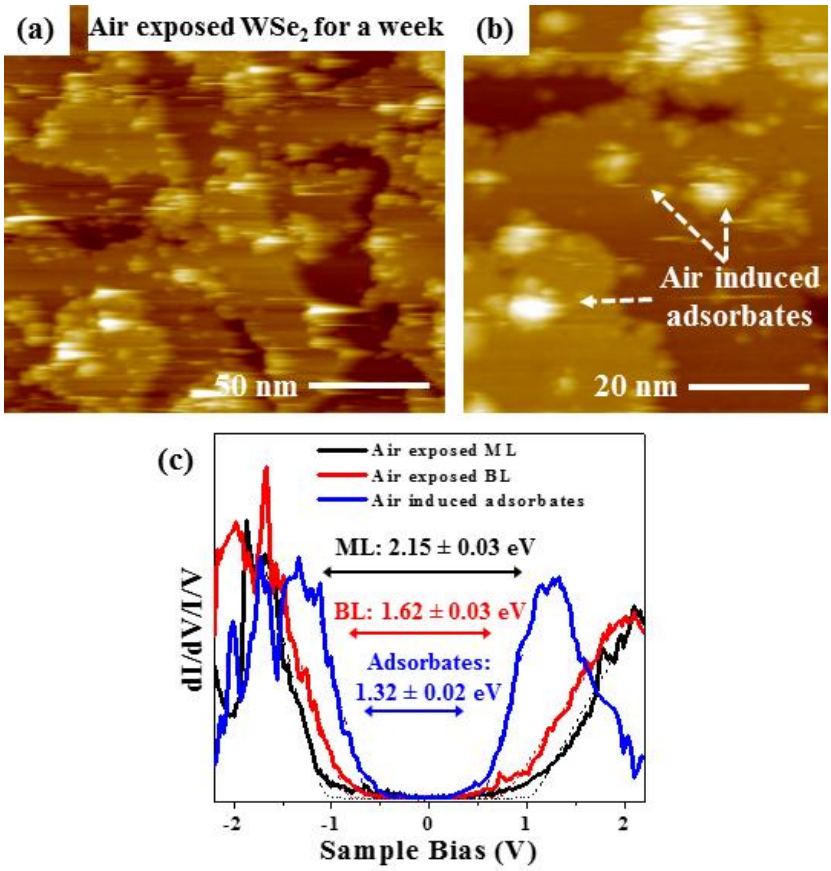

Figure 3.3. Empty state STM image of WSe_2/HOPG after air exposure for 1 week. (a) Large area STM image of the air exposed WSe_2 surface (V_{sample}:2 V, I_t: 10 pA), before annealing. (b) Zoomed STM image of the WSe_2 surface exposed to air for 1 week (V_{sample}: 2 V, I_t: 20 pA). (c) STS of air exposed ML and BL WSe_2 and adsorbates.

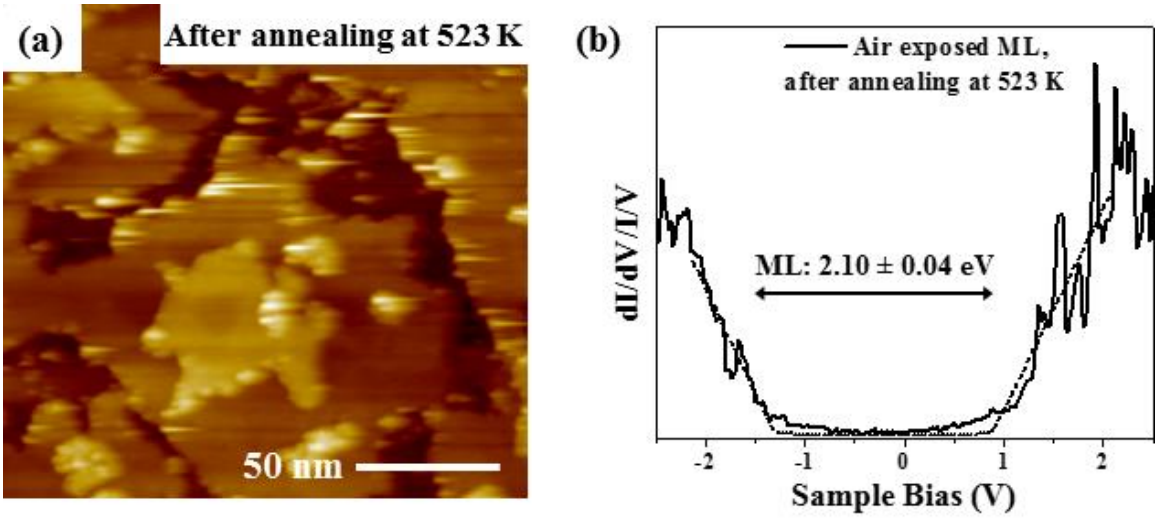

Figure 3.4. (a) After annealing at 523 K for 30 min, STM image of air exposed WSe_2 surface (V_{sample}: 2 V, I_t: 10 pA). (b) After annealing at 523 K for 30 min, STS of air exposed ML WSe_2.

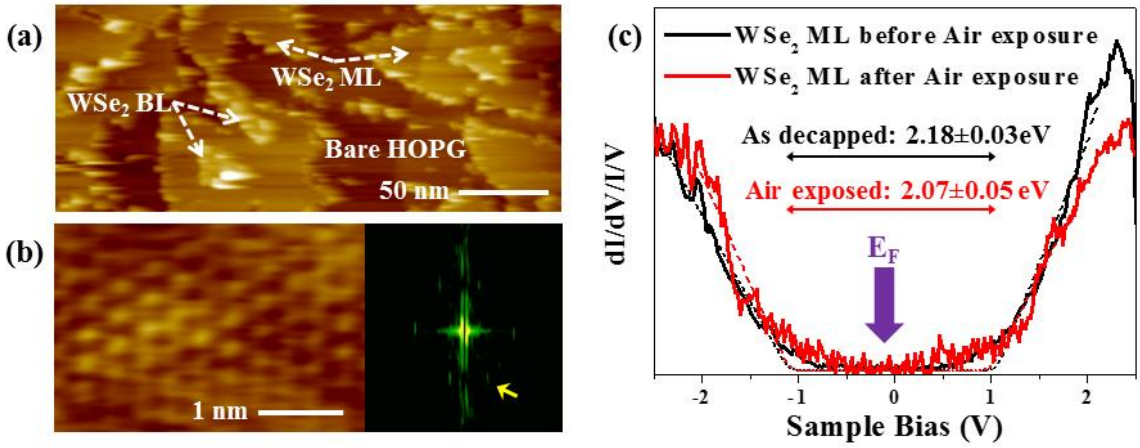

Figure 3.5. (a) Large area empty state STM image of WSe_2 surface exposed to air for 9 weeks (V_{sample}: 2 V, I_t: 15 pA). (b) Atom resolved STM image of a WSe_2 ML terrace after air exposure

(V_{sample}: −1 V, I_t: 120 pA) and corresponding Fourier transform. (c) STS of a WSe_2 ML before and after air exposure.

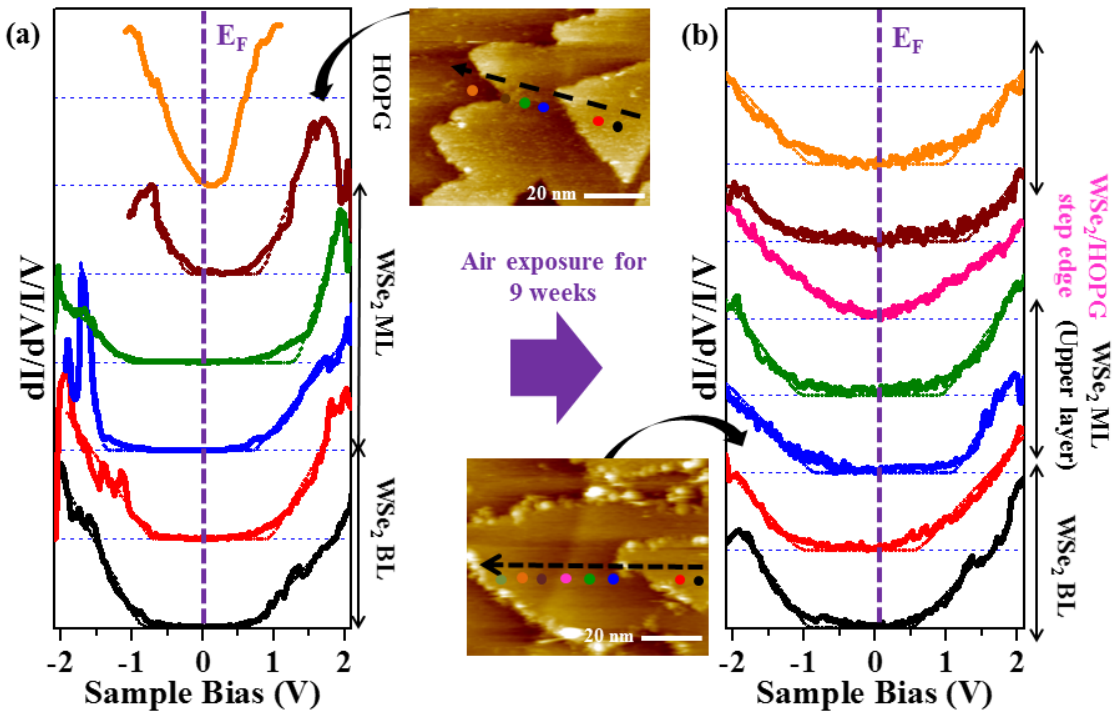

Figure 3.6. (a) Subset of (dI/dV)/(I/V) spectra recorded along the dashed black line in the STM image, before air exposure. (b) Subset of (dI/dV)/(I/V) spectra recorded along the dashed black line in the STM, after air exposure.

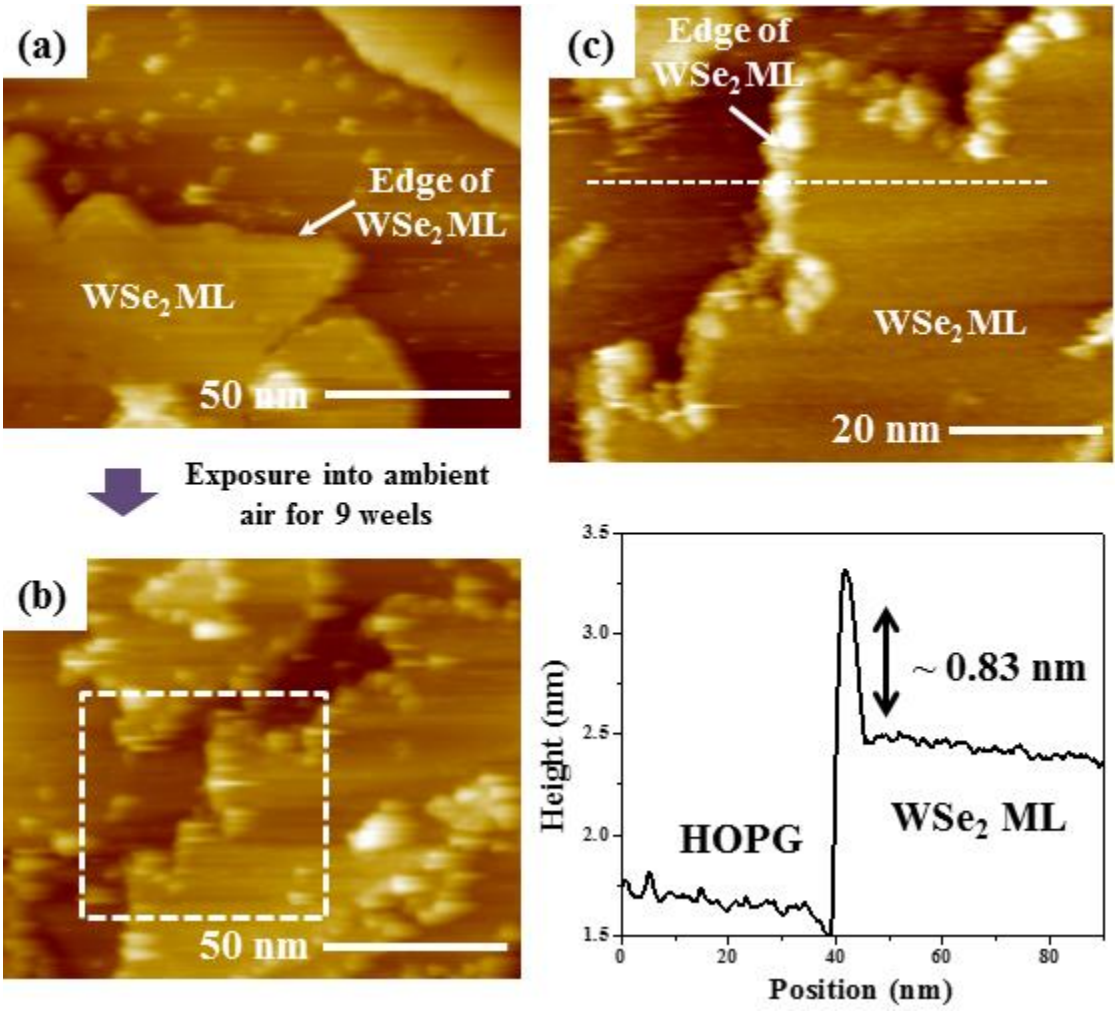

Figure 3.7. Empty state STM image of the WSe_2 edge after exposure for 9 weeks to ambient air, after annealing in UHV. (a) STM image of decapped WSe_2. Surface (V_{sample}: 2 V, I_t: 20 pA). (b) STM image of air exposed WSe_2 (V_{sample}: 2 V, I_t: 15 pA). (c) Expanded STM image of the white rectangle from (b) and corresponding line trace (V_{sample}: 2 V, I_t: 20 pA)

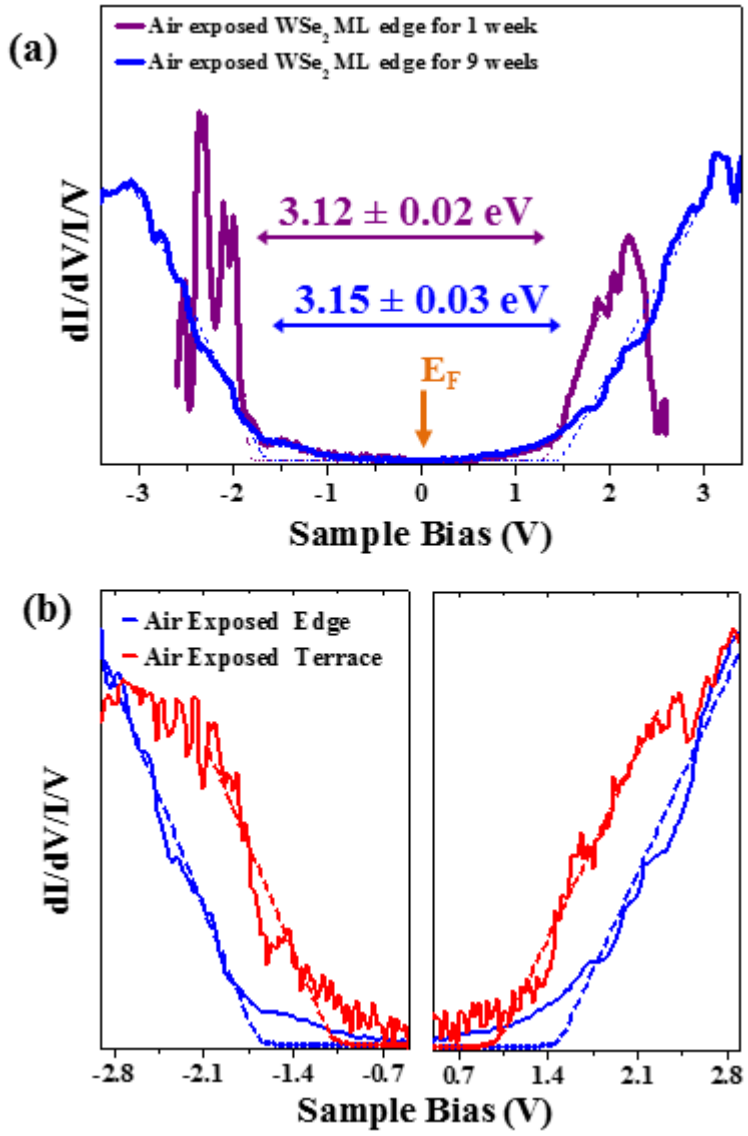

Figure 3.8. (a) (dI/dV)/(I/V) recorded at the WSe_2 ML edge exposed to air for 1 and 9 weeks. (b) Closed view of STS near band edge from −2.9 to −0.5 V and from 0.5 to 2.9 V.

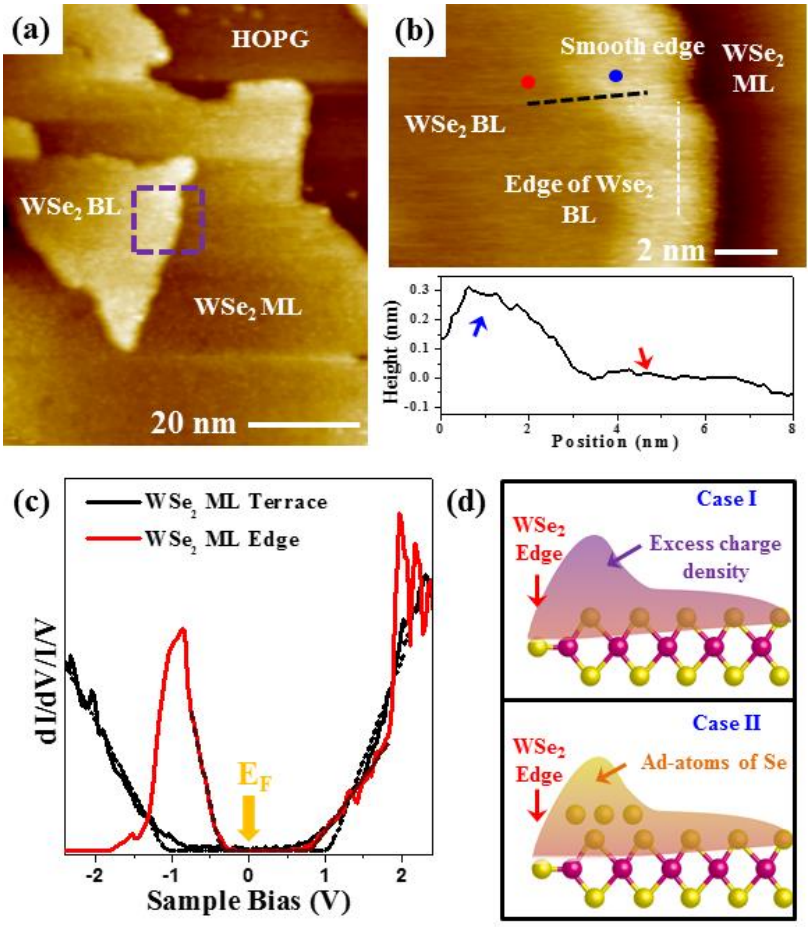

Figure 3.9. Empty state STM and STS of WSe_2 edges, before air exposure. (a) Large scale STM image of the edge of the WSe_2 ML before air exposure (V_{sample}: 2 V, I_t: 20 pA). (b) Zoomed STM images of the purple rectangle in (a) (V_{sample}: −1 V, I_t: 40 pA) and corresponding line trace along the dash line. (c) STS spectra recorded at the edge of the WSe_2 ML and the terrace of the WSe_2 ML, before air exposure. (d) Proposed schematic of WSe_2 edges before exposure to air.

Chapter 4

Dielectric Deposition of Ultrahigh Nucleation Density on Two-Dimensional Surfaces

4.1 Abstract

Several proposed beyond-CMOS devices based on two-dimensional (2D) require the deposition of thin dielectrics between 2D layers. However, the direct deposition of dielectrics on 2D materials is challenging due to their inert surface chemistry. To deposit high-quality, thin dielectrics on 2D materials, a flat lying titanyl phthalocyanine (TiOPc) monolayer, deposited via the molecular beam epitaxy, was employed to create a seed layer for atomic layer deposition (ALD) on 2D materials, and the initial stage of growth was probed using in-situ STM. ALD pulses of trimethyl aluminum and H_2O resulted in the uniform deposition of AlO_x on the TiOPc/HOPG. The uniformity of the dielectric is consistent with DFT calculations showing multiple reaction sites are available on the TiOPc molecule for reaction with TMA. Capacitors prepared with 50 cycles of AlO_x on TiOPc/graphene display a capacitance greater than 1000 nF/cm^2. These TiOPc seeding layer also can be employed on WSe2 surface for uniform deposition of dielectrics.

4.2 Introduction

Complementary metal–oxide–semiconductor (CMOS) technology based on Si has been implemented for logic devices due to its outstanding performance and low cost. However, as CMOS devices are scaled down to a few nanometers, the maximum density of devices is limited by the power consumption of each device. To develop alternative, low-voltage devices with steeper subthreshold swing than the 300 K thermodynamic limit of 60 mV/decade, devices with graphene as the channel material are being explored[24, 140]. Graphene has high carrier mobility and stability;

therefore, most research has been focused on graphene devices based on in-plane transport[24, 140-142]. However, due to the zero band gap of graphene, such devices cannot be turned OFF, and are hence not directly useful for CMOS architectures.

An alternative approach uses vertical junctions in a 2D/insulator/2D geometry, relying on charge transfer out of the plane and offering potential for low OFF-state power consumption. Device structures such as the Bilayer pseudo-Spin Field-Effect Transistor (BiSFET) and the interlayer tunneling FET based on 2D materials have been proposed[31, 143-153]. Although the layout of each device is different, all device models share a common vertical 2D/I/2D structure. In order to fabricate these vertical junctions, a high quality ultrathin (1~2 nm) insulating layer must be inserted between two 2D layers[144-148, 150-152, 154-156]. Although graphene/insulator/graphene junctions with mechanically exfoliated hexagonal boron nitride have shown negative differential resistance (NDR) when appropriately biased[149, 155, 157], there are still few reports of NDR due to the poor reproducibility[146-147, 150, 155]. Moreover, the mechanical transfer of exfoliated layers and subsequent assembly of stacks requiring rotational alignment are unrealistic for large-scale device production[155]. To overcome these challenges, atomic layer deposition (ALD) has been proposed to deposit a dielectric[150-151, 156, 158-159]. However, most of the previous research on ALD dielectrics on 2D materials has focused on thick layers (> 10 nm) because most 2D materials do not have dangling bonds, and thin dielectrics give rise to large pinhole densities[160-166]. Although the initial growth stage is critical to deposit pinhole-free, thin dielectrics, the direct observation of ALD nucleation on 2D materials has not yet been reported at the atomic level because ALD precursors are readily transformed into an oxide in ambient air and easily transfer from 2D materials to STM tips even at low temperatures.

To nucleate ultra-thin dielectrics uniformly on 2D materials, titanyl phthalocyanine (TiOPc) molecules are deposited on graphite and graphene as a template for ALD dielectrics. Each step of the deposition of both TiOPc and the dielectric are observed at the molecular scale with *in-*

situ STM in ultrahigh vacuum to overcome the extreme reactivity of the ALD precursor in ambient air. Using the TiOPc seed layer, graphene capacitors and FETs were fabricated to evaluate the electrical properties of the deposited dielectrics. Combing in-situ observation, the growth of thin dielectrics on TiOPc/graphene can be extended to interlayer FETs based on transition metal dichalcogenides (TMD)[31, 167-170].

4.3 Experimental Details

Highly oriented pyrolytic graphite (HOPG) was purchased from SPI supplies (Structure Probe, Inc). TiOPc was purchased from Sigma Aldrich and purified by multiple sublimations. To obtain a clean surface, HOPG samples were exfoliated multiple times in air. Monolayer graphene films were grown by chemical vapor deposition (CVD), and transferred onto highly N-doped SiO_2/Si substrates. After loading into the UHV deposition chamber, both the HOPG, and graphene samples were heated to 750 K for 3 h to remove volatile organic contaminants and other adsorbates. A thick overlayer of TiOPc was deposited on clean HOPG or graphene at 373 K using organic molecular beam epitaxy (MBE) with a differentially pumped effusion cell (Eberl MBE-Komponenten). Subsequently, the thick multilayer was heated to 523 K for 6 min, and a flat-lying TiOPc monolayer was formed. ALD reactions on the TiOPc monolayer were performed with an *in-situ* ALD system attached to the UHV system to avoid air exposure. The TiOPc/HOPG was transferred from the UHV chamber to the ALD chamber *via* a load-lock chamber, without breaking vacuum. After exposure to trimethyl-aluminum (TMA) of various pulse durations (70 ms to 360 mS) and H_2O pulses of 500 ms duration at 373 K, the samples were transferred back to the STM stage, again without air exposure.

STM and STS were performed at 100 K with an Omicron VT STM system with etched tungsten tips. Capacitors were fabricated using CVD-grown graphene, while dual-gated FETs were

fabricated on exfoliated, monolayer graphene on Si/SiO_2 using e-beam lithography (50 nm Ni top gate contacts). Both the graphene capacitors and FETs were annealed at 623 K for 8 h in vacuum (~ 1×10^{-6} Torr) to remove resist residue remaining from device fabrication. The cleaned samples were transferred into the UHV chamber to deposit a TiOPc seed layer. Afterwards, these samples were transferred in ambient air to a commercial ALD reactor (Beneq) to form the AlO_x/TiOPc/graphene/SiO_2/Si stack. After dielectric deposition, Ni was deposited on AlO_x/TiOPc graphene/SiO_2/Si as the top-gate using a thermal evaporator. All electrical measurements were performed with a probe station in ambient conditions. Density functional theory (DFT) calculations were carried out using the Vienna *ab-initio* simulation package (VASP).

4.4 Result and Discussion

4.4.1 Deposition of TiOPc seedling layer.

A highly ordered TiOPc monolayer is deposited on HOPG by UHV-MBE as confirmed by STM. A schematic diagram of the TiOPc molecular structure is shown in Fig. 4.1.a. Figure 4.1.b shows an empty-state STM image with a defect-free monolayer of TiOPc deposited on HOPG with long-range order. Although most of the STM experiments in this study have been done on graphite, both graphite and graphene surfaces are inert due to sp^2 hybridization[166] and can therefore be considered equivalent for this study. The Fourier Transform (FT) of Fig. 4.1.b is provided in the inset, where a distinct set of peaks is consistent with an array of single-phased crystalline TiOPc. Each individual TiOPc molecule has a bright spot at its center, assigned to O, and darker surrounding features assigned to the aromatic rings, indicating that the TiOPc molecules face vacuum to form a flat-lying monolayer. As shown in previous reported DFT calculations, the outer benzene rings of TiOPc molecules provide weak π-π^* interaction with the substrate, while the

central O and N are negatively charged, thereby providing potential binding sites for polar adsorbates[171].

DFT calculations show that TiOPc on graphene does not induce major electronic perturbation in the band structure of graphene close to the Dirac point. Figure 4.1.c shows the band structures of both graphene (left) and TiOPc/graphene (right) with the position of the Fermi level marked by a blue dashed line. After deposition of the TiOPc monolayer on graphene, new band states corresponding to TiOPc are generated; however, the symmetric linear dispersion of the graphene band structure, which is critical for a vertical junction, are nearly unchanged[148].

4.4.2 In-situ observation in growth of dielectric on TiOPc/HOPG

After verifying the deposition of an ordered seed layer of TiOPc, AlO_x dielectric was deposited using ALD. TMA exposure to TiOPc/HOPG for 70 ms at 373 K induces chemisorbate islands, as illustrated in the empty state STM image in Figure 4. 2.a consistent with the dissociation of TMA into dimethyl aluminum (DMA). Note, the dissociation of TMA can occur even at 300 K, indicating that there are dissociated chemisorbates on the TiOPc/HOPG after exposure to TMA at 373 K[172-173]. After TMA exposure, there is no apparent periodicity, and the surface comprising an adsorbate/TiOPc complex has features of varying height and spacing. As shown in the inset of Fig. 4.2.a, the FT of the STM image shows diminished peak intensity compared to the FT of unreacted TiOPc/HOPG of Fig. 4.1.a. The chemisorbate/TiOPc complexes have an average spacing of 1.25 ± 0.05 nm, which is less than the spacing between bare TiOPc molecules on HOPG, consistent with multiple binding states for the ALD precursor on a single TiOPc molecule.

Because the TiOPc monolayer is highly reactive to TMA, high-density AlO_x nucleation on TiOPc/HOPG results even after just one pulse of TMA and H_2O. Formation of stoichiometric Al_2O_3 requires a post-annealing step, and therefore the aluminum oxide formed on the surface is denoted

as AlO_x[174-175]. As shown in STM image of Fig. 4.2.b, after one ALD cycle with a TMA pulse of 360 ms on TiOPc/HOPG at 373 K, AlO_x appears as a cluster on each unit cell, without noticeable pinholes. The inset FT in Fig. 4.2.b shows only a bright contour around the center indicating an amorphous structure for AlO_x/TiOPc/HOPG. The monolayer of AlO_x appears as a nearly continuous film with no discernable pinholes in the STM images. This coverage indicates that the TMA reacts with each TiOPc molecule, and further addition of H_2O induces transformation of the adsorbates to AlO_x.

Scanning tunneling spectroscopy (STS) was employed to determine the transitions in electronic structure induced by sequential ALD pulses, as shown in Fig. 4.2.c. A variable tip-surface STS method was employed to collect a larger tunneling signal during STS measurements[122]. The TiOPc monolayer on HOPG has a band gap of about 1.7 eV and an almost symmetric density of states (DOS). After exposing TiOPc to TMA, the DOS in the valence and conduction bands significantly decreased and the band gap increased to about 2.5 eV. However, in the STS of Fig. 4.2.c, two band gap states (s1 and s2) still remain at -0.5 and -1.2 V, which are below the E_F, indicating charge trapping in DMA/TiOPc/graphene.

DFT was used to model possible charge movements as shown in Fig. 4.3.a and 4.3.c. As DMA reacts with the central O of TiOPc, a large change in the DFT PDOS of DMA/TiOPc is observed. The new states are generated near the Fermi level at -0.1 and +0.75 eV (red bars and arrows), while there is a decrease of preexisting states at -1 and +0.35 eV (blue bars and arrows). Therefore, this transition of DOS in DMA/TiOPc is consistent with the experimental observation of trap states below the Fermi level, as shown in the STS measurements. In STS, these band gap states are diminished by the following H_2O pulse. After 1 cycle of ALD at 373 K, the band gap increased to about 3.4 eV, and most of the states within the band gap are removed.

DFT calculations suggest the existence of multiple stable binding sites (O, N and C) for DMA on TiOPc molecules, which is required for high nucleation density after one ALD cycle. All

sites can bond DMA at 373 K to convert into AlO_x during ALD. Combining STM images of Fig. 4.3, a simplified model is proposed in Fig. 4.4; Initially, TMA dissociates into DMA and chemisorbs onto TiOPc, bonding to O, N, or C sites at 373 K. Therefore, multiple DMA molecules coexist on each TiOPc molecule after the first TMA pulse. Subsequently, the H_2O pulse transforms the $Al(CH_3)_2$ into $Al(OH)_2$ and induces cross-linking of Al-O-Al similar to what is observed on Si(100)[172]. Finally, after exposing the TiOPc/HOPG to multiple cycles of ALD, AlO_x begins to grow between the TiOPc molecules, consistent with the AFM images in the bottom right.

The deposition of a subnanometer dielectric on TiOPc/HOPG significantly decreases the surface tunneling conductance between the STM tip and the sample. A schematic of the tunneling junction between the metal STM tip and AlO_x/TiOPc/HOPG is displayed in Fig. 4.5.a. The tunneling current measured as a function of sample bias for both TiOPc/HOPG and ALD deposited TiOPc/HOPG (1 and 5 ALD cycles) are shown in Fig. 4.5.b, and nine different STS IV curves after 1 cycle and 5 cycles ALD are included in Fig. 4.5.c. For TiOPc/HOPG, an increasing current is measured for both positive and negative sample biases, producing a V-shaped I-V plot with high currents. In contrast, after 1 cycle of TMA/H_2O, the tunneling current decreases throughout the bias range by more than one order of magnitude compared to the bare TiOPc/HOPG, while the offset position is shifted to a positive bias. The reduced tunneling current is attributed to the energy barrier introduced by the subnanometer AlO_x layer, resulting in a decreased probability of tunneling electrons. It is noted that the shift of the offset bias in STS results from trap or fixed charge states in dielectric or at the interface of dielectric-TiOPc, because these dielectrics were processed without post-deposition annealing. Therefore it is possible there are excess oxygen or defects states in dielectric[174-175]. The tunneling current further decreases by an order of magnitude after 5-cycles of ALD in Fig. 4.5.b. In this case, the low current regime expands to a larger voltage range. As the thickness of the insulating dielectric increased due to additional ALD cycles on TiOPc/HOPG, increasing the tunnel barrier width, the tunneling of charge carriers from the metal tip (sample) to

sample (tip) requires applying higher bias thereby the onset bias is pushed to a higher voltage range, as shown by an orange arrow. This shift of onset bias is more prominently shown in the nine different IV curves taken after 1 and 5 cycles ALD/TiOPc/HOPG in Fig. 4.5.c. It is noted that although the current of 1 cycle ALD/TiOPc/HOPG ($1.4x10^{-4}$ to $1.87x10^{-4}$ nA) is slightly lower in the flat regions of the I-V curves than the current of 5 cycles ALD/TiOPc/HOPG ($1.5x10^{-4}$ to $2.5x10^{-4}$ nA) in Fig. 4.5.b, the current levels of both samples are very low in the flat regions of the I-V curves, therefore this difference is within the noise level of the measurement. As shown in Fig. 4.5.c, both 1 cycle and 5 cycles ALD/TiOPc/HOPG possess the similar variation of current levels (from $1x10^{-4}$ to $3x10^{-4}$ nA) in the flat region of the I-V curves as displayed by the red bars.

4.4.3 Electric characteristics of deposited dielectric on TiOPc/graphene

Figure 4.6.a shows the schematic of Ni/AlO_x/TiOPc/graphene capacitors fabricated on SiO_2/Si, with 50 cycles of ALD. The V-shape of the CV curves in Fig. 4.6.b is due to the effect of the quantum capacitance of graphene[176-177]. Previous reports have mostly employed thick dielectric layers (8~20 nm) to measure CV due to limitations imposed by large pinhole densities in thin layers[164]. However, since the AlO_x/TiOPc/graphene has a very low pinhole density compared to previous reports, thinner capacitors could be fabricated even with conventional thermal metal gate deposition. At -3 V, the maximum capacitance (C_{max}) is over 1000 nF/cm^2 at 1 kHz, which is larger than prior reported values on graphene[162, 164-165]. Instead C_{max} reported here is consistent with InGaAs with 4.7 nm of Al_2O_3[178]. The contact resistance between graphene and the Au contact is manifest by the difference of C_{max} between 1 and 2 kHz[179-180]. Moreover, near zero capacitance is observed at 0 V, which results from low minority carriers at the interface, indicating the full modulated capacitance by gate bias. The leakage current in the capacitor is shown in Fig. 4.6.c to be around 0.02 A/cm^2 at a gate bias of +/- 3 V. As shown below, small area devices have a lower

leakage current per unit area, which is consistent with leakage being limited by particulate-induced pinholes resulting from graphene grain boundaries[39].

To further evaluate the quality of the 4 nm dielectric, dual-gated, exfoliated graphene FETs were fabricated as shown in Fig. 4.7.a. In this case, 40 cycles of AlO_x/TiOPc were deposited. A Ni top gate was deposited on AlO_x/TiOPc/graphene/SiO_2/Si, and a highly N-doped Si substrate was used as a back gate, allowing dual-gate control of the carrier concentration in graphene. The leakage current of the FET is below 10^{-7}A/cm^2 within a top gate bias range of -1 to +1 V, as shown in Figure 4.7.b. This leakage current is much smaller than previous leakage values in thicker ALD-deposited Al_2O_3 on graphene (previous leakage value: about 2.2 x 10^{-6} A/cm^2 in 4.5 nm Al_2O_3 and 1.9 x 10^{-7} A/cm^2 in 15 nm Al_2O_3)[163, 181]. The resistance is measured at V_{BG} = 0 V over a top gate range of +/- 1V in Fig. 4.7.c. The position of maximum resistance (Dirac point) of the device is at V_{TG} = 0.17 V for the forward sweep, while the reverse sweep shifts the Dirac point to 0.05 V, giving rise to a 0.12 V hysteresis. Compared to previous reports, the positions of the Dirac points are closer to 0 V and the hysteresis is smaller[141, 163, 181] suggesting the TiOPc seed layer and subsequent dielectric deposition does not induce a significant amount of chemical doping or interfacial trap defects.

Figure 4.7.d shows resistance as a function of back gate bias (-50 to 50V) for varying top gate biases in the range of -0.3 to 0.3 V. From the device schematic in Fig. 4.7.a, it can be seen that while the back-gate can modulate the entire graphene channel, the top-gate can only modulate the local channel region under the top-gate. Therefore, the modulation of the top and bottom gates induces shifts of Dirac point originating from the graphene channel, as shown in Fig 4.7.d. As V_{TG} is varied, the carrier density in the top-gated region changes, and can be neutralized by applying an appropriate V_{BG}[163, 182]. At 0, V_{TG} are detected: one at V_{Bg} = 0 V, which is the primary Dirac Point, and a second at V_{Bg} ~ 40 V. These two “Dirac Points” results from the coexistence of a top gated dielectric/graphene region (A) and an open dielectric/graphene region (B) as shown in Fig. 4(d). Since only region A is affected by the top-gate, the primary Dirac Point corresponding to this region

would shift when the top-gate voltage is changed, while the secondary Dirac point remains at 40 V. At V_{TG} = -0.3 V, the large peak located at V_{BG} = 40 V is when the top-gate is biased in such a way that the Primary Dirac point overlaps with the Secondary Dirac point, and causes a "series addition" of the two resistances, leading to a large peak, which appears as a single Dirac point.

Figure 4.7.e shows a two-dimensional plot of the channel resistance as a function of the back-gate bias (V_{BG}), and top-gate bias (V_{TG}). The variation of both Primary and Secondary Dirac point is displayed in Fig. 4.7.e. The slope along the variation of Primary Dirac points represents the ratio of capacitances of the top-gate and back-gate as shown dashed line. From the slope of the V_{BG} vs V_{TG} for channel resistance, the capacitance ratio is calculated as 105 from the equation slope = $V_{TG}/V_{BG} = C_{TG}/C_{BG.}$ The back-gate capacitance is ~ 11 nF/cm^2 for a 300 nm back-gate SiO_2 oxide; therefore, the top-gate capacitance is calculated as 1155 nF/cm^2.

4.4.4 Deposition of dielectric on TMDs using TiOPc seedling layer

The TiOPc seedling layer also can be employed to deposit uniform Al_2O_3 on TMDs. To develop the process, a ML of TiOPc was deposited on the MBE-grown WSe_2 on HOPG, and the empty-state STM image in Fig. 4.8.a shows a defect-free and highly ordered layer. No domain boundaries, large-scale defects, or second-layer growth of TiOPc are observed, indicating a flat-lying and single-crystalline order in the TiOPc ML. As shown in the molecularly resolved STM image of Fig. 4.8.b, the O atom is located on top of the central Ti atom; the polarity of the TiOPc molecule arises from binding of this O with the central Ti. The STM image of TiOPc in Fig. 4.8.b is slightly distorted by the thermal drift during STM imaging; however, a square lattice of TiOPc molecules is clearly observed. This single-crystalline square lattice is confirmed by the Fourier transform, shown in the inset of Fig. 4.8.b, where four-fold symmetry indicated by nine distinct peaks is observed. The four-fold crystalline structure of the TiOPc ML on WSe_2/HOPG is clearly

distinguished from the honeycomb lattice structure of WSe_2 on HOPG. It is noted that in the present observation, the desorption temperature of a TiOPc ML on WSe_2 (523 K) in the UHV chamber is lower than the desorption temperature of a TiOPc ML on HOPG (623 K); annealing of TiOPc/WSe_2 above of 523 K results in the degradation of the TiOPc crystal structure. Therefore, it follows that the TiOPc ML has a weaker van der Waals interaction with WSe_2 than with HOPG[183].

STS measurements of WSe_2/HOPG with and without TiOPc are used to determine how the surface electronic structure is changed upon TiOPc deposition, as shown in Fig. 4.8.c. The STS spectra on the TiOPc ML were recorded at the center of the molecules. The STS spectra show that the bare WSe_2/HOPG band gap is 2.05 ± 0.04 eV, and the Fermi level is positioned near the center of the band gap. The Fermi level is marked by the purple arrow at 0 V. TiOPc increases the density of states (DOS) both at the valence band and conduction band, as indicated by the blue arrows, indicating a smaller band gap (1.44 ± 0.03 eV). Moreover, the Fermi level is positioned near the conduction band, indicating the WSe_2/TiOPc stack is *n*-type characteristics. It is noted that although the TiOPc/WSe_2/HOPG has a smaller band gap than WSe_2/HOPG, there are no midgap state and deposition of a gate oxide may remove the band edge states since they can be due to weakly bound charge which is eliminate by oxide bonding[183]. A previous STS of Al_2O_3 deposition on TiOPc/HOPG showed that a few monolayers of Al_2O_3 increased the band gap as measured by STS.

After verifying the TiOPc seedling layer on MBE grown WSe_2 *via* STM, the Al_2O_3 was deposited on the TiOPc/WSe_2 surface by the ALD process. It is noted that the bulk WSe_2 samples were employed for atomic force microscopy (AFM) and conductive AFM (C-AFM). Uniform deposition of Al_2O_3 on the bulk WSe_2 at 393 K assisted by a TiOPc seedling layer is confirmed by atomic force microscopy (AFM). Figures 4.9.a and 4.9.b show topographic differences of ALD Al_2O_3 on bulk WSe_2 with and without the TiOPc seedling layer using the same ALD growth conditions. Because the ideal surface of WSe_2 (defect free surface) does not possess dangling

bonds, ALD nucleation occurs at defects or step edges. Figure 4.9.a shows that the resulting surface has 5.5 nm deep pinholes with diameters at the 100 to 500 nm scale and root mean square (RMS) surface roughness of 3.6 nm. In contrast, for the sample that includes a ML TiOPc seeding layer, the Al_2O_3 attaches uniformly on the TiOPc/WSe_2 without pinholes, as shown by the AFM image and the associated line trace in Fig. 4.9.b. As a result of the elimination of pinholes in the Al_2O_3/TiOPc/WSe_2 stack, the RMS roughness is decreased by more than a factor of 20 to 0.15 nm. This RMS roughness value is less than one third of the RMS roughness obtained using a remote O_2 plasma-assisted, 120 cycle ALD Al_2O_3 film on MoS_2.[184]

Integrating the TiOPc seeding layer into the ALD process also decreases the gate leakage current, as shown in Fig. 4.9.c. Leakage current was measured by conductive AFM (C-AFM) in a dark box on a sample for which Al_2O_3 was deposited with and without the TiOPc seed layer, using conductive plateau AFM tips (Nanosensors: PL2-NCH). For the sample without TiOPc, the diameter of the AFM tip is sufficiently small (1.8 μm) that it can contact the WSe_2 through pinholes in the Al_2O_3. Because the WSe_2 surface is electrically conductive, the current measured through a pinhole reaches the 10 nA compliance of the system. Conversely, because there are no detectable pinholes in the Al_2O_3/TiOPc/WSe_2 stack, the C-AFM tip only contacts the Al_2O_3 and the leakage current is reduced by more than two orders of magnitude. It is noted that the current does not return to zero at zero volts in the Al_2O_3/TiOPc/WSe_2 heterostructure. For a sweep rate from minus to plus of 0.5 V/sec, the minimum current is observed at 3.5 V indicating some charging of traps. However, because the traps are likely present on the air-exposed oxide surface, they may be removed during gate metal deposition during FET fabrication.

4.4 Summary

The deposition of a dielectric layer with a high nucleation density was demonstrated by using a TiOPc seed layer prior to ALD. *In-situ* STM was employed to image each step of the process with molecular resolution. The TiOPc layer has long-range order and shows high reactivity with TMA; after exposure to TMA for 70 ms at 373 K, TMA dissociatively chemisorbs on TiOPc/HOPG resulting in multiple chemisorption sites. After exposure to 1 cycle ALD pulse, the high coverage of AlO_x is obtained without noticeable pinholes. STS measurements show that 1 cycle of ALD on TiOPc/HOPG increases the band gap from 1.7 to 3.4 eV, while the tunneling current is decreased by one order magnitude. These results are consistent with the formation of a subnanometer oxide. DFT calculations show that O, N and C sites of the TiOPc molecules have high binding energy with DMA, consistent with the existence multiple reaction sites per single TiOPc molecule. With capacitor and dual-gated devices, the dielectric shows insulating properties with high-quality CV and RV characteristics. The combination of high-quality subnanometer dielectric deposition and *in-situ* measurements provides a pathway for large-scale fabrication of 2D interlayer devices, which can be extended to other 2D crystals and devices.

4.5 Acknowledgments

This work is supported in part by the National Science Foundation Grant DMR 1207213, by the Center for Low Energy Systems Technology (LEAST), a STARnet Semiconductor Research Corporation (SRC) program sponsored by MARCO and DARPA, and by the SRC Nanoelectronic Research initiated through the South West Academy of Nanoelectronics (SWAN).

Chapter 4, in part or in full, is Reproduced with permission from “Jun Hong Park, Hema C.P. Movva, Evgeniy Chagarov, Kasra Sardashti, Harry Chou, Iljo Kwak, Kai-Ting Hu, Susan K. Fullerton-Shirey, Pabitra Choudhury, Sanjay K. Banerjee, Andrew C. Kummel. In Situ Observation

of Initial Stage in Dielectric Growth and Deposition of Ultrahigh Nucleation Density Dielectric on Two-Dimensional Surfaces. Nano Letters, 2015, 15 (10), pp 6626–6633." Copyright [2017] American Chemical Society. The dissertation author was the primary investigator and author of this paper.

Chapter 4, in part or in full, is Reproduced with permission from "Jun Hong Park, Sara Fathipour, Iljo Kwak, Christopher F. Ahles, Suresh Vishwanath, Huili Grace Xing, Susan K. Fullerton- Shirey, Alan Seabaugh, Andrew C. Kummel. Atomic Layer Deposition of Al2O3 on WSe2 Functionalized by Titanyl Phthalocyanine. ACS Nano, 2016, 10 (7), pp 6888–6896." Copyright [2017] American Chemical Society. The dissertation author was the primary investigator and author of this paper.

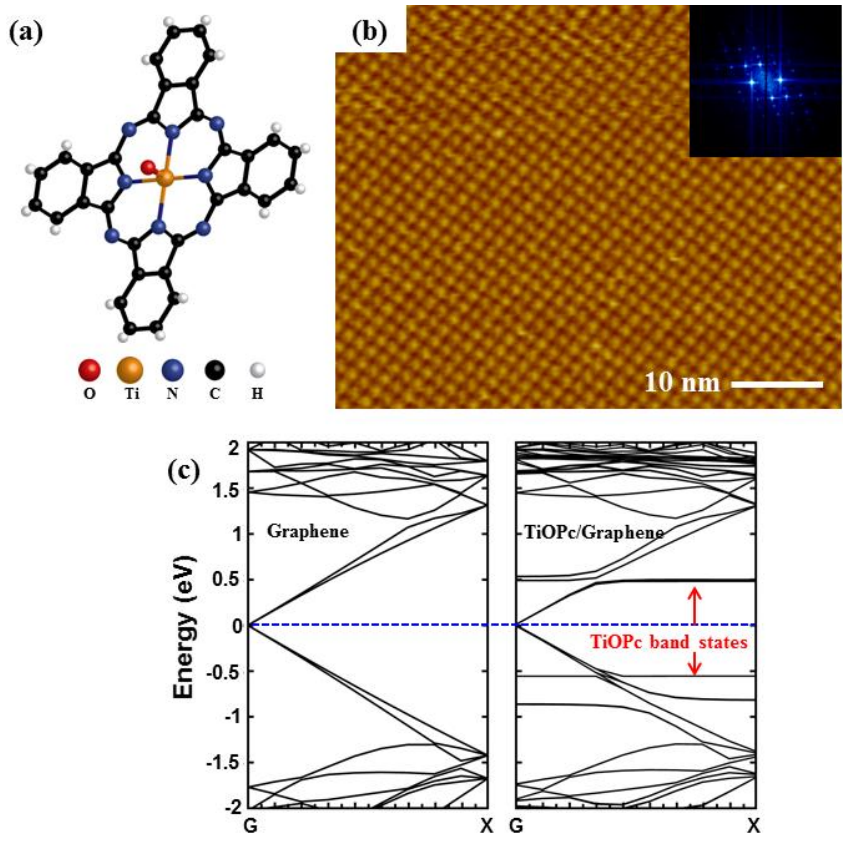

Figure 4.1. Empty state STM images of monolayer TiOPc on HOPG and band structure of graphene and TiOPc/graphene. (a) Schematic model for the molecular structure of TiOPc. (b) Bare TiOPc monolayer deposited on HOPG. The inset shows the corresponded Fourier transform (FT). (V_S = +2.0 V, I_T = 20 pA) (c) DFT band structure of graphene before (left), and after deposition of TiOP on graphene (right).

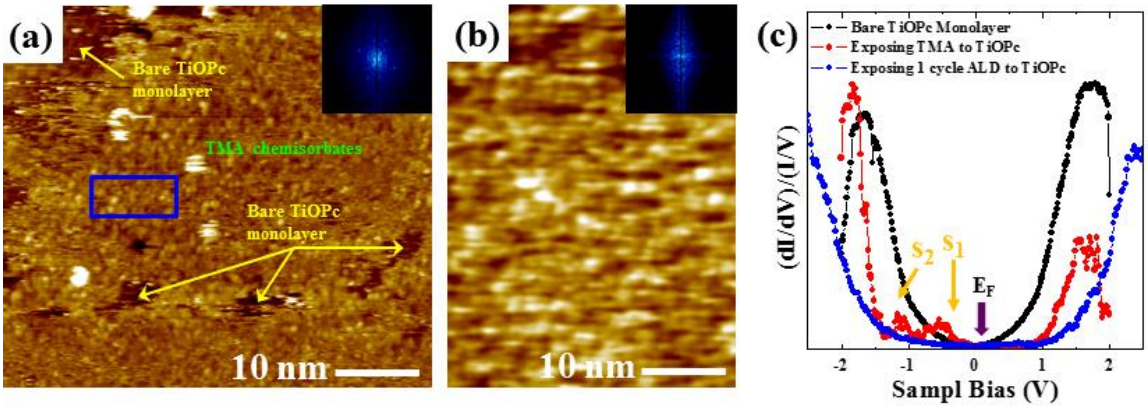

Figure 4.2. Topographic and electronic transitions of TiOPc/HOPG as an exposure of TMA. (a) TiOPc monolayer exposed to TMA for 70 mS at 373 K. (V_S = +2 V, I_T = 20 pA) The inset shows the corresponded Fourier transform (FT). (b) TiOPc/HOPG monolayer exposed to 1 cycle of ALD at 373 K with TMA for 360 ms and H_2O for 500 ms. (V_S = +3 V, I_T = 20 pA) The inset shows the corresponded FT of the AlO_x/TiOPc. (c) STS dI/dV/I/V spectrum of bare, exposed TMA, and one cycle of ALD pulse (TMA + H_2O) on TiOPc monolayer.

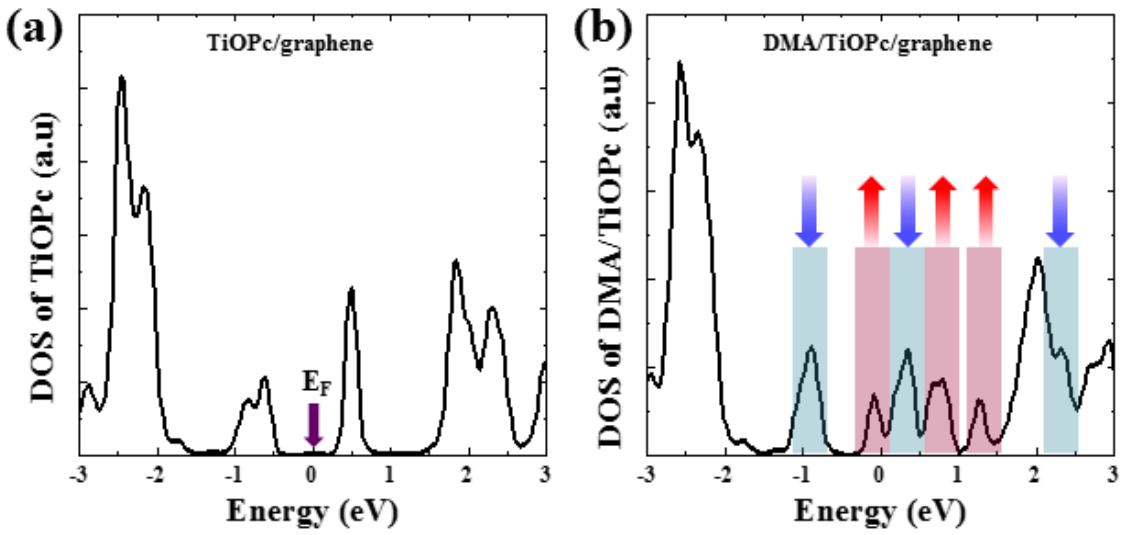

Figure 4.3. DFT projected density of states (PDOS) (a) PDOS of a TiOPc molecule on graphene. (b) A DMA/TiOPc molecule on graphene, respectively, assuming a single DMA molecule reacts only with the O of the TiOPc molecule.

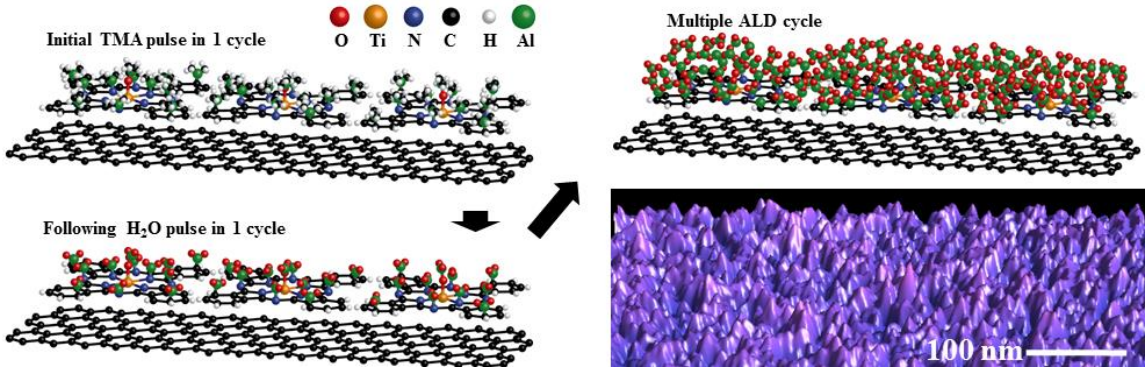

Figure 4.4. Proposed schematic diagram for growth of AlO_x on TiOPc/graphene. AFM images after five cycles of ALD pulse on TiOPc/single layer graphene/SiO_2/Si.

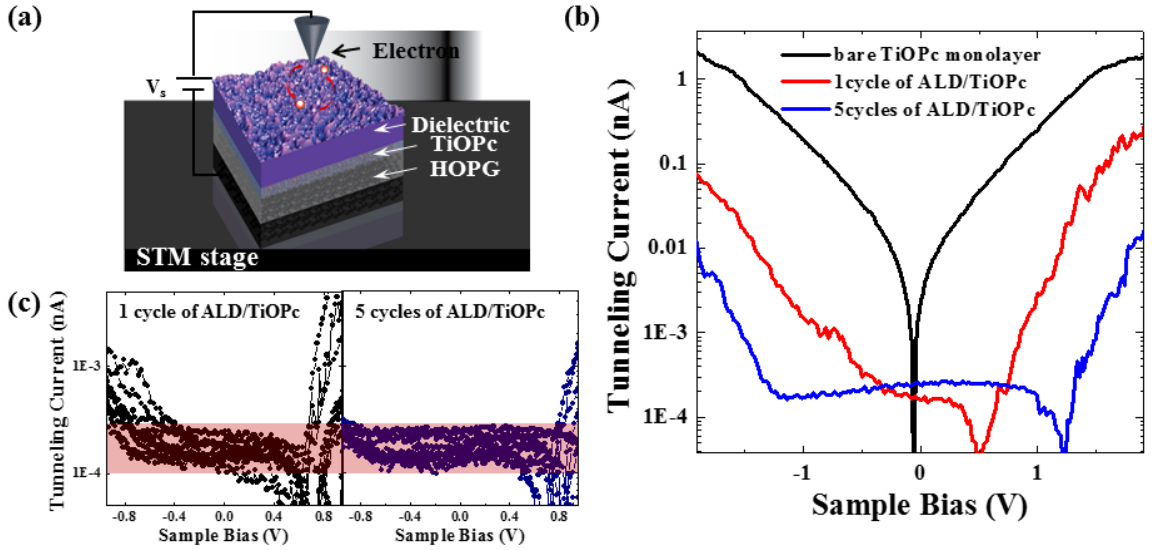

Figure 4.5. Scanning tunneling characterization of deposited dielectric layers. (a) Schematic of tunnel junction in metal tip/vacuum/AlO_x(purple)/TiOPc(sky blue)/HOPG(gray). (b) Log scaled tunneling current of a TiOPc monolayer, AlO_x deposited by one and five cycles of TMA/H_2O pulses on TiOPc/HOPG. (c) Nine different STS IV curves taken after one and five cycles of ALD/TiOPc/HOPG.

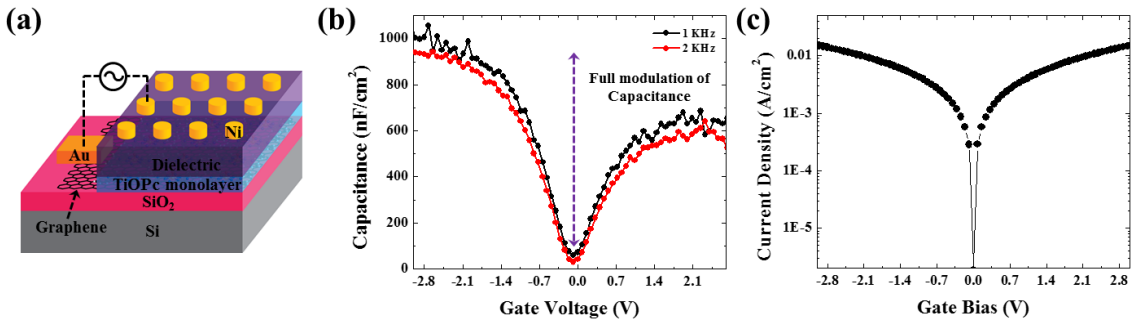

Figure 4.6. Capacitance characterization of deposited dielectric layer. (a) Schematic of metal−oxide−graphene capacitor with TiOPc seed monolayer. (b) Capacitance−voltage data for 50 ALD cycle dielectric layer on TiOPc/graphene/SiO_2/Si. (c) Leakage current density−voltage data of same capacitor; IV reported at 1 MHz.

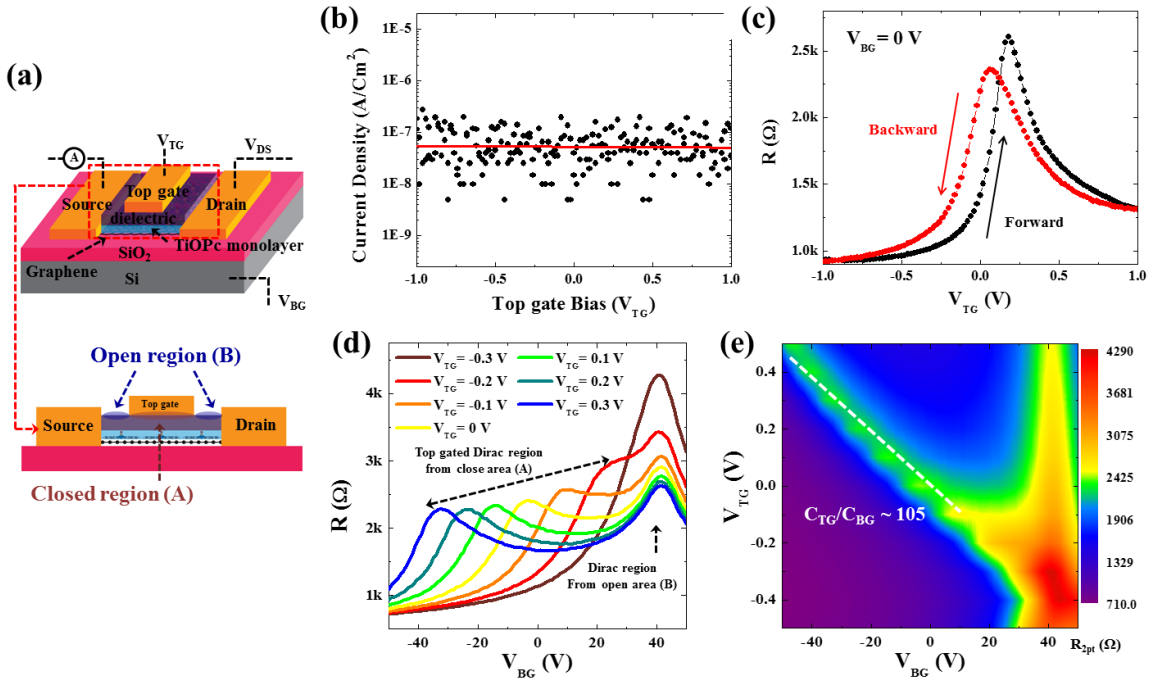

Figure 4.7. Electric characterization of deposited dielectric layer. (a) Schematic of dual gate 40 cycles dielectric-graphene FET. (b) Leakage current density-top gate bias of graphene FET. (c) Resistance versus top gate bias at 0 V back gate bias. The hysteresis between forward and backward sweeps is 0.12 V. (d) Resistance versus back gate bias at different top gate bias from −0.3 to 0.3 V. (e) Two-dimensional resistance plot as a function of top-gate voltage and back-gate voltage for a graphene FET.

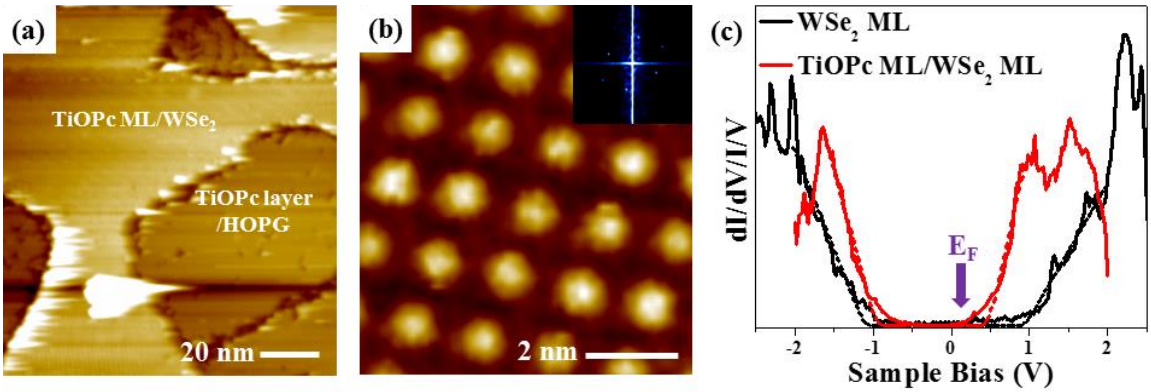

Figure 4.8. STM images of a monolayer TiOPc on WSe_2/HOPG. STM images recorded at 100 K. (a) TiOPc ML deposited on a WSe_2 ML on HOPG. (b) Submolecular resolution of MBE TiOPc ML/WSe_2 ML/HOPG. The central O is observed as a bright spot. (V_S = +2.0 V, I_T = 40 pA) The inset shows the Fourier transform of the TiOPc ML. (c) (dI/dV)/(I/V) spectrum of bare WSe_2ML/HOPG and TiOPc ML/WSe_2 ML/HOPG.

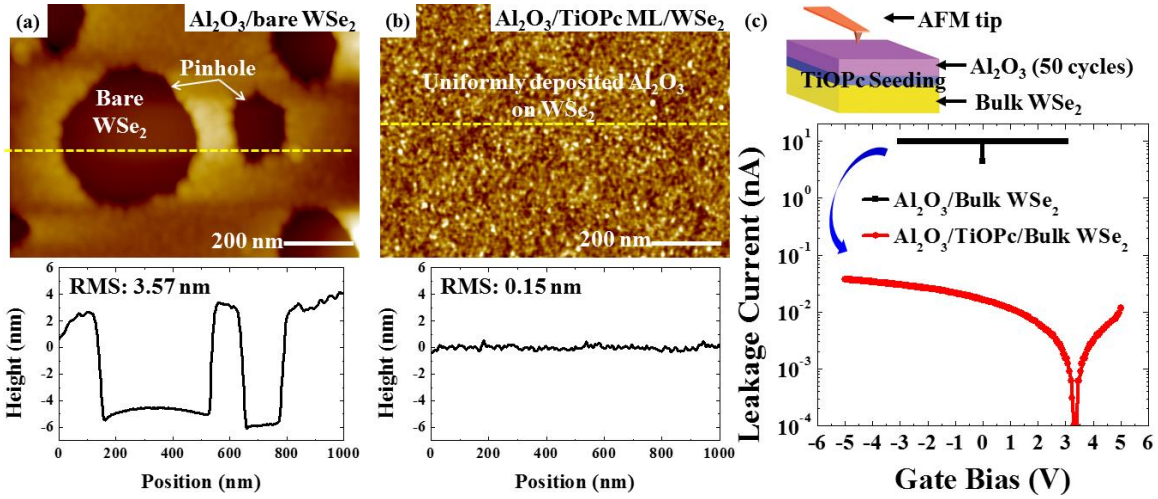

Figure 4.9. Topographic and electronic characteristics of Al_2O_3/TiOPc stack on bulk WSe_2 using AFM and C-AFM. (a) AFM image and corresponding line trace of Al_2O_3/bulk WSe_2 without the TiOPc layer. (b) AFM image and line trace of Al_2O_3/TiOPc/bulk WSe_2. (c) Conductive-AFM measurements of Al_2O_3 leakage currents prior to postdeposition annealing.

5. Reference

1. Wright, J. D., Gas-Adsorption on Phthalocyanines and Its Effects on Electrical-Properties. *Prog Surf Sci* **1989,** *31* (1-2), 1-60.

2. Archer, P. B. M.; Chadwick, A. V.; Miasik, J. J.; Tamizi, M.; Wright, J. D., Kinetic Factors in the Response of Organometallic Semiconductor Gas Sensors. *Sensor Actuator* **1989,** *16* (4), 379-392.

3. Ho, K. C.; Tsou, Y. H., Chemiresistor-type NO gas sensor based on nickel phthalocyanine thin films. *Sensor Actuat B-Chem* **2001,** *77* (1-2), 253-259.

4. van Faassen, E.; Kerp, H., Explanation of the low oxygen sensitivity of thin film phthalocyanine gas sensors. *Sensor Actuat B-Chem* **2003,** *88* (3), 329-333.

5. Bohrer, F. I.; Colesniuc, C. N.; Park, J.; Ruidiaz, M. E.; Schuller, I. K.; Kummel, A. C.; Trogler, W. C., Comparative Gas Sensing in Cobalt, Nickel, Copper, Zinc, and Metal-Free Phthalocyanine Chemiresistors. *J Am Chem Soc* **2009,** *131* (2), 478-485.

6. Grate, J. W.; Klusty, M.; Barger, W. R.; Snow, A. W., Role of Selective Sorption in Chemiresistor Sensors for Organophosphorus Detection. *Anal Chem* **1990,** *62* (18), 1927-1934.

7. Fu, Y. T.; da Silva, D. A.; Sini, G.; Asiri, A. M.; Aziz, S. G.; Risko, C.; Bredas, J. L., Structure and Disorder in Squaraine-C60 Organic Solar Cells: A Theoretical Description of Molecular Packing and Electronic Coupling at the Donor-Acceptor Interface. *Adv Funct Mater* **2014,** *24* (24), 3790-3798.

8. Nie, W. Y.; Tsai, H. H.; Asadpour, R.; Blancon, J. C.; Neukirch, A. J.; Gupta, G.; Crochet, J. J.; Chhowalla, M.; Tretiak, S.; Alam, M. A.; Wang, H. L.; Mohite, A. D., High-efficiency solution-processed perovskite solar cells with millimeter-scale grains. *Science* **2015,** *347* (6221), 522-525.

9. Ogawa, S.; Fan, F. R. F.; Bard, A. J., Scanning-Tunneling-Microscopy, Tunneling Spectroscopy, and Photoelectrochemistry of a Film of Q-Cds Particles Incorporated in a Self-Assembled Monolayer on a Gold Surface. *J Phys Chem-Us* **1995,** *99* (28), 11182-11189.

10. Placencia, D.; Wang, W. N.; Gantz, J.; Jenkins, J. L.; Armstrong, N. R., Highly Photoactive Titanyl Phthalocyanine Polymorphs as Textured Donor Layers in Organic Solar Cells. *J Phys Chem C* **2011,** *115* (38), 18873-18884.

11. Placencia, D.; Wang, W. N.; Shallcross, R. C.; Nebesny, K. W.; Brumbach, M.; Armstrong, N. R., Organic Photovoltaic Cells Based On Solvent-Annealed, Textured Titanyl Phthalocyanine/C-60 Heterojunctions. *Adv Funct Mater* **2009,** *19* (12), 1913-1921.

12. Shah, S.; Biswas, R., Atomic Pathways Underlying Light-Induced Changes in Organic Solar Cell Materials. *J Phys Chem C* **2015,** *119* (35), 20265-20271.

13. Su, M. S.; Kuo, C. Y.; Yuan, M. C.; Jeng, U. S.; Su, C. J.; Wei, K. H., Improving Device Efficiency of Polymer/Fullerene Bulk Heterojunction Solar Cells Through Enhanced Crystallinity and Reduced Grain Boundaries Induced by Solvent Additives. *Adv Mater* **2011,** *23* (29), 3315-+.

14. Tress, W.; Leo, K.; Riede, M., Dominating recombination mechanisms in organic solar cells based on ZnPc and C-60. *Appl Phys Lett* **2013,** *102* (16).

15. Williams, G.; Sutty, S.; Klenkler, R.; Aziz, H., Renewed interest in metal phthalocyanine donors for small molecule organic solar cells. *Solar Energy Materials and Solar Cells* **2014,** *124*, 217-226.

16. Lawton, E. A., The Thermal Stability of Copper Phthalocyanine. *J Phys Chem-Us* **1958,** *62* (3), 384-384.

17. Kanai, M.; Kawai, T.; Motai, K.; Wang, X. D.; Hashizume, T.; Sakura, T., Scanning-Tunneling-Microscopy Observation of Copper-Phthalocyanine Molecules on Si(100) and Si(111) Surfaces. *Surf Sci* **1995,** *329* (3), L619-L623.

18. Lu, X.; Hipps, K. W.; Wang, X. D.; Mazur, U., Scanning tunneling microscopy of metal phthalocyanines: d(7) and d(9) cases. *J Am Chem Soc* **1996,** *118* (30), 7197-7202.

19. Lu, X.; Hipps, K. W., Scanning tunneling microscopy of metal phthalocyanines: d(6) and d(8) cases. *J Phys Chem B* **1997,** *101* (27), 5391-5396.

20. Wang, Y. F.; Kroger, J.; Berndt, R.; Hofer, W., Structural and Electronic Properties of Ultrathin Tin-Phthalocyanine Films on Ag(111) at the Single-Molecule Level. *Angew Chem Int Edit* **2009,** *48* (7), 1261-1265.

21. Zhang, L. Z.; Cheng, Z. H.; Huan, Q.; He, X. B.; Lin, X.; Gao, L.; Deng, Z. T.; Jiang, N.; Liu, Q.; Du, S. X.; Guo, H. M.; Gao, H. J., Site- and Configuration-Selective Anchoring of Iron-Phthalocyanine on the Step Edges of Au(111) Surface. *J Phys Chem C* **2011,** *115* (21), 10791-10796.

22. Li, Z. Y.; Li, B.; Yang, J. L.; Hou, J. G., Single-Molecule Chemistry of Metal Phthalocyanine on Noble Metal Surfaces. *Accounts Chem Res* **2010,** *43* (7), 954-962.

23. Schmidt, A.; Chau, L. K.; Back, A.; Armstrong, N. R., Epitaxial phthalocyanine ultrathin films grown by organic molecular beam epitaxy (OMBE). *Phthalocyanines* **1996,** *4*, 307-341.

24. Novoselov, K. S.; Geim, A. K.; Morozov, S. V.; Jiang, D.; Zhang, Y.; Dubonos, S. V.; Grigorieva, I. V.; Firsov, A. A., Electric field effect in atomically thin carbon films. *Science* **2004,** *306* (5696), 666-669.

25. Podzorov, V.; Gershenson, M. E.; Kloc, C.; Zeis, R.; Bucher, E., High-mobility field-effect transistors based on transition metal dichalcogenides. *Appl Phys Lett* **2004,** *84* (17), 3301-3303.

26. Radisavljevic, B.; Radenovic, A.; Brivio, J.; Giacometti, V.; Kis, A., Single-layer MoS2 transistors. *Nat Nanotechnol* **2011,** *6* (3), 147-150.

27. Fang, H.; Chuang, S.; Chang, T. C.; Takei, K.; Takahashi, T.; Javey, A., High-Performance Single Layered WSe2 p-FETs with Chemically Doped Contacts. *Nano Lett* **2012,** *12* (7), 3788-3792.

28. Mak, K. F.; He, K. L.; Shan, J.; Heinz, T. F., Control of valley polarization in monolayer MoS2 by optical helicity. *Nat Nanotechnol* **2012,** *7* (8), 494-498.

29. Chen, Y. F.; Xi, J. Y.; Dumcenco, D. O.; Liu, Z.; Suenaga, K.; Wang, D.; Shuai, Z. G.; Huang, Y. S.; Xie, L. M., Tunable Band Gap Photoluminescence from Atomically Thin Transition-Metal Dichalcogenide Alloys. *Acs Nano* **2013,** *7* (5), 4610-4616.

30. Schwarz, S.; Dufferwiel, S.; Walker, P. M.; Withers, F.; Trichet, A. A. P.; Sich, M.; Li, F.; Chekhovich, E. A.; Borisenko, D. N.; Kolesnikov, N. N.; Novoselov, K. S.; Skolnick, M. S.; Smith, J. M.; Krizhanovskii, D. N.; Tartakovskii, A. I., Two-Dimensional Metal-Chalcogenide Films in Tunable Optical Microcavities. *Nano Lett* **2014,** *14* (12), 7003-7008.

31. Li, M.; Esseni, D.; Snider, G.; Jena, D.; Xing, H. G., Single particle transport in two-dimensional heterojunction interlayer tunneling field effect transistor. *J Appl Phys* **2014,** *115* (7).
32. Zeng, H. L.; Dai, J. F.; Yao, W.; Xiao, D.; Cui, X. D., Valley polarization in MoS2 monolayers by optical pumping. *Nat Nanotechnol* **2012,** *7* (8), 490-493.

33. Lee, C. H.; Lee, G. H.; van der Zande, A. M.; Chen, W. C.; Li, Y. L.; Han, M. Y.; Cui, X.; Arefe, G.; Nuckolls, C.; Heinz, T. F.; Guo, J.; Hone, J.; Kim, P., Atomically thin p-n junctions with van der Waals heterointerfaces. *Nat Nanotechnol* **2014,** *9* (9), 676-681.

34. Rivera, P.; Schaibley, J. R.; Jones, A. M.; Ross, J. S.; Wu, S. F.; Aivazian, G.; Klement, P.; Seyler, K.; Clark, G.; Ghimire, N. J.; Yan, J. Q.; Mandrus, D. G.; Yao, W.; Xu, X. D., Observation of long-lived interlayer excitons in monolayer MoSe2-WSe2 heterostructures. *Nat Commun* **2015,** *6*.

35. Yan, R. S.; Fathipour, S.; Han, Y. M.; Song, B.; Xiao, S. D.; Li, M. D.; Ma, N.; Protasenko, V.; Muller, D. A.; Jena, D.; Xing, H. G., Esaki Diodes in van der Waals Heterojunctions with Broken-Gap Energy Band Alignment. *Nano Lett* **2015,** *15* (9), 5791-5798.

36. Nitsche, R.; Bolsterli, H. U.; Lichtensteiger, M., Crystal Growth by Chemical Transport Reactions .1. Binary, Ternary, and Mixed-Crystal Chalcogenides. *J Phys Chem Solids* **1961,** *21* (3-4), 199-205.

37. Eichfeld, S. M.; Hossain, L.; Lin, Y. C.; Piasecki, A. F.; Kupp, B.; Birdwell, A. G.; Burke, R. A.; Lu, N.; Peng, X.; Li, J.; Azcatl, A.; McDonnell, S.; Wallace, R. M.; Kim, M. J.; Mayer, T. S.; Redwing, J. M.; Robinson, J. A., Highly Scalable, Atomically Thin WSe2 Grown via Metal-Organic Chemical Vapor Deposition. *Acs Nano* **2015,** *9* (2), 2080-2087.

38. Zhang, C. D.; Johnson, A.; Hsu, C. L.; Li, L. J.; Shih, C. K., Direct Imaging of Band Profile in Single Layer MoS2 on Graphite: Quasiparticle Energy Gap, Metallic Edge States, and Edge Band Bending. *Nano Lett* **2014,** *14* (5), 2443-2447.

39. Li, X. S.; Cai, W. W.; An, J. H.; Kim, S.; Nah, J.; Yang, D. X.; Piner, R.; Velamakanni, A.; Jung, I.; Tutuc, E.; Banerjee, S. K.; Colombo, L.; Ruoff, R. S., Large-Area Synthesis of High-Quality and Uniform Graphene Films on Copper Foils. *Science* **2009,** *324* (5932), 1312-1314.

40. Suk, J. W.; Kitt, A.; Magnuson, C. W.; Hao, Y. F.; Ahmed, S.; An, J. H.; Swan, A. K.; Goldberg, B. B.; Ruoff, R. S., Transfer of CVD-Grown Monolayer Graphene onto Arbitrary Substrates. *Acs Nano* **2011,** *5* (9), 6916-6924.

41. Wang, W.; Leung, K. K.; Fong, W. K.; Wang, S. F.; Hui, Y. Y.; Lau, S. P.; Chen, Z.; Shi, L. J.; Cao, C. B.; Surya, C., Molecular beam epitaxy growth of high quality p-doped SnS van der Waals epitaxy on a graphene buffer layer. *J Appl Phys* **2012,** *111* (9).

42. Ugeda, M. M.; Bradley, A. J.; Shi, S. F.; da Jornada, F. H.; Zhang, Y.; Qiu, D. Y.; Ruan, W.; Mo, S. K.; Hussain, Z.; Shen, Z. X.; Wang, F.; Louie, S. G.; Crommie, M. F., Giant bandgap renormalization and excitonic effects in a monolayer transition metal dichalcogenide semiconductor. *Nat Mater* **2014,** *13* (12), 1091-1095.

43. Yue, R. Y.; Barton, A. T.; Zhu, H.; Azcatl, A.; Pena, L. F.; Wang, J.; Peng, X.; Lu, N.; Cheng, L. X.; Addou, R.; McDonnell, S.; Colombo, L.; Hsu, J. W. P.; Kim, J.; Kim, M. J.; Wallace, R. M.; Hinkle, C. L., HfSe2 Thin Films: 2D Transition Metal Dichalcogenides Grown by Molecular Beam Epitaxy. *Acs Nano* **2015,** *9* (1), 474-480.

44. Suresh Vishwanath, X. L., Sergei Rouvimov, Patrick C Mende, Angelica Azcatl, Stephen McDonnell, Robert M Wallace, Randall M Feenstra, Jacek K Furdyna, Debdeep Jena and Huili Grace Xing, Comprehensive structural and optical characterization of MBE grown MoSe2 on graphite, CaF2 and graphene. *2D Materials* **2015,** *2* (2), 024007.

45. Liu, H. J.; Jiao, L.; Xie, L.; Yang, F.; Chen, J. L.; Ho, W. K.; Gao, C. L.; Jia, J. F.; Cui, X. D.; Xie, M. H., Molecular-beam epitaxy of monolayer and bilayer WSe 2 : a scanning tunneling microscopy/spectroscopy study and deduction of exciton binding energy. *2D Materials* **2015,** *2* (3), 034004.

46. Binning, G.; Rohrer, H.; Gerber, C.; Weibel, E., Surface Studies by Scanning Tunneling Microscopy. *Phys Rev Lett* **1982,** *49* (1), 57-61.

47. Eley, D. D.; Hazeldin.Dj; Palmer, T. F., Mass-Spectra, Ionization-Potentials and Related Properties of Metal-Free and Transition-Metal Phthalocyanines. *J Chem Soc Farad T 2* **1973,** *69* (12), 1808-1814.

48. Tegeler, E.; Iwan, M.; Koch, E. E., Electronic-Structure of the Valence Bands of H-2-Phthalocyanine, Mg-Phthalocyanine and Pt-Phthalocyanine Derived from Soft-X-Ray Emission and Photoelectron Emission-Spectra. *J Electron Spectrosc* **1981,** *22* (3-4), 297-307.

49. Martin, M.; Andre, J. J.; Simon, J., Influence of Dioxygen on the Junction Properties of Metallophthalocyanine Based Devices. *J Appl Phys* **1983,** *54* (5), 2792-2794.

50. Kerp, H. R.; Westerduin, K. T.; van Veen, A. T.; van Faassen, E. E., Quantification and effects of molecular oxygen and water in zinc phthalocyanine layers. *J Mater Res* **2001,** *16* (2), 503-511.

51. Simon, J.; André, J. J.; Lehn, J. M.; Rees, C. W., *Molecular semiconductors : photoelectrical properties and solar cells*. Springer-Verlag: Berlin ; New York, 1985; p xiii, 288 p.

52. Zwart, J.; Vanwolput, J. H. M. C., Esr Study of Reaction of Cobalt Phthalocyanines with Ammonia and Dioxygen. *J Mol Catal* **1979,** *5* (1), 51-64.

53. Lever, A. B. P.; Wilshire, J. P.; Quan, S. K., Manganese Phthalocyanine-Dioxygen Molecular Adduct. *J Am Chem Soc* **1979,** *101* (13), 3668-3669.

54. Yahiro, H.; Naka, T.; Kuramoto, T.; Kurohagi, K.; Okada, G.; Shiotani, M., An EPR study on oxygen molecule adduct of Co(II)-phthalocyanines encapsulated into zeolites. *Micropor Mesopor Mat* **2005,** *79* (1-3), 291-297.

55. Honeybourne, C. L.; Ewen, R. J.; Hill, C. A. S., Use of Thin-Films of Conjugated Organic Macrocycles as the Active Elements in Toxic-Gas Sensors Operating at Room-Temperature. *J Chem Soc Farad T 1* **1984,** *80*, 851-863.

56. Bouvet, M.; Guillaud, G.; Leroy, A.; Maillard, A.; Spirkovitch, S.; Tournilhac, F. G., Phthalocyanine-based field-effect transistor as ozone sensor. *Sensor Actuat B-Chem* **2001,** *73* (1), 63-70.

57. Bohrer, F. I.; Sharoni, A.; Colesniuc, C.; Park, J.; Schuller, I. K.; Kummel, A. C.; Trogler, W. C., Gas sensing mechanism in chemiresistive cobalt and metal-free phthalocyanine thin films. *J Am Chem Soc* **2007,** *129* (17), 5640-5646.

58. Tran, N. L.; Bohrer, F. I.; Trogler, W. C.; Kummel, A. C., A density functional theory study of the correlation between analyte basicity, ZnPc adsorption strength, and sensor response. *J Chem Phys* **2009,** *130* (20).

59. Royer, J. E.; Kappe, E. D.; Zhang, C. Y.; Martin, D. T.; Trogler, W. C.; Kummel, A. C., Organic Thin-Film Transistors for Selective Hydrogen Peroxide and Organic Peroxide Vapor Detection. *J Phys Chem C* **2012,** *116* (46), 24566-24572.

60. Choi, C. G.; Lee, S.; Lee, W. J., NO gas-sensing characteristics of copper phthalocyanine film prepared by plasma-activated evaporation. *Sensor Actuat B-Chem* **1996,** *32* (1), 77-82.

61. Bishop, S. R.; Tran, N. L.; Poon, G. C.; Kummel, A. C., Dynamics of analyte binding onto a metallophthalocyanine: NO/FePc. *J Chem Phys* **2007,** *127* (21).

62. Newton, M. I.; Starke, T. K. H.; Willis, M. R.; McHale, G., NO2 detection at room temperature with copper phthalocyanine thin film devices. *Sensor Actuat B-Chem* **2000,** *67* (3), 307-311.

63. Newton, M. I.; Starke, T. K. H.; McHale, G.; Willis, M. R., The effect of NO2 doping on the gas sensing properties of copper phthalocyanine thin film devices. *Thin Solid Films* **2000,** *360* (1-2), 10-12.

64. Padma, N.; Joshi, A.; Singh, A.; Deshpande, S. K.; Aswal, D. K.; Gupta, S. K.; Yakhmi, J. V., NO(2) sensors with room temperature operation and long term stability using copper phthalocyanine thin films. *Sensor Actuat B-Chem* **2009,** *143* (1), 246-252.

65. Alagna, L.; Capobianchi, A.; Paoletti, A. M.; Pennesi, G.; Rossi, G.; Casaletto, M. P.; Generosi, A.; Paci, B.; Albertini, V. R., The effect of NO2 on spectroscopic and structural properties of evaporated ruthenium phthalocyanine dimer. *Thin Solid Films* **2006,** *515* (4), 2748-2753.

66. Park, J.; Royer, J. E.; Colesniuc, C. N.; Bohrer, F. I.; Sharoni, A.; Jin, S. H.; Schuller, I. K.; Trogler, W. C.; Kummel, A. C., Ambient induced degradation and chemically activated recovery in copper phthalocyanine thin film transistors. *J Appl Phys* **2009,** *106* (3).

67. Buchholz, J. C.; Somorjai, G. A., Surface-Structures of Phthalocyanine Monolayers and Vapor-Grown Films - Low-Energy Electron-Diffraction Study. *J Chem Phys* **1977,** *66* (2), 573-580.

68. Kresse, G.; Furthmuller, J., Efficiency of ab-initio total energy calculations for metals and semiconductors using a plane-wave basis set. *Comp Mater Sci* **1996,** *6* (1), 15-50.

69. Kresse, G.; Furthmuller, J., Efficient iterative schemes for ab initio total-energy calculations using a plane-wave basis set. *Phys Rev B* **1996,** *54* (16), 11169-11186.

70. Blochl, P. E., Projector Augmented-Wave Method. *Phys Rev B* **1994,** *50* (24), 17953-17979.
71. Kresse, G.; Joubert, D., From ultrasoft pseudopotentials to the projector augmented-wave method. *Phys Rev B* **1999,** *59* (3), 1758-1775.

72. Perdew, J. P.; Burke, K.; Ernzerhof, M., Generalized gradient approximation made simple. *Phys Rev Lett* **1996,** *77* (18), 3865-3868.

73. Perdew, J. P.; Burke, K.; Ernzerhof, M., Generalized gradient approximation made simple (vol 77, pg 3865, 1996). *Phys Rev Lett* **1997,** *78* (7), 1396-1396.

74. Henkelman, G.; Arnaldsson, A.; Jonsson, H., A fast and robust algorithm for Bader decomposition of charge density. *Comp Mater Sci* **2006,** *36* (3), 354-360.

75. Sanville, E.; Kenny, S. D.; Smith, R.; Henkelman, G., Improved grid-based algorithm for Bader charge allocation. *J Comput Chem* **2007,** *28* (5), 899-908.

76. Tang, W.; Sanville, E.; Henkelman, G., A grid-based Bader analysis algorithm without lattice bias. *J Phys-Condens Mat* **2009,** *21* (8).

77. Nguyen, T. Q.; Escano, M. C. S.; Kasai, H., Nitric Oxide Adsorption Effects on Metal Phthalocyanines. *J Phys Chem B* **2010,** *114* (31), 10017-10021.

78. Tran, N. L.; Kummel, A. C., A density functional theory study on the binding of NO onto FePc films. *J Chem Phys* **2007,** *127* (21).

79. Wang, G. F.; Ramesh, N.; Hsu, A.; Chu, D.; Chen, R. R., Density functional theory study of the adsorption of oxygen molecule on iron phthalocyanine and cobalt phthalocyanine. *Mol Simulat* **2008,** *34* (10-15), 1051-1056.

80. Buchner, F.; Seufert, K.; Auwarter, W.; Heim, D.; Barth, J. V.; Flechtner, K.; Gottfried, J. M.; Steinruck, H. P.; Marbach, H., NO-Induced Reorganization of Porphyrin Arrays. *Acs Nano* **2009,** *3* (7), 1789-1794.

81. Bartram, M. E.; Koel, B. E., The Molecular Adsorption of No2 and the Formation of N2o3 on Au(111). *Surf Sci* **1989,** *213* (1), 137-156.

82. Wickham, D. T.; Banse, B. A.; Koel, B. E., Adsorption of Nitrogen-Dioxide on Polycrystalline Gold. *Catal Lett* **1990,** *6* (2), 163-172.

83. Honeybourne, C. L.; Ewen, R. J., Dark Dc Conductivity and Spectroscopy of Clean and Gas Doped Thin-Films of Organic Semiconductors. *Journal of Physics and Chemistry of Solids* **1983,** *44* (3), 215-223.

84. Zheng, G.; Altman, E. I., The oxidation of Pd(111). *Surf Sci* **2000,** *462* (1-3), 151-168.

85. Chen, H. L.; Wu, S. Y.; Chen, H. T.; Chang, J. G.; Ju, S. P.; Tsai, C.; Hsu, L. C., Theoretical Study on Adsorption and Dissociation of NO(2) Molecule on Fe(111) Surface. *Langmuir* **2010,** *26* (10), 7157-7164.

86. Yen, M. Y.; Ho, J. J., Density-functional study for the NO(x) (x=1, 2) dissociation mechanism on the Cu(111) surface. *Chem Phys* **2010,** *373* (3), 300-306.

87. Lozzi, L.; Picozzi, S.; Santucci, S.; Cantalini, C.; Delley, B., Photoemission and theoretical investigations on NO2 doping of copper phthalocyanine thin films. *J Electron Spectrosc* **2004,** *137*, 101-105.

88. Mrwa, A.; Friedrich, M.; Hofmann, A.; Zahn, D. R. T., Response of Lead Phthalocyanine to High No2 Concentration. *Sensor Actuat B-Chem* **1995,** *25* (1-3), 596-599.

89. Sadaoka, Y.; Jones, T. A.; Revell, G. S.; Gopel, W., Effects of Morphology on No2 Detection in Air at Room-Temperature with Phthalocyanine Thin-Films. *J Mater Sci* **1990,** *25* (12), 5257-5268.

90. Saliba, N.; Parker, D. H.; Koel, B. E., Adsorption of oxygen on Au(111) by exposure to ozone. *Surf Sci* **1998,** *410* (2-3), 270-282.

91. Parker, D. H.; Koel, B. E., Chemisorption of High Coverages of Atomic Oxygen on the Pt(111), Pd(111), and Au(111) Surfaces. *J Vac Sci Technol A* **1990,** *8* (3), 2585-2590.

92. vanDaelen, M. A.; Li, Y. S.; Newsam, J. M.; vanSanten, R. A., Energetics and dynamics for NO and CO dissociation on Cu(100) and Cu(111). *J Phys Chem-Us* **1996,** *100* (6), 2279-2289.

93. Bogicevic, A.; Hass, K. C., NO pairing and transformation to N2O on Cu(111) and Pt(111) from first principles. *Surf Sci* **2002,** *506* (1-2), L237-L242.

94. Gurevich, A. B.; Bent, B. E.; Teplyakov, A. V.; Chen, J. G., A NEXAFS investigation of the formation and decomposition of CuO and Cu2O thin films on Cu(100). *Surf Sci* **1999,** *442* (1), L971-L976.

95. Yen, M. Y.; Ho, J. J., Density-functional study for the NOx (x=1, 2) dissociation mechanism on the Cu(111) surface. *Chem Phys* **2010,** *373* (3), 300-306.

96. Rodriguez, J. A.; Jirsak, T.; Liu, G.; Hrbek, J.; Dvorak, J.; Maiti, A., Chemistry of NO2 on oxide surfaces: Formation of NO3 on TiO2(110) and NO2 <-> O vacancy interactions. *J Am Chem Soc* **2001,** *123* (39), 9597-9605.

97. Kong, X. H.; Yang, Y. L.; Lei, S. B.; Wang, C., On the topography multiplicity of non-planar titanyl(IV) phthalocyanine molecules and the STM imaging mechanism. *Surf Sci* **2008,** *602* (3), 684-692.

98. Batteas, J. D.; Dunphy, J. C.; Somorjai, G. A.; Salmeron, M., Coadsorbate induced reconstruction of a stepped Pt(111) surface by sulfur and CO: A novel surface restructuring mechanism observed by scanning tunneling microscopy. *Phys Rev Lett* **1996,** *77* (3), 534-537.

99. Anderson, P. W., Absence of Diffusion in Certain Random Lattices. *Phys Rev* **1958,** *109* (5), 1492-1505.

100. Horowitz, G.; Hajlaoui, M. E., Mobility in polycrystalline oligothiophene field-effect transistors dependent on grain size. *Adv Mater* **2000,** *12* (14), 1046-1050.

101. Chwang, A. B.; Frisbie, C. D., Temperature and gate voltage dependent transport across a single organic semiconductor grain boundary. *J Appl Phys* **2001,** *90* (3), 1342-1349.

102. Verlaak, S.; Arkhipov, V.; Heremans, P., Modeling of transport in polycrystalline organic semiconductor films. *Appl Phys Lett* **2003,** *82* (5), 745-747.

103. Puntambekar, K.; Dong, J. P.; Haugstad, G.; Frisbie, C. D., Structural and electrostatic complexity at a pentacene/insulator interface. *Adv Funct Mater* **2006,** *16* (7), 879-884.

104. Huang, H. C.; Wang, H. B.; Zhang, J. D.; Yan, D. H., Surface potential images of polycrystalline organic semiconductors obtained by Kelvin probe force microscopy. *Appl Phys a-Mater* **2009,** *95* (1), 125-130.

105. Kaake, L. G.; Barbara, P. F.; Zhu, X. Y., Intrinsic Charge Trapping in Organic and Polymeric Semiconductors: A Physical Chemistry Perspective. *J Phys Chem Lett* **2010,** *1* (3), 628-635.

106. Wang, X. J.; Ji, S. L.; Wang, H. B.; Yan, D. H., Highly sensitive gas sensor enhanced by tuning the surface potential. *Org Electron* **2011,** *12* (12), 2230-2235.

107. Di Carlo, A.; Piacenza, F.; Bolognesi, A.; Stadlober, B.; Maresch, H., Influence of grain sizes on the mobility of organic thin-film transistors. *Appl Phys Lett* **2005,** *86* (26).

108. Jin, S. H.; Jung, K. D.; Shin, H.; Park, B. G.; Lee, J. D., Grain size effects on contact resistance of top-contact pentacene TFTs. *Synthetic Met* **2006,** *156* (2-4), 196-201.

109. Wang, S. D.; Miyadera, T.; Minari, T.; Aoyagi, Y.; Tsukagoshi, K., Correlation between grain size and device parameters in pentacene thin film transistors. *Appl Phys Lett* **2008,** *93* (4).

110. Vinciguerra, V.; La Rosa, M.; Nicolosi, D.; Sicurella, G.; Occhipinti, L., Modeling the gate bias dependence of contact resistance in staggered polycrystalline organic thin film transistors. *Org Electron* **2009,** *10* (6), 1074-1081.

111. Chae, S. H.; Jin, Y.; Kim, T. S.; Chung, D. S.; Na, H.; Nam, H.; Kim, H.; Perello, D. J.; Jeong, H. Y.; Ly, T. H.; Lee, Y. H., Oxidation Effect in Octahedral Hafnium Disulfide Thin Film. *Acs Nano* **2016,** *10* (1), 1309-1316.

112. Kosmider, K.; Gonzalez, J. W.; Fernandez-Rossier, J., Large spin splitting in the conduction band of transition metal dichalcogenide monolayers. *Phys Rev B* **2013,** *88* (24).

113. Jones, A. M.; Yu, H. Y.; Ghimire, N. J.; Wu, S. F.; Aivazian, G.; Ross, J. S.; Zhao, B.; Yan, J. Q.; Mandrus, D. G.; Xiao, D.; Yao, W.; Xu, X. D., Optical generation of excitonic valley coherence in monolayer WSe2. *Nat Nanotechnol* **2013,** *8* (9), 634-638.

114. Zhao, W. J.; Ribeiro, R. M.; Toh, M. L.; Carvalho, A.; Kloc, C.; Neto, A. H. C.; Eda, G., Origin of Indirect Optical Transitions in Few-Layer MoS2, WS2, and WSe2. *Nano Lett* **2013,** *13* (11), 5627-5634.

115. Fang, H.; Tosun, M.; Seol, G.; Chang, T. C.; Takei, K.; Guo, J.; Javey, A., Degenerate n-Doping of Few-Layer Transition Metal Dichalcogenides by Potassium. *Nano Lett* **2013,** *13* (5), 1991-1995.

116. Zhang, C.; Chen, Y.; Johnson, A.; Li, M.-Y.; Li, L.-J.; Mende, P. C.; Feenstra, R. M.; Shih, C.-K., Probing Critical Point Energies of Transition Metal Dichalcogenides: Surprising Indirect Gap of Single Layer WSe2. *Nano Lett* **2015,** *15* (10), 6494-6500.

117. Xue, J. M.; Sanchez-Yamagishi, J.; Bulmash, D.; Jacquod, P.; Deshpande, A.; Watanabe, K.; Taniguchi, T.; Jarillo-Herrero, P.; Leroy, B. J., Scanning tunnelling microscopy and spectroscopy of ultra-flat graphene on hexagonal boron nitride. *Nat Mater* **2011,** *10* (4), 282-285.

118. Geim, A. K.; Grigorieva, I. V., Van der Waals heterostructures. *Nature* **2013,** *499* (7459), 419-425.

119. Brixner, L. H., Preparation and Properties of the Single Crystalline Ab2-Type Selenides and Tellurides of Niobium, Tantalum, Molybdenum and Tungsten. *J Inorg Nucl Chem* **1962,** *24* (Mar), 257-263.

120. Ramasubramaniam, A., Large excitonic effects in monolayers of molybdenum and tungsten dichalcogenides. *Phys Rev B* **2012,** *86* (11).

121. Desai, S. B.; Seol, G.; Kang, J. S.; Fang, H.; Battaglia, C.; Kapadia, R.; Ager, J. W.; Guo, J.; Javey, A., Strain-Induced Indirect to Direct Bandgap Transition in Multi layer WSe2. *Nano Lett* **2014,** *14* (8), 4592-4597.

122. Feenstra, R. M.; Lee, J. Y.; Kang, M. H.; Meyer, G.; Rieder, K. H., Band gap of the Ge(111)c(2x8) surface by scanning tunneling spectroscopy. *Phys Rev B* **2006,** *73* (3).

123. Feenstra, R. M., Tunneling Spectroscopy of the (110)-Surface of Direct-Gap Iii-V Semiconductors. *Phys Rev B* **1994,** *50* (7), 4561-4570.

124. Bevington, P. R.; Robinson, D. K., *Data reduction and error analysis for the physical sciences*. 3rd ed.; McGraw-Hill: Boston, 2003; p xi, 320 p.

125. Yun, W. S.; Han, S. W.; Hong, S. C.; Kim, I. G.; Lee, J. D., Thickness and strain effects on electronic structures of transition metal dichalcogenides: 2H-M X-2 semiconductors (M = Mo, W; X = S, Se, Te). *Phys Rev B* **2012,** *85* (3).

126. Matsui, T.; Kambara, H.; Niimi, Y.; Tagami, K.; Tsukada, M.; Fukuyama, H., STS observations of landau levels at graphite surfaces. *Phys Rev Lett* **2005,** *94* (22).

127. Li, G. H.; Luican, A.; Andrei, E. Y., Scanning Tunneling Spectroscopy of Graphene on Graphite. *Phys Rev Lett* **2009,** *102* (17).

128. Wang, F. G.; Di Valentin, C.; Pacchioni, G., Electronic and Structural Properties of WO3: A Systematic Hybrid DFT Study. *J Phys Chem C* **2011,** *115* (16), 8345-8353.

129. Ping, Y.; Rocca, D.; Galli, G., Optical properties of tungsten trioxide from first-principles calculations. *Phys Rev B* **2013,** *87* (16).

130. Watanabe, H.; Fujikata, K.; Oaki, Y.; Imai, H., Band-gap expansion of tungsten oxide quantum dots synthesized in sub-nano porous silica. *Chem Commun* **2013,** *49* (76), 8477-8479.

131. Schofield, S. R.; Studer, P.; Hirjibehedin, C. F.; Curson, N. J.; Aeppli, G.; Bowler, D. R., Quantum engineering at the silicon surface using dangling bonds. *Nat Commun* **2013,** *4*.

132. Pierucci, D.; Naitabdi, A.; Bournel, F.; Gallet, J. J.; Tissot, H.; Carniato, S.; Rochet, F.; Kohler, U.; Laumann, D.; Kubsky, S.; Silly, M. G.; Sirotti, F., Benzaldehyde on Water-Saturated Si(001): Reaction with Isolated Silicon Dangling Bonds versus Concerted Hydrosilylation. *J Phys Chem C* **2014,** *118* (19), 10005-10016.

133. Helveg, S.; Lauritsen, J. V.; Laegsgaard, E.; Stensgaard, I.; Norskov, J. K.; Clausen, B. S.; Topsoe, H.; Besenbacher, F., Atomic-scale structure of single-layer MoS2 nanoclusters. *Phys Rev Lett* **2000,** *84* (5), 951-954.

134. Lauritsen, J. V.; Kibsgaard, J.; Helveg, S.; Topsoe, H.; Clausen, B. S.; Laegsgaard, E.; Besenbacher, F., Size-dependent structure of MoS2 nanocrystals. *Nat Nanotechnol* **2007,** *2* (1), 53-58.

135. Tuxen, A.; Kibsgaard, J.; Gobel, H.; Laegsgaard, E.; Topsoe, H.; Lauritsen, J. V.; Besenbacher, F., Size Threshold in the Dibenzothiophene Adsorption on MoS2 Nanoclusters. *Acs Nano* **2010,** *4* (8), 4677-4682.

136. Tsai, C.; Abild-Pedersen, F.; Norskov, J. K., Tuning the MoS2 Edge-Site Activity for Hydrogen Evolution via Support Interactions. *Nano Lett* **2014,** *14* (3), 1381-1387.

137. Bruix, A.; Füchtbauer, H. G.; Tuxen, A. K.; Walton, A. S.; Andersen, M.; Porsgaard, S.; Besenbacher, F.; Hammer, B.; Lauritsen, J. V., In Situ Detection of Active Edge Sites in Single-Layer MoS2 Catalysts. *Acs Nano* **2015,** *9* (9), 9322-9330.

138. Waitkins, G. R.; Clark, C. W., Selenium Dioxide - Preparation, Properties, and Use as Oxidizing Agent. *Chem Rev* **1945,** *36* (3), 235-289.

139. Brooks, L. S., The Vapor Pressures of Tellurium and Selenium. *J Am Chem Soc* **1952,** *74* (1), 227-229.

140. Geim, A. K.; Novoselov, K. S., The rise of graphene. *Nat Mater* **2007,** *6* (3), 183-191.

141. Meric, I.; Han, M. Y.; Young, A. F.; Ozyilmaz, B.; Kim, P.; Shepard, K. L., Current saturation in zero-bandgap, topgated graphene field-effect transistors. *Nat Nanotechnol* **2008,** *3* (11), 654-659.

142. Williams, J. R.; DiCarlo, L.; Marcus, C. M., Quantum hall effect in a gate-controlled p-n junction of graphene. *Science* **2007,** *317* (5838), 638-641.

143. Seabaugh, A. C.; Zhang, Q., Low-Voltage Tunnel Transistors for Beyond CMOS Logic. *P Ieee* **2010,** *98* (12), 2095-2110.

144. Banerjee, S. K.; Register, L. F.; Tutuc, E.; Reddy, D.; MacDonald, A. H., Bilayer PseudoSpin Field-Effect Transistor (BiSFET): A Proposed New Logic Device. *Ieee Electr Device L* **2009,** *30* (2), 158-160.

145. Reddy, D.; Register, L. F.; Tutuc, E.; Banerjee, S. K., Bilayer Pseudospin Field-Effect Transistor: Applications to Boolean Logic. *Ieee T Electron Dev* **2010,** *57* (4), 755-764.

146. Britnell, L.; Gorbachev, R. V.; Jalil, R.; Belle, B. D.; Schedin, F.; Katsnelson, M. I.; Eaves, L.; Morozov, S. V.; Mayorov, A. S.; Peres, N. M. R.; Neto, A. H. C.; Leist, J.; Geim, A. K.; Ponomarenko, L. A.; Novoselov, K. S., Electron Tunneling through Ultrathin Boron Nitride Crystalline Barriers. *Nano Lett* **2012,** *12* (3), 1707-1710.

147. Britnell, L.; Gorbachev, R. V.; Jalil, R.; Belle, B. D.; Schedin, F.; Mishchenko, A.; Georgiou, T.; Katsnelson, M. I.; Eaves, L.; Morozov, S. V.; Peres, N. M. R.; Leist, J.; Geim, A. K.; Novoselov, K. S.; Ponomarenko, L. A., Field-Effect Tunneling Transistor Based on Vertical Graphene Heterostructures. *Science* **2012,** *335* (6071), 947-950.

148. Feenstra, R. M.; Jena, D.; Gu, G., Single-particle tunneling in doped graphene-insulator-graphene junctions. *J Appl Phys* **2012,** *111* (4).

149. Britnell, L.; Gorbachev, R. V.; Geim, A. K.; Ponomarenko, L. A.; Mishchenko, A.; Greenaway, M. T.; Fromhold, T. M.; Novoselov, K. S.; Eaves, L., Resonant tunnelling and negative differential conductance in graphene transistors. *Nat Commun* **2013,** *4*.

150. Roy, T.; Hesabi, Z. R.; Joiner, C. A.; Fujimoto, A.; Vogel, E. M., Barrier engineering for double layer CVD graphene tunnel FETs. *Microelectron Eng* **2013,** *109*, 117-119.

151. Zhao, P.; Feenstra, R. M.; Gu, G.; Jena, D., SymFET: A Proposed Symmetric Graphene Tunneling Field-Effect Transistor. *Ieee T Electron Dev* **2013,** *60* (3), 951-957.

152. Roy, T.; Liu, L.; de la Barrera, S.; Chakrabarti, B.; Hesabi, Z. R.; Joiner, C. A.; Feenstra, R. M.; Gu, G.; Vogel, E. M., Tunneling characteristics in chemical vapor deposited graphene-hexagonal boron nitride-graphene junctions. *Appl Phys Lett* **2014,** *104* (12).

153. Fogler, M. M.; Butov, L. V.; Novoselov, K. S., High-temperature superfluidity with indirect excitons in van der Waals heterostructures. *Nat Commun* **2014,** *5*.

154. Gilbert, M. J., Performance Characteristics of Scaled Bilayer Graphene Pseudospin Devices. *Ieee T Electron Dev* **2010,** *57* (11), 3059-3067.

155. Mishchenko, A.; Tu, J. S.; Cao, Y.; Gorbachev, R. V.; Wallbank, J. R.; Greenaway, M. T.; Morozov, V. E.; Morozov, S. V.; Zhu, M. J.; Wong, S. L.; Withers, F.; Woods, C. R.; Kim, Y. J.; Watanabe, K.; Taniguchi, T.; Vdovin, E. E.; Makarovsky, O.; Fromhold, T. M.; Fal'ko, V. I.; Geim, A. K.; Eaves, L.; Novoselov, K. S., Twist-controlled resonant tunnelling in graphene/boron nitride/graphene heterostructures. *Nat Nanotechnol* **2014,** *9* (10), 808-813.

156. Khorasani, S. A., Tunable Spontaneous Emission From Layered Graphene/Dielectric Tunnel Junctions. *Ieee J Quantum Elect* **2014,** *50* (5), 307-313.

157. Fallahazad, B.; Lee, K.; Kang, S.; Xue, J. M.; Larentis, S.; Corbet, C.; Kim, K.; Movva, H. C. P.; Taniguchi, T.; Watanabe, K.; Register, L. F.; Banerjee, S. K.; Tutuc, E., Gate-Tunable Resonant Tunneling in Double Bilayer Graphene Heterostructures. *Nano Lett* **2015,** *15* (1), 428-433.

158. Kim, S.; Jo, I.; Nah, J.; Yao, Z.; Banerjee, S. K.; Tutuc, E., Coulomb drag of massless fermions in graphene. *Phys Rev B* **2011,** *83* (16).

159. Kim, S.; Jo, I.; Dillen, D. C.; Ferrer, D. A.; Fallahazad, B.; Yao, Z.; Banerjee, S. K.; Tutuc, E., Direct Measurement of the Fermi Energy in Graphene Using a Double-Layer Heterostructure. *Phys Rev Lett* **2012,** *108* (11).

160. Xuan, Y.; Wu, Y. Q.; Shen, T.; Qi, M.; Capano, M. A.; Cooper, J. A.; Ye, P. D., Atomic-layer-deposited nanostructures for graphene-based nanoelectronics. *Appl Phys Lett* **2008,** *92* (1).

161. Liao, L.; Duan, X. F., Graphene-dielectric integration for graphene transistors. *Mat Sci Eng R* **2010,** *70* (3-6), 354-370.

162. Alaboson, J. M. P.; Wang, Q. H.; Emery, J. D.; Lipson, A. L.; Bedzyk, M. J.; Elam, J. W.; Pellin, M. J.; Hersam, M. C., Seeding Atomic Layer Deposition of High-k Dielectrics on Epitaxial Graphene with Organic Self-Assembled Monolayers. *Acs Nano* **2011,** *5* (6), 5223-5232.

163. Jandhyala, S.; Mordi, G.; Lee, B.; Lee, G.; Floresca, C.; Cha, P. R.; Ahn, J.; Wallace, R. M.; Chabal, Y. J.; Kim, M. J.; Colombo, L.; Cho, K.; Kim, J., Atomic Layer Deposition of Dielectrics on Graphene Using Reversibly Physisorbed Ozone. *Acs Nano* **2012,** *6* (3), 2722-2730.

164. Sangwan, V. K.; Jariwala, D.; Filippone, S. A.; Karmel, H. J.; Johns, J. E.; Alaboson, J. M. P.; Marks, T. J.; Lauhon, L. J.; Hersam, M. C., Quantitatively Enhanced Reliability and Uniformity of High-kappa Dielectrics on Graphene Enabled by Self-Assembled Seeding Layers. *Nano Lett* **2013,** *13* (3), 1162-1167.

165. Shin, W. C.; Bong, J. H.; Choi, S. Y.; Cho, B. J., Functionalized Graphene as an Ultrathin Seed Layer for the Atomic Layer Deposition of Conformal High-k Dielectrics on Graphene. *Acs Appl Mater Inter* **2013,** *5* (22), 11515-11519.

166. Terrones, M.; Botello-Mendez, A. R.; Campos-Delgado, J.; Lopez-Urias, F.; Vega-Cantu, Y. I.; Rodriguez-Macias, F. J.; Elias, A. L.; Munoz-Sandoval, E.; Cano-Marquez, A. G.; Charlier, J. C.; Terrones, H., Graphene and graphite nanoribbons: Morphology, properties, synthesis, defects and applications. *Nano Today* **2010,** *5* (4), 351-372.

167. McDonnell, S.; Brennan, B.; Azcatl, A.; Lu, N.; Dong, H.; Buie, C.; Kim, J.; Hinkle, C. L.; Kim, M. J.; Wallace, R. M., HfO2 on MoS2 by Atomic Layer Deposition: Adsorption Mechanisms and Thickness Scalability. *Acs Nano* **2013,** *7* (11), 10354-10361.

168. Dlubak, B.; Seneor, P.; Anane, A.; Barraud, C.; Deranlot, C.; Deneuve, D.; Servet, B.; Mattana, R.; Petroff, F.; Fert, A., Are Al2O3 and MgO tunnel barriers suitable for spin injection in graphene? *Appl Phys Lett* **2010,** *97* (9).

169. Martin, M. B.; Dlubak, B.; Weatherup, R. S.; Yang, H.; Deranlot, C.; Bouzehouane, K.; Petroff, F.; Anane, A.; Hofmann, S.; Robertson, J.; Fert, A.; Seneor, P., Sub-nanometer Atomic Layer Deposition for Spintronics in Magnetic Tunnel Junctions Based on Graphene Spin-Filtering Membranes. *Acs Nano* **2014,** *8* (8), 7890-7895.

170. Liu, H.; Xu, K.; Zhang, X. J.; Ye, P. D., The integration of high-k dielectric on two-dimensional crystals by atomic layer deposition. *Appl Phys Lett* **2012,** *100* (15).

171. Norton, J. E.; Bredas, J. L., Theoretical characterization of titanyl phthalocyanine as a p-type organic semiconductor: Short intermolecular pi-pi interactions yield large electronic couplings and hole transport bandwidths. *J Chem Phys* **2008,** *128* (3).

172. Dillon, A. C.; Ott, A. W.; Way, J. D.; George, S. M., Surface-Chemistry of Al2o3 Deposition Using Al(Ch3)(3) and H2o in a Binary Reaction Sequence. *Surf Sci* **1995,** *322* (1-3), 230-242.

173. Potts, S. E.; Profijt, H. B.; Roelofs, R.; Kessels, W. M. M., Room-Temperature ALD of Metal Oxide Thin Films by Energy-Enhanced ALD. *Chem Vapor Depos* **2013,** *19* (4-6), 125-133.

174. Scherer, H.; Weimann, T.; Zorin, A. B.; Niemeyer, J., The effect of thermal annealing on the properties of Al-AlOx-Al single electron tunneling transistors. *J Appl Phys* **2001,** *90* (5), 2528-2532.

175. Hu, J.; Nainani, A.; Sun, Y.; Saraswat, K. C.; Wong, H. S. P., Impact of fixed charge on metal-insulator-semiconductor barrier height reduction. *Appl Phys Lett* **2011,** *99* (25).

176. Xia, J. L.; Chen, F.; Li, J. H.; Tao, N. J., Measurement of the quantum capacitance of graphene. *Nat Nanotechnol* **2009,** *4* (8), 505-509.

177. Xia, J. L.; Chen, F.; Tedesco, J. L.; Gaskill, D. K.; Myers-Ward, R. L.; Eddy, C. R.; Ferry, D. K.; Tao, N. J., The transport and quantum capacitance properties of epitaxial graphene. *Appl Phys Lett* **2010,** *96* (16).

178. Kim, E. J.; Chagarov, E.; Cagnon, J.; Yuan, Y.; Kummel, A. C.; Asbeck, P. M.; Stemmer, S.; Saraswat, K. C.; McIntyre, P. C., Atomically abrupt and unpinned Al2O3/In0.53Ga0.47As interfaces: Experiment and simulation. *J Appl Phys* **2009,** *106* (12).

179. Russo, S.; Craciun, M. F.; Yamamoto, M.; Morpurgo, A. F.; Tarucha, S., Contact resistance in graphene-based devices. *Physica E* **2010,** *42* (4), 677-679.

180. Xia, F. N.; Perebeinos, V.; Lin, Y. M.; Wu, Y. Q.; Avouris, P., The origins and limits of metal-graphene junction resistance. *Nat Nanotechnol* **2011,** *6* (3), 179-184.

181. Lee, B.; Mordi, G.; Kim, M. J.; Chabal, Y. J.; Vogel, E. M.; Wallace, R. M.; Cho, K. J.; Colombo, L.; Kim, J., Characteristics of high-k Al2O3 dielectric using ozone-based atomic layer deposition for dual-gated graphene devices. *Appl Phys Lett* **2010,** *97* (4).

182. Kim, S.; Nah, J.; Jo, I.; Shahrjerdi, D.; Colombo, L.; Yao, Z.; Tutuc, E.; Banerjee, S. K., Realization of a high mobility dual-gated graphene field-effect transistor with Al2O3 dielectric. *Appl Phys Lett* **2009,** *94* (6).

183. Park, J. H.; Movva, H. C. P.; Chagarov, E.; Sardashti, K.; Chou, H.; Kwak, I.; Hu, K. T.; Fullerton-Shirey, S. K.; Choudhury, P.; Banerjee, S. K.; Kummel, A. C., In Situ Observation of Initial Stage in Dielectric Growth and Deposition of Ultrahigh Nucleation Density Dielectric on Two-Dimensional Surfaces. *Nano Lett* **2015,** *15* (10), 6626-6633.

184. Yang, W.; Sun, Q. Q.; Geng, Y.; Chen, L.; Zhou, P.; Ding, S. J.; Zhang, D. W., The Integration of Sub-10 nm Gate Oxide on MoS2 with Ultra Low Leakage and Enhanced Mobility. *Sci Rep-Uk* **2015,** *5*.